

FERROELECTRICITY IN FREE NIOBIUM CLUSTERS

A Dissertation
Presented to
The Academic Faculty

By


Ramiro Alfredo Moro


In Partial Fulfillment
Of the Requirements for the Degree
Doctor of Philosophy in Physics


Georgia Institute of Technology
November, 2003

FERROELECTRICITY IN FREE NIOBIUM CLUSTERS


Approved by:


Dr. Walter A. de Heer, Advisor


Dr. Edward H. Conrad


Dr. Phillip First


Dr. Uzi Landman


Dr. Robert L. Whetten
(G.I.T. Department of Chemistry)

Date Approved 11/18/2003

This work is dedicated to my wife Maribel and my daughter Nathalie.

ACKNOWLEDGEMENT

I want to thank Walter de Heer who is the leader of our reasearch group and my advisor. Also thanks to former members of the group that contributed in building the molecular beam machine including Philippe Poncharal, Stefan Frank and Patrice Keghelian and current members of the group that participated in this work Xiaoshan Xu and Shuangye Yin.

Interesting discussions were held with Cristian Batista, Gerd Bergmann, Dragomir Davidovic, Phillip First, Brian Kennedy, Vitaly Kresin, Uzi Landman, Carlos Sa de Melo and Robert Whetten. Some friends that helped me in many different ways include Armando A. Anaya, Asmerom Y. Ogbazghi, Jacob A. Sauer, and Denis B. Semwogerere.

Support from the machine shop came from Leon Halverson, Sam Mize and Norman Scott. I also received assistance and cooperation from Nancy Baggett, Helmut Biritz, Kevin Carter, Patricia Dixon, Keith Garner, Mark Miller, Velera Pate, Jack Ramsey and Andrew Zangwill.

I received constant support from my wife, my parents, brothers, sister and friends.

TABLE OF CONTENTS

Dedication	iii
Acknowledgement	iv
List of Tables	vii
List of Figures	viii
List of Symbols	xv
Summary	xvii
I Introduction	1
1.1 Electrical Polarizability in Metal Clusters	6
1.2 Evidence of Permanent Dipole Moments in V, Nb and Ta clusters	9
II The Molecular Beam Machine	13
2.1 Overview	13
2.2 Cluster Source	15
2.3 Deflection Plates	20
2.4 Speed Measurement	24
2.5 Time of Flight Mass Spectrometer	31
2.6 Calibration	36
2.7 Data Analysis Methods	38
III Experimental Results with Niobium Clusters	40
3.1 Deflections at 300 Kelvin. Normal Polarizabilities	40
3.2 Low Temperature Results	42

3.3 Simple Model to explain Field and Temperature Dependence	51
3.4 Transition Temperatures and Dipole Moments Calculated in the Model	56
3.5 Stern-Gerlach Experiments with Niobium clusters	59
3.6 Correlation between Magnetic and Electric Deflection Experiments	70
IV Experiments with Vanadium, Tantalum and Nb_NAl_M	71
4.1 Electrical Polarizabilities of Vanadium and Tantalum Clusters	71
4.2 Low Temperature Results with Vanadium and Tantalum Clusters	74
4.3 Results with Nb_NAl_M	78
V Discussion and Conclusion	79
5.1 Possible connection with superconductivity	79
5.2 Conclusion	82
References	84
Vita	91

LIST OF TABLES

Table 1	Value of the second moment of the distribution of magnetic moments for several coupling cases.	67
---------	------------------------------------------------------------------------------------------------	----

LIST OF FIGURES

Figure 1	Principle of the electric deflection experiment. A neutral particle passes through a region of inhomogeneous electric field where it changes its trajectory producing a deflection, which is measured.	5
Figure 2	A classical perfect spherical conductor is polarized by an electric field. The induced dipole moment is parallel to the electric field.	6
Figure 3	A simple metal cluster in an electric field. Schematic that shows the electronic spill-out effect.	7
Figure 4	Experimentally measured polarizability per atom of sodium clusters [G. Tikhonov, 2001]. Short dashed line is the bulk limit (from equation 4). Long dashed line is the approximation given by equation 6 with $\delta = 0.13$ nm.	8
Figure 5	Main parts of the apparatus. A YAG laser, steering prisms, a focusing lens, a vaporization cluster source, a mechanical chopper, skimmers, collimators, electric deflection plates, a scanning slit, an excimer laser for ionization and a time of flight mass spectrometer. The length of the apparatus is about 3 m from the focusing lens to the UV window. Pressures are 10^{-2} Torr in the first chamber and 10^{-9} Torr in the mass spectrometer.	14
Figure 6	A laser-vaporization source for metal clusters. The in-line design allows precise alignment of the beam. The target rod is inserted laterally which allows changing samples without breaking vacuum. The YAG laser (Continuum, Surelite I-20) pulses for 6 ns (full width at half the maximum) delivering 55 mJ at 355 nm. The laser evaporates atoms of the surface of the sample and they make a plume of hot plasma. A pulsed valve (Parker) opens for 1 ms, injecting ultra high pure helium in the small cavity where the sample sits. The evaporated atoms are cooled down by the gas and coalesce to form clusters. The gas exits the source through the nozzle, carrying the clusters along. At the exit of the nozzle there is a skimmer that communicates the first two vacuum chambers and allows only the center part of the beam to pass.	16
Figure 7	Schematic diagram of the cryogenic cluster source. The second stage of a cryocooler (Sumitomo, SRDK) is connected to a cold finger that cools down the source and a reservoir. The first pulsed valve	

(Parker) injects the gas into the reservoir. It stays there for 40 ms and a special pulsed valve controls its injection into the source. A silicon diode is used to measure temperature. The source and reservoir are drawn to scale. A 25-ohm heater is used to control the temperature. Brass screws are used to avoid loosening at low temperatures. The cold finger, source and reservoir are made of copper. The connection between the cold finger and source is through 30 layers of silver foil pressed together.

18

Figure 8 (a) Cross section of the electric deflection plates used in the experiments. (b) Schematic of the electric connections of deflection plates.

21

Figure 9 Distances involved in calculating electric deflections. L_1 : length of the deflection field, L_2 : distance from field to detector, d : cluster deflection.

23

Figure 10 The speed is measured by chopping the beam and detecting the loss of signal. The chopper consists of an electric motor (Portescap, 22S) with a pair of metallic blades attached. It normally runs at 6000 RPM. The sensor, which determines the position of the chopper blades, has a phototransistor illuminated by an LED. When a blade is in the path of the light it is detected by the phototransistor as a high impedance state and at the same time the opposite blade is in the path of the cluster beam. The distance between the blades and the detector is known ($L = 2.45$ m) and we measure the time between the chopping of the beam and the detection ($T_2 - T_1$) to determine the speed.

25

Figure 11 The chopper clips a cobalt cluster beam. Eighteen mass spectra are presented taken at different chopper times. The time of flight axis goes from zero to 50 μ s and covers clusters up to Co_{85} . When time is too short or too long the blade misses the beam so everything is transmitted. Depletion happens when timing is right and the transmitted signal in the middle is due to the slit in the blade of the chopper.

26

Figure 12 Timing sequence for the experiment. The time axis is not at scale. The sequence starts with the first pulsed valve (Parker) that fills the reservoir with helium at room temperature. Later, one of the blades of the chopper crosses the path of the cluster beam triggering the rest of the time sequence. The gas, already cold, is injected when the second valve opens. Then the YAG laser pulses

(Continuum, Surelite I-20) evaporating some atoms from the surface of the sample. With the cold gas, clusters are produced which start going towards the mass spectrometer. If timing is right the second blade of the chopper chops the beam and that is observed as a depletion of signal at the detector.

28

Figure 13 Timing sequence diagram. The chopper signal is treated to measure the time between the first and second blades. (a) TTL signal from light sensor. There are two notched pulses per revolution. (b) Inverted signal from the sensor. (c) Output of a one-shot circuit that gives a 1.1 ms long square wave. (d) The signal is divided by two in counter 1 of a data acquisition card (National Instruments, PCI-1200) and gives a square wave whose length is half the period of the chopper. (e) Clock signal of Counter 0, which is fixed at 2MHz. (f) Counter 0 starts at 50 000 and counts down while signal (d) is high, this way the difference between 50 000 and the final value is the time between the blades of the chopper in halves of microseconds.

30

Figure 14 Schematic of the time of flight mass spectrometer. Clusters are ionized by the excimer laser (Lambda Physik, Optex, 193nm, 6.4 eV) and accelerated by an electric field towards a pair of grounded grids. Later, they are further accelerated towards a third grid and a micro channel plate (MCP, Galileo). The hitting of the charged cluster on the MCP creates an avalanche of electrons that are collected in a plate. The signal is amplified (Ortec, 9327) and sent to a multichannel analyzer (Fast Comtec, 7886) where it is recorded.

32

Figure 15 High-resolution mode of the mass spectrometer. (a) Time of flight (TOF) in microseconds for a Nb_{15} cluster as a function of the initial position in the ionization region. (b) Peak profile of Nb_{15} as a function of time of flight. The time resolution of this peak ($\text{TOF}/\delta\text{TOF}$) is greater than 17 000, which corresponds to a mass resolution ($\text{Mass}/\delta\text{Mass}$) of 8500.

33

Figure 16 Position sensitive mode of the mass spectrometer. (a) Time of flight (TOF) in microseconds for a Nb_{15} cluster as a function of the initial position in the ionization region. (b) Peak profile of Nb_{15} as a function of time of flight. The time resolution of this peak is 3500, and mass resolution 1750.

34

Figure 17	(a) High-resolution spectrum of niobium clusters. (b) Expanded region around Nb_{11} . The mass scale is with respect to 1022.01 atomic mass units (c) Expanded region around Nb_{11}O .	37
Figure 18	Position-Sensitive mass spectrum with and without electric field for Nb_{17} at 300 K. Dashed line is with field off. Continuous line is with $E = 80 \text{ kV/cm}$.	40
Figure 19	Polarizability per atom of niobium clusters at 300 K. Dashed line is the bulk limit and also shown is the value calculated using equation 6 for the spill-out model with $\delta = 0.1 \text{ nm}$.	41
Figure 20	Deflections as a function of electric field for Nb_{15} . These experiments at 300 K demonstrate that the deflections are quadratic with applied field. Dashed line is a quadratic fit to the data.	42
Figure 21	Representative deflection profiles of some niobium clusters at three temperatures. Dashed lines at zero field, continuous lines at 80 kV/cm. At 300 K deflections are small and consistent with normal metal clusters. At 50 K some clusters develop tails that extend several millimeters. At 20 K some clusters are deflected beyond the detector limits yielding loss of detected intensity. The fraction R of the clusters that show anomalous deflections, either detected in the tail or deflected beyond the detection limits is a function of the temperature and electric field intensity.	44
Figure 22	Deflection profiles of Nb_{14} at 50 K and several electric fields. The dashed line is at zero field intensity. For every profile we can distinguish a main peak and a tail. The main peaks are deflected tens of micrometers. The tails instead are deflected several millimeters. Inset: Deflections of the main peaks as a function of the electric field applied, which demonstrate they are quadratic with the field.	45
Figure 23	Extension of the observed tail for Nb_{14} as a function of electric field at 50 K. The straight line is a linear fit to the data which extrapolates to give an intercept of 11 kV/cm, which is interpreted as the electric field need to uncouple the dipole moment.	46
Figure 24	Permanent dipole moments calculated from the extension of the visible tails in niobium clusters at 50 K and 80 kV/cm.	46

- Figure 25 Filled squares are experimentally measured polarizabilities per atom of niobium clusters at 20 K. These values were calculated from the average deflections of clusters that are left after applying an electric field of 80 kV/cm (which deflects most of the anomalous fraction beyond the detector limits). In the case of Nb₉, Nb₁₁ and Nb₁₄ there is a certain fraction of the clusters that are deflected negatively (towards weaker fields) and these clusters are not swept away, that is why their polarizabilities are anomalously low. The thin dashed line is the polarizability at 300 K that is reproduced here for comparison. Notice that the values at 20 K are systematically lower than the room temperature data. It is also remarkable the odd-even alternation in the region Nb₂₅-Nb₄₅ with higher polarizabilities for odd clusters. The thick dashed line indicates the bulk limit. 48
- Figure 26 Ferroelectric fraction of niobium clusters at 20 K and 40 K defined as the fraction of the clusters in the tails, either visible or not. Experiments with an electric field of 40 kV/cm. 50
- Figure 27 Ferroelectric fraction of niobium clusters measured at 16 K and 72 kV/cm. Filled squares are odd clusters, open circles are even clusters. The accuracy from counting statistics is 5.3% or better. 51
- Figure 28 The model by P. Dugourd [P. Dugourd, 2001] correctly predicts the shape of the deflected peak of a molecule of Ti C₆₀ with a dipole of 8.1 D. Filled squares are experimental values, thin dashed line their model prediction. The experiment at 8 kV is done with an electric field of 48.3 kV/cm. 52
- Figure 29 A Stark diagram for Nb₁₂ where M_J=10 and P₀=20 D. Two regions are visible, one of dense avoided crossings that yield an almost zero slope and a region of downwardly going levels. Only every hundredth energy level is shown in the main figure. Insets show every level in the expanded region. 55
- Figure 30 Ferroelectric fraction (R) experimentally measured at 3 temperatures and several electric field intensities for Nb₃₀. The continuous lines are the fitting functions calculated in the proposed model. 56

Figure 31	Permanent dipole moment per atom for niobium clusters calculated in the proposed model.	57
Figure 32	Ferroelectric transition temperatures of niobium clusters calculated in the proposed model.	58
Figure 33	Niobium clusters in the range Nb_2 to Nb_7 deflected by an inhomogeneous magnetic field. The dashed line is the profile without magnetic field and the solid line is after applying 0.9 T. The experiment was done at 20 K. The niobium dimer does respond to the magnetic field as expected [A.M. James, 1993].	60
Figure 34	Niobium clusters in the range Nb_8 to Nb_{13} deflected by an inhomogeneous magnetic field. The dashed line is the profile without magnetic field and the solid line is after applying 0.9 T. This experiment was done at 20 K. The response of Nb_9 is stronger than Nb_7 (shown in the previous figure).	61
Figure 35	The Stern-Gerlach experiment of Nb_{22} . The dashed line is the peak with zero field and the solid line is after applying 0.9 T. The x-axis scale has been converted to magnetic moment in Bohr magnetons. Almost no visible response to the magnetic field. This is also the case for all even-clusters studied, with the only exception of the dimer.	62
Figure 36	The Stern-Gerlach experiment of Nb_{23} . The dashed line is the peak with zero field and the solid line is after applying 0.9 T. The x-axis scale has been converted to magnetic moment in Bohr magnetons. Contrary to ferromagnetic clusters [W.A. de Heer, 1990], the response is towards higher as well as lower magnetic field in this case.	62
Figure 37	Magnetic moment of niobium clusters measured from the extension of magnetic deflections in Stern-Gerlach experiments. Filled squares are odd clusters, open squares are even clusters.	64
Figure 38	Hypothetical deflection profiles for different coupling cases. (a) Spin strongly coupled to the total angular momentum of the cluster produces a pedestal-like distribution of magnetic moments. (b) Spin strongly coupled to the cluster axis produces a logarithmic distribution of magnetic moments. (c) Spin uncoupled produces two projections. (d) Spin in contact with a thermal bath produces a	

	small thermally averaged deflection. The dashed lines are the profiles with zero field and the continuous lines are with a magnetic field applied. The magnetic moment distributions have been convoluted with the undeflected peaks to get the simulated profile.	66
Figure 39	Second moment of the distribution of magnetic moments of niobium clusters. Experiments done at $T=20$ K for the range Nb_{6-70} (squares) and at $T=33$ K for Nb_{3-5} (circles). Filled symbols are odd clusters, open symbols are even clusters.	69
Figure 40	Width of the distribution of magnetic moments in niobium clusters with odd number of electrons measured at 20 K and 0.9 T (solid line) compared to the ferroelectric fraction measured at 20 K and 60 kV/cm (dashed line).	70
Figure 41	Polarizability per atom of vanadium clusters measured at 300 K and 72 kV/cm. The dashed line is the bulk limit and also shown is the polarizability calculated with the spill-out approximation (equation 6) for $\delta=0.18$ nm.	72
Figure 42	Polarizability per atom of tantalum clusters measured at 300 K and 72 kV/cm. The dashed line is the bulk limit and also shown is a fitting with the spill-out approximation (equation 6) with $\delta = 0.19$ nm.	73
Figure 43	Ferroelectric fraction of vanadium clusters in the range V_{10} to V_{88} . Experiment done at 18 K and 80 kV/cm. Errors shown are from counting statistics.	75
Figure 44	Ferroelectric fraction of tantalum clusters in the range Ta_5 to Ta_{96} . Experiment done at 21 K and 80 kV/cm. Errors are from counting statistics.	76
Figure 45	Transition temperature T_G calculated in the model for vanadium clusters.	77
Figure 46	Transition temperature T_G calculated in the model for tantalum clusters.	77
Figure 47	Ferroelectric fraction in a cluster of 15 niobium atoms doped with aluminum. Error bars show the uncertainty in counting statistics. Experiment done at 34 K and 60 kV/cm.	78

LIST OF SYMBOLS

amu	Atomic mass unit (1.67×10^{-27} kg)
Å	Unit of length, Angstrom (10^{-10} m)
D	Debye, unit of electric dipole moment, equal to 3.34×10^{-30} C m
E	Electric field intensity
Excimer	Excited dimer, used in the excimer laser
I_i	i^{th} -moment of a distribution
IP	Ionization Potential
$I(x)$	Intensity
J	Total angular momentum (Spin plus rotational angular momentum)
K	Projection of the total angular momentum (J) on the cluster axis
K	Heat conductivity
k_B	Boltzman constant (1.38×10^{-23} J T ⁻¹)
LED	Light emitting diode
m	mass of the cluster
MCP	Microchannel Plate
M_J	Projection of the total angular momentum (J) on the electric field axis
M_0	Total magnetic moment
N	Number of atoms in a cluster
P	Electric dipole moment
P_0	Permanent electric dipole moment

R	Radius of a particle or ferroelectric fraction
R_s	Wigner-Seitz radius
T	Temperature
T_G	Ferroelectric transition temperature
TOF	Time of flight
Torr	Unit of pressure, equal to 133.32 Pa
U	Potential energy
UV	Ultraviolet. A UV window transmits ultraviolet light.
v	Speed of the beam
W	Energy
YAG	Yttrium Aluminum Garnet, used in the YAG laser.
α	Polarizability
α_{atom}	Polarizability per atom
δ	Energy level spacing or spill-out distance of the electron cloud.
Δ	Superconducting energy gap
ϵ_0	Permittivity of vacuum ($8.85 \times 10^{-12} \text{ F m}^{-1}$)
μ_B	Bohr magneton, unit of magnetic moment ($9.27 \times 10^{-24} \text{ J T}^{-1}$)

SUMMARY

Niobium clusters were studied in a molecular beam. Electric deflection measurements showed normal metallic polarizabilities at room temperature, larger than the bulk value. At low temperatures many clusters develop electric dipole moments of the order of 1 Debye per atom which contradict metallic properties. A simple model is proposed to explain the electric field and temperature dependence of the observations. Magnetic deflection experiments showed no response from clusters with even number of electrons (except for the dimer), while clusters with odd number of electrons have magnetic moments due to the last unpaired electron with g-factors close to 2. Size dependent variations were found in the second moment of the distribution of magnetic moments. Evidence was found which indicates that the spin of the last electron uncouples when the cluster becomes ferroelectric. The study is extended to tantalum and vanadium clusters, which also show ferroelectricity at low temperatures. In general the ferroelectric state occurs at higher temperatures for clusters with even number of electrons in the three metals studied.

CHAPTER I

INTRODUCTION

The objects studied in this thesis are very small. A particle of 28 niobium atoms has a diameter of just 1nm, about 20 times smaller than the smallest viruses known. Their study falls in the area of clusters, intermediate between atomic and condensed matter physics. The study of clusters tries to find the evolution of physical properties from the atom to the bulk.

Simple metal clusters have been extensively studied [W.A. de Heer, 1993]. From experiments of mass abundance spectra in sodium [W.D. Knight, 1984] evidence of a shell structure in the electronic levels was found that causes certain sizes to be more stable than others. Closed shells occur at 8, 20, 40 and 58 sodium atoms. Later, evidence of the shell structure was also found in the mass abundance spectra of potassium [W.D. Knight, 1985a], copper, silver and gold [I. Katakuse, 1985]. A property like the ionization potential (IP) shows the transition from atomic to bulk-like behavior. Measurements of IPs in sodium [G. Wrigge, 2002], potassium [W.A. de Heer, 1987] and silver [G. Alameddin, 1992] show high values for small clusters and a downward trend towards the work function (which is the bulk limit) while also showing size dependent variations that can be interpreted by considering the shell structure. The main lesson learned from the study of these simple metal clusters is that they are not exotic and even in the smaller size

range they already resemble the bulk and their properties are dominated by the valence electrons.

Ferromagnetic clusters of iron, nickel and cobalt have been studied too [I.M.L. Billas, 1994] [J.P. Bucher, 1991]. It was found that their spin aligns with a magnetic field [W.A. de Heer, 1990], following a thermal averaged behavior as in the case of superparamagnetism [S.N. Khanna, 1991]. The magnetic moments are enhanced with respect to the bulk, possibly due to surface effects. Some rhodium and manganese clusters were found to be ferromagnetic [A.J. Cox, 1993][M.B. Knickelbein, 2001] (Rh is not magnetic and Mn is antiferromagnetic in the bulk) which shows two cases where properties are unique to small systems, since in both cases the effect disappears with increasing size.

Phase transitions have been observed in clusters. A ferromagnetic to paramagnetic transition has been seen in $\text{Ni}_{200-240}$ at $T = 340$ K [D. Gerion, 2000]. In those experiments the heat capacity was obtained by heating clusters with photons and measuring temperature as a function of energy absorbed. Evidence of a rigid-fluid transition was observed in argon clusters [M.Y. Hahn, 1988]. The melting point and heat capacity of Na_{139} has been determined from the temperature dependence of its photofragmentation mass spectrum [M. Schmidt, 1997]. Also the melting point of tin clusters from measurements of formation energies [T. Bachelis, 2000]. A structural phase transition was found in Si_N clusters [M.F. Jarrold, 1991] deduced from drift velocities experiments.

In this thesis we study niobium clusters. Our motivation to choose niobium was that among the pure elements it has the highest critical temperature for superconductivity [C. Kittel, 1996] with the exception of lithium which becomes a superconductor at 20 K, but at high pressures [K. Shimizu 2002].

Superconductivity does not occur in an atom, but it must develop at some point when the particle grows, so we wanted to observe its onset in a cluster. Electron tunneling experiments in aluminum particles [C.T. Black, 1996] as small as 10 nm in diameter still show evidence of the superconducting energy gap (Δ). Nuclear magnetic resonance experiments [K. Nomura, 1980] in aluminum particles showed superconducting features down to 4 nm. Scaling rules tell that the Meissner effect should be suppressed in small clusters [D. Shoenberg, 1962] and indeed our magnetic experiments with niobium did not show evidence of diamagnetism, but only the response of the unpaired electron in clusters with odd number of atoms [W.A. de Heer, 2003a]. Recent experiments of magnetization in small lead particles [S. Reich, 2003] have shown that the transition from diamagnetism to normal behavior happens at the Anderson limit [P.W. Anderson, 1959], that is, when the electronic energy level spacing (δ) is equal to the superconducting energy gap. The clusters that we study in this thesis are in the ultra-small regime where the energy level spacing is larger than the superconducting energy gap ($\delta > \Delta$).

A straightforward way to investigate the properties of clusters is by measuring their electric polarizability [V.V. Kresin, 1997]. The tool used in this research is a molecular

beam machine [G. Scoles, 1988] [W. A. de Heer, 1991a]. The experiment is schematically depicted in figure 1. The principle is simple. Neutral particles pass through a region of inhomogeneous electric field. They become polarized and are deflected towards the stronger field. The goal is to measure this deflection as a function of temperature, size of the cluster and field intensity.

Limited work has been done with metallic cluster beams at low temperature [S. Pokrant, 2000] [D. Gerion, 1999]. Part of this thesis involved the development of a cryogenic source, able to cool the clusters down to $T = 9$ K.

Our experiments with niobium clusters at low temperatures showed a surprising effect. Many clusters develop a permanent electric dipole moment at low temperatures [R. Moro, 2003]. This thesis presents our results in characterizing this effect. The fraction of clusters that showed large dipole moments was measured at several fields and temperatures. A model is proposed to explain the observations. The study is extended to vanadium and tantalum, that are also superconductors.

Chapter II describes the apparatus, chapter III shows our experimental results with niobium and describes the model proposed. In chapter IV the work is extended to vanadium and tantalum and in chapter V we discuss a possible connection with superconductivity.

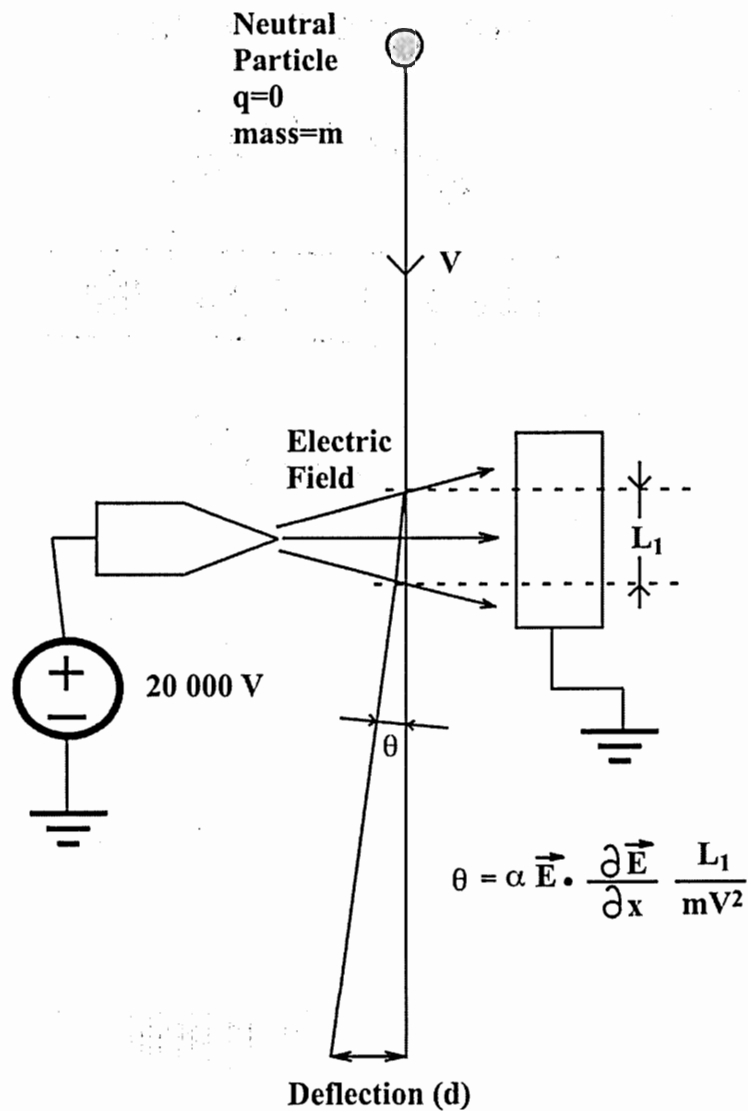


Figure 1: Principle of the electric deflection experiment. A neutral particle passes through a region of inhomogeneous electric field where it changes its trajectory producing a deflection, which is measured.

1.1 Electric Polarizability of Metal Clusters

A classical perfect conductor in an electric field develops a dipole moment (\bar{P}) that cancels the electric field inside the material (see figure 2). This gives rise to a polarizability (α) proportional to the volume of the particle.

$$\bar{P} = \alpha \bar{E} \quad (1)$$

$$\alpha = 4\pi\epsilon_0 R^3 \quad (2)$$

Where R is the classical radius of the particle.

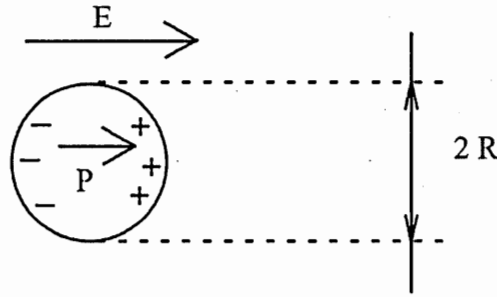


Figure 2: A classical perfect spherical conductor is polarized by an electric field. The induced dipole moment is parallel to the electric field.

If the particle has N atoms, the polarizability per atom (α_{atom}) will be given by the following equation:

$$\alpha_{\text{atom}} = \frac{\alpha}{N} = \frac{1}{N} 4\pi\epsilon_0 R^3 \quad (3)$$

In the bulk limit R^3/N is the Wigner-Seitz radius cubed (R_s^3) so:

$$\alpha_{\text{atom}} = 4\pi\epsilon_0 R_s^3 \quad (4)$$

Experiments in sodium clusters show a larger polarizability for the small sizes [W.D. Knight, 1985b] [G. Tikhonov, 2001]. For larger clusters the polarizability approaches the bulk limit given by equation 4. In first order the discrepancy for small clusters can be explained by considering that the electrostatic screening goes beyond the classical boundary of the cluster [N.D. Lang, 1970]. This is due to the spill-out of the electrons which is of the order of 0.13 nm for sodium. Hence the polarizability is modified to give equation 5.

$$\alpha = 4\pi\epsilon_0(R + \delta)^3 \quad (5)$$

So that the polarizability per atom can be approximated by equation 6.

$$\alpha_{\text{atom}} = 4\pi\epsilon_0 \left(R_s + \frac{\delta}{\sqrt[3]{N}} \right)^3 \quad (6)$$

Clearly the correction is more important for small clusters, as seen in experiments [W.A. de Heer, 1993] [V.V. Kresin, 1997]. Figure 3 shows a schematic of this spill out effect, for a cluster of 20 sodium atoms, where the correction to the polarizability is 40%.

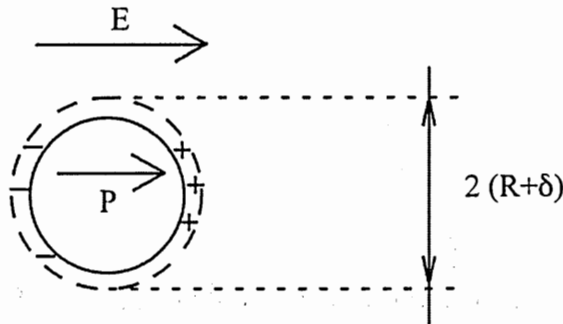


Figure 3: A simple metal cluster in an electric field. Schematic that shows the electronic spill-out effect.

A recent polarizability measurement in sodium clusters is presented in figure 4 [G. Tikhonov, 2001]. There are variations in the polarizability superimposed over the spill-out approximation. These variations up to Na_9 have been reproduced almost perfectly by spin-dependent local-density approximation (LSDA) [I. Moullet, 1990]. The spherical jellium model predicts larger polarizabilities of open shell clusters compared to closed shell ones [W. Eckardt, 1984], but underestimates their values by 15%.

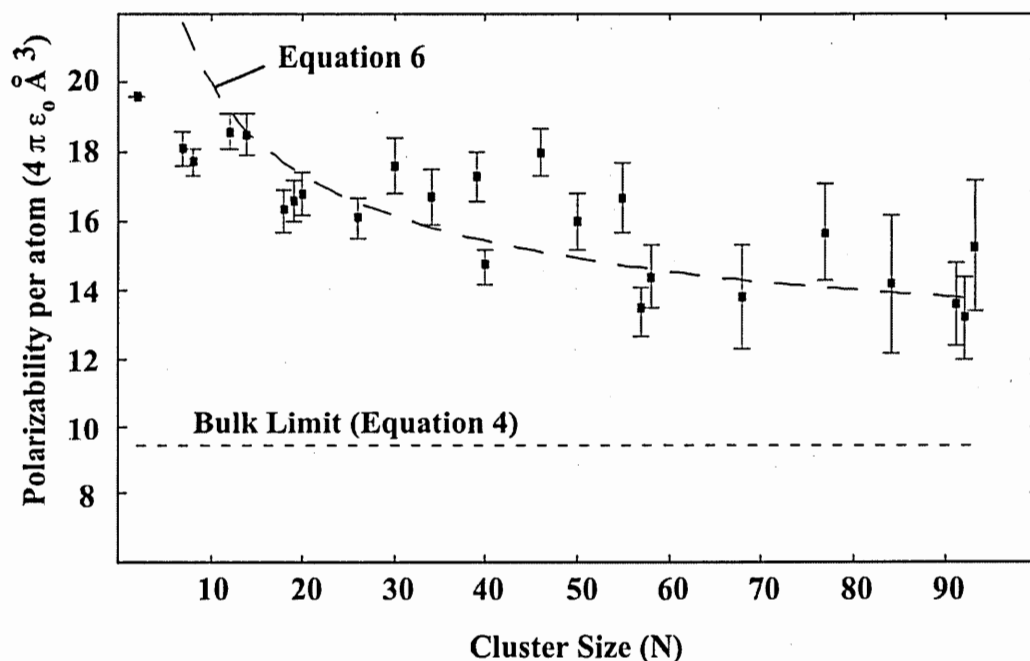


Figure 4: Experimentally measured polarizability per atom of sodium clusters [G. Tikhonov, 2001]. Short dashed line is the bulk limit (from equation 4). Long dashed line is the approximation given by equation 6 with $\delta = 0.13$ nm.

A more complicated example of polarizabilities is the case of aluminum clusters, where a deviation from the jellium model was found [W.A. de Heer, 1989]. In particular, the polarizabilities of small clusters are below the jellium value and they recover for clusters greater than Al_{40} .

An experiment with nickel [M.B. Knickelbein, 2001a] showed some clusters whose polarizabilities were significantly larger than the classical ideal value even after considering the spill-out effect (For example Ni_{51} has a polarizability of twice the classical value). These deviations can be explained in part by considering the atomic structures, where closely packed or quasispherical structures show polarizability minima, while structures with “missing” atoms display higher values.

Niobium clusters at room temperature behave like simple metal clusters (as will be seen in chapter III), with larger polarizabilities than the bulk limit that can be approximated in first order by the spill-out effect. That changes at low temperatures.

1.2 Evidence of Permanent Dipole Moments in V, Nb and Ta clusters.

As reported in detail in chapter III, the response of niobium clusters to an electric field at low temperatures is more complex. At $T=50\text{K}$ the deflections for some clusters are several orders of magnitude larger than for normal polarizable clusters [R. Moro, 2003]. Moreover, the extensions of these deflections do not follow a quadratic dependence with

field, suggesting they are due to permanent dipole moments (a polarizable particle has a quadratic response to the electric field). In contrast, it is predicted [S.A. Blundell, 2000] only a 15% change in the polarizability for sodium clusters between room temperature and $T=0$ K. A large variation in the polarizability as a function of temperature has been observed in Ge_NTe_M [R. Schäfer, 1996] but never in metallic clusters.

Permanent dipole moments have been seen in clusters and molecules. For example in Ge_2Te and Ge_2Te_2 [R. Schäfer, 1996] and in TiC_{60} [P. Dugourd, 2001], but its observation in niobium clusters contradicts metallic properties. The electrons in a metal would screen any electric field canceling the dipole moment.

Not all niobium clusters have the anomalous property. Some sizes behave normally even at low temperatures, like Nb_{17} for example. For the ones that have the anomalous property there is a fraction that behaves normally at a given temperature. In chapter III we characterize these phenomena.

It is important to notice that these are isolated particles, so even though they come from a source at a very well defined temperature, the distribution of energy states is broad. As an illustrative example, for an ensemble of simple harmonic oscillators the probability of finding one oscillator in state n is given by equation 7, where Δ is the energy gap between levels.

$$P(n) = \frac{e^{-\frac{n\Delta}{k_B T}}}{\sum_{i=0}^{\infty} e^{-\frac{i\Delta}{k_B T}}} = e^{-\frac{n\Delta}{k_B T}} \left(1 - e^{-\frac{\Delta}{k_B T}} \right) \quad (7)$$

For example if $T=20$ K and $\Delta/k_B=10$ K, the probability of finding the oscillator in the ground state will be 40%, in the first excited state 24% and so on. Similarly in our experiments the temperature of the clusters ensemble is known, but their states are distributed over a broad range.

As explained in more detail in chapter III, the response of niobium clusters as a function of field is also interesting. The transition from a normal behavior to an anomalous one is sharp. For example, when increasing the field from 20 to 40 kV/cm a fraction as large as 20% of the clusters could go from being deflected a few hundred microns to several millimeters. This is explained in a simple model where energy levels anti-cross in a Stark diagram giving a zero average slope and only when the field is large enough the full slope of the level is realized.

Vanadium and tantalum clusters also show this effect, however it is weaker in both metals. In other words, for them it happens at lower temperatures and higher fields. Other interesting feature of the effect is that it is stronger for clusters with even number of electrons. This has been observed in the three metals studied [W.A. de Heer, 2003b].

Stern-Gerlach magnetic deflection experiments were also done with niobium clusters and

we were able to observe the magnetic moment of the last unpaired electron [W.A. de Heer, 2003a]. The g-factors found are all close to 2.0, but the second moment of the distribution of magnetic moments is strongly size dependent. These results are described in chapter III together with a possible correlation with the ferroelectric state.

CHAPTER II

THE MOLECULAR BEAM MACHINE

2.1 Overview

In the present work clusters are studied free in a molecular beam [G. Scoles, 1988] [W.A. de Heer, 1993]. The experimental set up consists of a source, where clusters are formed and thermalized in helium, then they travel in vacuum and pass in between a pair of deflection plates where an inhomogeneous electric field is applied. This field produces a force that deflects the particles. Using position-sensitive time-of-flight-mass-spectrometry [W.A. de Heer, 1991a] the mass and deflections are determined simultaneously. This information, together with the speed of the beam allows us to find polarizabilities and dipole moments. As shown in the schematic diagram in figure 5 the apparatus consists of a series of vacuum chambers where clusters are created, deflected and detected. In the first chamber there is only rough vacuum (10^{-2} Torr). The pressures are progressively lower in the next chambers and the mass spectrometer is at high vacuum (10^{-9} Torr). The distance from the source to the detector is 2.51m. The experiment is pulsed. Normally the repetition rate is 20 Hz, which means that the source produces a beam of clusters every 50 ms. These clusters are deflected and detected and results are accumulated in a computer. To get good statistics the experiments last several hours with hundreds of alternations between field on and off.

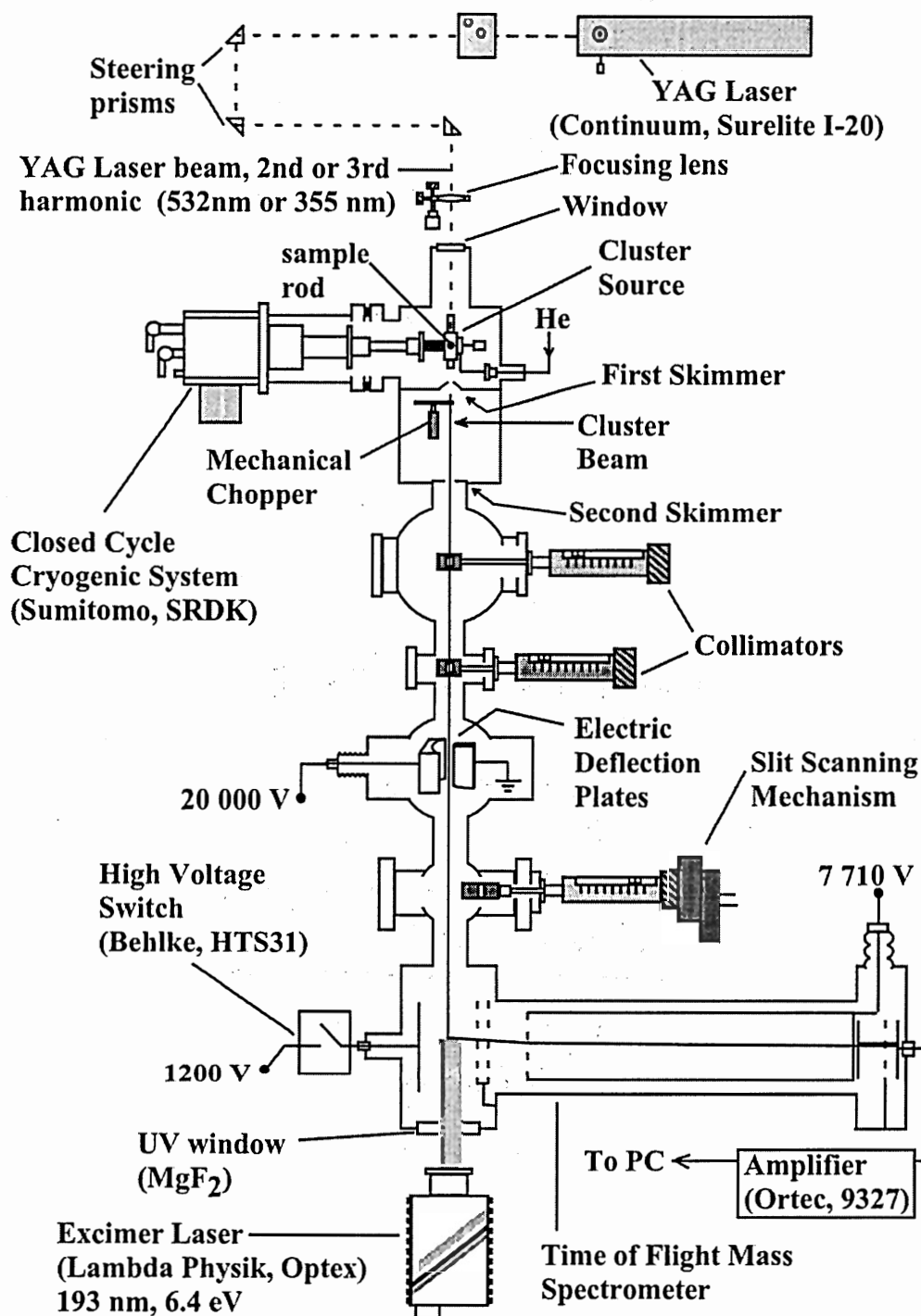


Figure 5: Main parts of the apparatus. A YAG laser, steering prisms, a focusing lens, a vaporization cluster source, a mechanical chopper, skimmers, collimators, electric deflection plates, a scanning slit, an excimer laser for ionization and a time of flight mass spectrometer. The length of the apparatus is about 3 m from the focusing lens to the UV window. Pressures are 10^{-2} Torr in the first chamber and 10^{-9} Torr in the mass spectrometer.

2.2 Cluster Source

In our experiments we use a laser vaporization source [R.E. Smalley, 1983] like the one shown in figure 6. The sample material, usually in the shape of a rod, sits inside a cavity. A YAG laser beam (Continuum, Surelite I-20) is focused on the sample. The laser pulses have a full width at half the maximum of 6 ns and energy of 55 mJ per shot, so the instantaneous power is about 1 MW. This is enough to evaporate about 10^{13} atoms from the surface of the sample. These atoms are very hot, but at the same time as the laser pulses a valve is opened, injecting about 5×10^{-6} mol of gas in the cavity. The gas is usually helium. It cools down the atoms that then coalesce to form clusters. The cavity has a nozzle, so the gas escapes the cavity carrying the clusters with it. Because the clusters are very small they acquire the speed of the carrier gas. At the exit of the nozzle there is a skimmer that communicates the first chamber with the second. Only the center part of the beam goes through the hole in the skimmer to the next chamber.

One very important goal in our experiments was to produce low temperatures beams to try to uncover new physics. Furthermore, keeping all other conditions equal, deflections (either magnetic or electric) are inversely proportional to the speed of the beam squared. In other words, they are inversely proportional to the temperature. Consequently a beam at 50 K will be deflected six times more than at room temperature, which translates into better accuracy in the measurements.

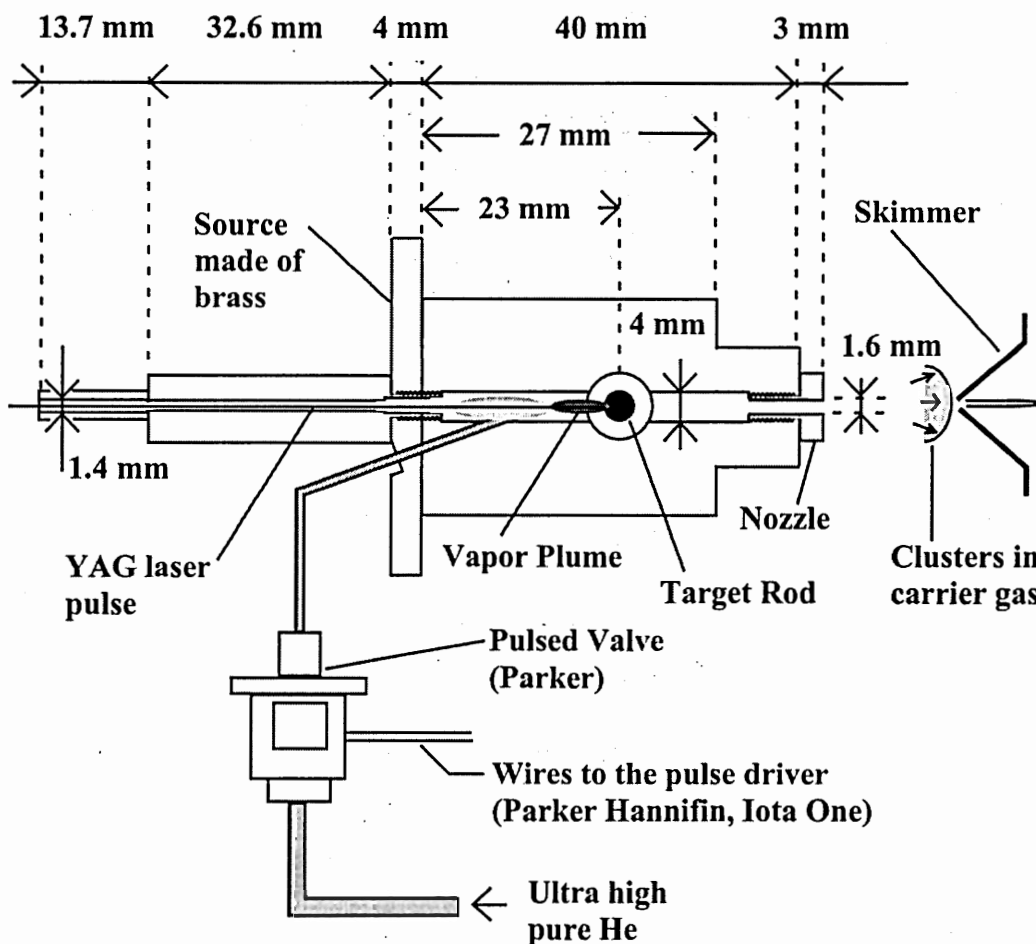


Figure 6: A laser-vaporization source for metal clusters. The in-line design allows precise alignment of the beam. The target rod is inserted laterally which allows changing samples without breaking vacuum. The YAG laser (Continuum, Surelite I-20) pulses for 6 ns (full width at half the maximum) delivering 55 mJ at 355 nm. The laser evaporates atoms of the surface of the sample and they make a plume of hot plasma. A pulsed valve (Parker) opens for 1 ms, injecting ultra high pure helium in the small cavity where the sample sits. The evaporated atoms are cooled down by the gas and coalesce to form clusters. The gas exits the source through the nozzle, carrying the clusters along. At the exit of the nozzle there is a skimmer that communicates the first two vacuum chambers and allows only the center part of the beam to pass.

One first attempt to get low temperature beams was to cool down the source. The pulsed valve operated at room temperature so that the gas entered the cavity at 300 K and was cooled in the source. This scheme worked reasonably well for intermediate temperatures, in the order of 100 K, but not below. What happens is that the colder the gas is, the more difficult it is to cool it down since the heat conductivity is proportional to $T^{2/3}$ in helium [CRC Handbook, 1980, page E-3].

$$K = 1.5 (T / 300 \text{ K})^{2/3} \text{ mW K}^{-1} \text{ cm}^{-1} \quad (8)$$

Where K is the heat conductivity and T is the temperature.

A numerical calculation shows that in the case of our source, the time needed to cool the gas from room temperature to 20 K is of the order of 10 ms, while the residence time of the gas in the source is only 1 ms. To solve this problem a different source design was needed.

The improved version involves two pulsed valves. The first one operates at room temperature and injects the gas into a reservoir where it can stay for up to 50 ms. Then, after the gas is already cooled, the second pulse valve injects the gas into the source. This way we are sure that the gas is at the temperature of the source. This design required that we had to build our own pulse valve, because there is no commercial valve available that operates at 20 K. Figure 7 shows this cryogenic source. The confirmation that this source really cools the gas down came from measurements of the speed of the beam (see below).

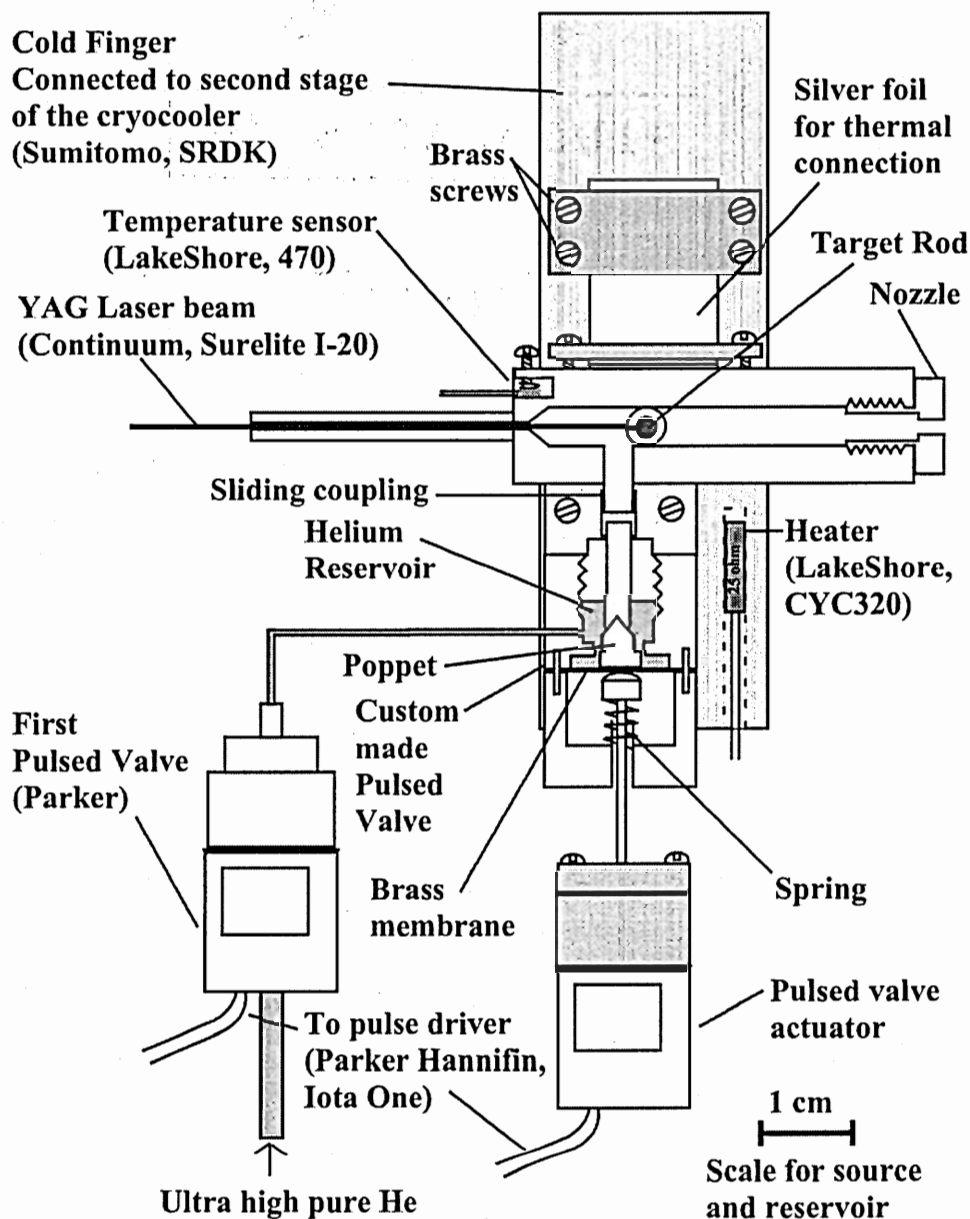


Figure 7: Schematic diagram of the cryogenic cluster source. The second stage of a cryocooler (Sumitomo, SRDK) is connected to a cold finger that cools down the source and a reservoir. The first pulsed valve (Parker) injects the gas into the reservoir. It stays there for 40 ms and a special pulsed valve controls its injection into the source. A silicon diode is used to measure temperature. The source and reservoir are drawn to scale. A 25-ohm heater is used to control the temperature. Brass screws are used to avoid loosening at low temperatures. The cold finger, source and reservoir are made of copper. The connection between the cold finger and source is through 30 layers of silver foil pressed together.

Both, the source and reservoir are connected to the second stage of a cold head (Sumitomo, SRDK), which reaches $T = 4 \text{ K}$ with a load of 1 W . Under operating conditions with the source in place the lowest temperature that we can get is $T = 9 \text{ K}$.

Some important details in designing the cryogenic source include:

- Establishing a way to check alignment with the rest of the machine and make adjustments. This is important since at low temperatures the cold finger shrinks by about 2 mm . In our design there are three screws that can be tightened to adjust the position of the source which sits on a thick o-ring. And because we can remove the sample from outside we can check the alignment by looking directly through the source.
- The first chamber is at rough vacuum of 10^{-2} Torr so the heat losses due to convection are high. This problem is compounded with the fact that the gas is dumped in cycles of high instantaneous pressure. The way to solve this problem was by surrounding the second stage of the cold head and part of the source with a protective jacket that could be pumped from the next chamber, so the pressure was 10^{-4} Torr inside the jacket. The only parts of the source exposed to the pressure of the first chamber were covered with insulation for additional protection.
- The temperature is measured with a silicon diode (LakeShore, 470) that is placed in contact with the source.

- To be able to control the temperature there is a 25-ohm heater (LakeShore, CYC320) attached to the source. An external proportional, integral and derivative regulator (LakeShore, 321) controls the current.

2.3 Deflection Plates

To generate the inhomogeneous electric field we use a pair of brass plates (figure 8). One plate is grounded while the other is connected to a voltage source. We can safely apply 20 kV without electrical breakdown in the vacuum chamber. In our experiments the plates are curved, which produces a force on the particles. Flat parallel plates were used in control experiments.

The cross section of the deflection plates is depicted in figure 8(a). The gap between the plates has a minimum of 2.4 mm. The most curved side has a radius of 2.7 mm and it is 5.1 mm for the less curved side. In figure 8(b) the high voltage connection is shown, it is made by a feed-through insulator, rated for 25 kV (Kurt-Lesker, EFT). The high-voltage source (FUG, HCN 35-35000) is controlled by the data acquisition computer and switches on and off every minute. The cluster beam is collimated so that only a narrow (0.3 mm) and short (4 mm) area of the electric field is used. In the calibration of the machine the deviations of field and gradient in that region are taken into account to calculate the average electric field and gradient.

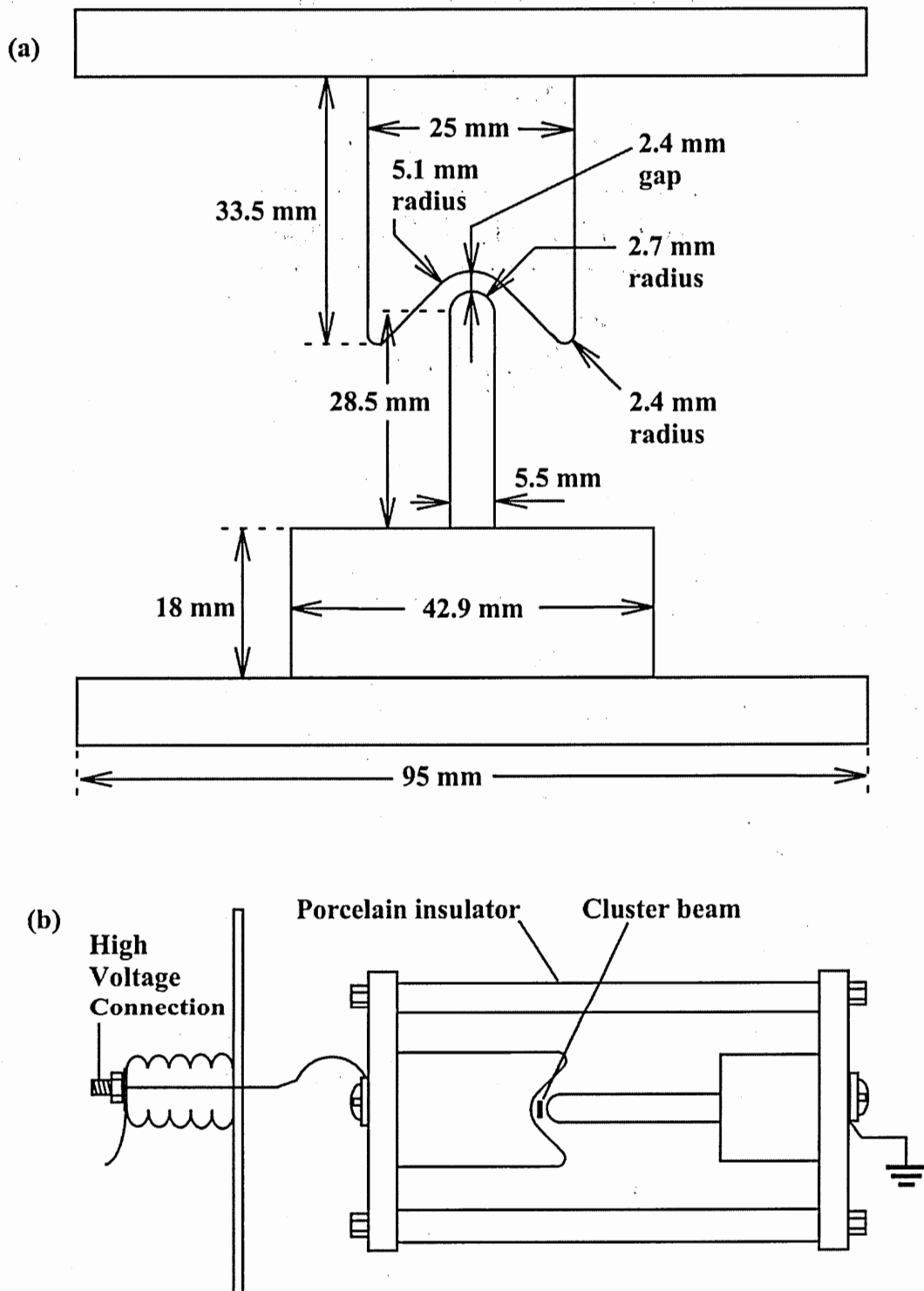


Figure 8: (a) Cross section of the electric deflection plates used in the experiments. (b) Schematic of the electric connections of deflection plates.

The force on a particle in a field is given by equation 9.

$$\vec{F} = -\nabla U \quad (9)$$

Where U is the potential energy. In the case of a particle with polarizability α , the energy in an electric field E is given by equation 10.

$$U = \frac{1}{2} \alpha E^2 \quad (10)$$

So the force in the x-direction acting on this particle becomes:

$$F_x = \alpha \vec{E} \cdot \frac{\partial \vec{E}}{\partial x} \quad (11)$$

If the electric field is in the x-direction this equation can be written:

$$F_x = \alpha E_x \frac{\partial E_x}{\partial x} \quad (12)$$

In the case of a particle with a permanent dipole moment P , the energy is given by the following equation:

$$U = -\vec{P} \cdot \vec{E} \quad (13)$$

If the electric field is in the x-direction the force will be:

$$F_x = P_x \frac{\partial E_x}{\partial x} \quad (14)$$

Where P_x is the projection of the dipole moment on the x-axis. Notice that this equation is also valid for a polarizable particle where:

$$P_x = \alpha E_x \quad (15)$$

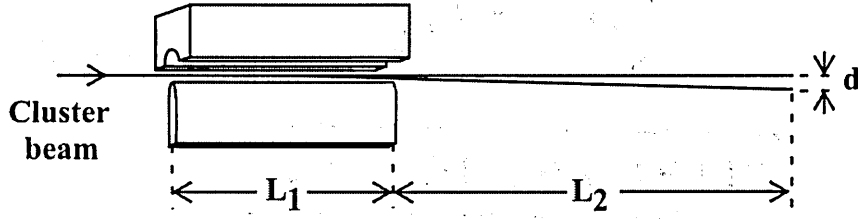


Figure 9: Distances involved in calculating electric deflections. L_1 : length of the deflection field, L_2 : distance from field to detector, d : cluster deflection.

The geometry of the trajectories and the plates is shown in figure 9. Given these parameters and using equation 14 for the force the deflection is given by the following equation:

$$d = P_x \frac{\partial E_x}{\partial x} L_1 \left(\frac{L_1}{2} + L_2 \right) \frac{1}{v^2} \frac{1}{m} \quad (16)$$

Where d is the deflection, P_x is the projection of the dipole moment (either induced or permanent) on the axis of the electric field, L_1 is the length of the electric deflection plates, L_2 is the distance between the plates and the detection region, v is the speed of the beam and m is the mass of the cluster.

Note that deflections are inversely proportional to the square of the speed. Also, if the particle studied is polarizable, P_x will be proportional to the electric field and because the derivative is also proportional to E , deflections will be quadratic with the field.

2.4 Speed Measurement

To measure the speed we use a chopper (see figure 5). This consists of a motor attached to a pair of blades that chop the beam at the exit of the first skimmer. As indicated in figure 10 the chopper allows a narrow pulse of clusters to be transmitted. When the clusters are detected we observe this narrow pulse and determine the time interval from the chopping of the beam to the arrival at the ionization chamber. Since we know the distance between the chopper and the ionization point (2.45 m), the speed is determined.

Because the motor works in vacuum its brushes cannot be made out of carbon, because they will only last for a couple of hours. The motor we use (Portescap, 22S) has precious metal brushes that should last several years.

When one of the blades is obstructing the beam, the other one is obstructing the light in a sensor placed at exactly the opposite side. This way the signal from the sensor coincides with the chopping of the beam and is used for timing and to synchronize the triggering of the experiment. Care was taken to assure that the two events happen simultaneously.

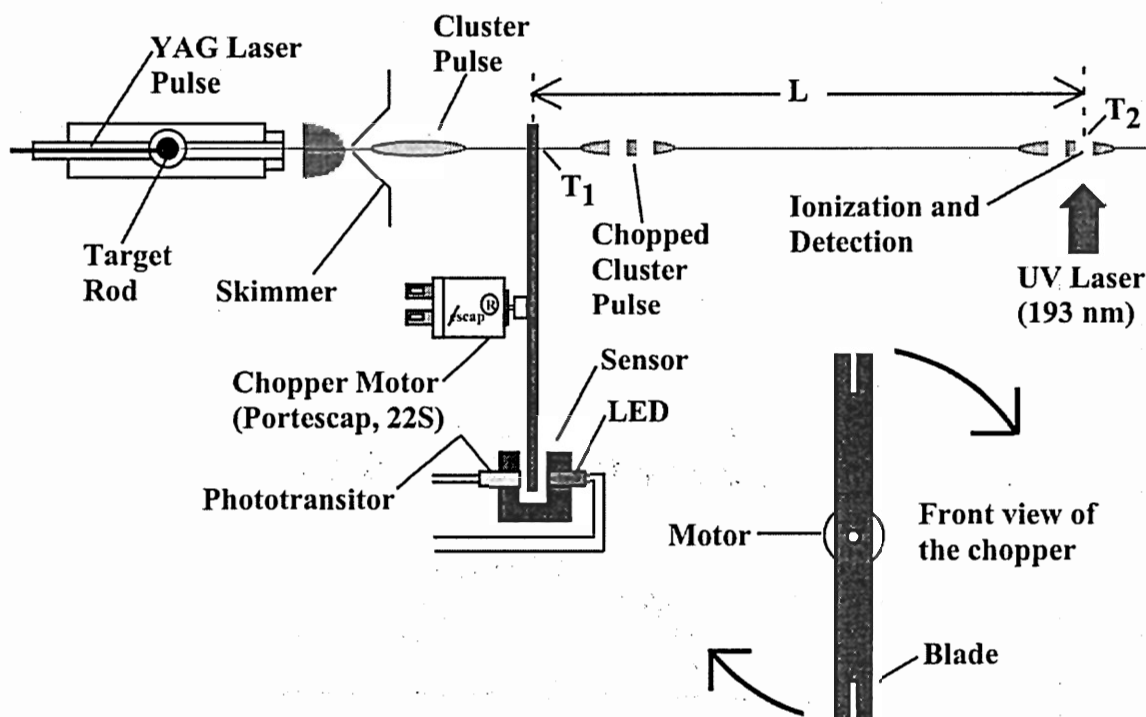


Figure 10: The speed is measured by chopping the beam and detecting the loss of signal. The chopper consists of an electric motor (Portescap, 22S) with a pair of metallic blades attached. It normally runs at 6000 RPM. The sensor, which determines the position of the chopper blades, has a phototransistor illuminated by an LED. When a blade is in the path of the light it is detected by the phototransistor as a high impedance state and at the same time the opposite blade is in the path of the cluster beam. The distance between the blades and the detector is known ($L = 2.45$ m) and we measure the time between the chopping of the beam and the detection ($T_2 - T_1$) to determine the speed.

An actual example of how the intensity is lost as time is changed is shown in figure 11.

The particular example shown corresponds to a cobalt cluster beam, but it applies to any cluster beam. The sharp central intensity peak is clearly distinguished. The typical accuracy of the speed measurement is 1.5% (accuracy of the average speed measured).

Notice also that the beam disappears uniformly, which shows that different cluster species have the same speed regardless of their masses.

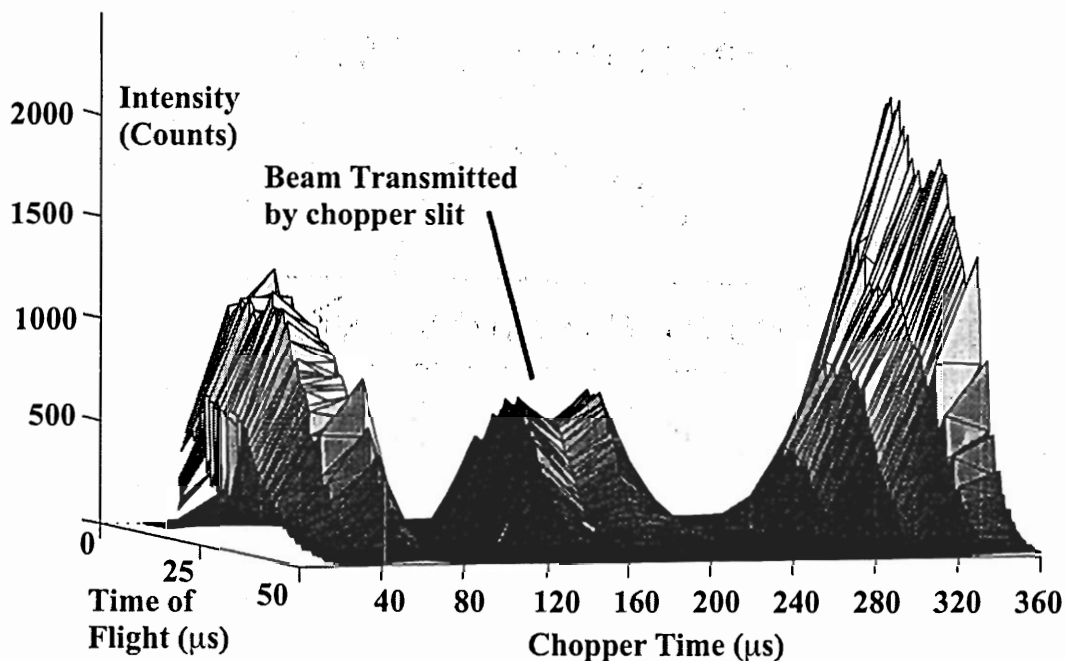


Figure 11: The chopper clips a cobalt cluster beam. Eighteen mass spectra are presented taken at different chopper times. The Time of Flight axis goes from zero to 50 μs and covers clusters up to Co_{85} . When time is too short or too long the blade misses the beam so everything is transmitted. Depletion happens when timing is right and the transmitted signal in the middle is due to the slit in the blade of the chopper.

The speed is measured under the same conditions used in the experiment. In particular we keep the time between the YAG laser and the excimer constant. Figure 12 shows the timing of the apparatus when measuring the speed. One of the blades of the chopper triggers the experiment (the signal is divided by ten, so only one out of ten pulses is really a triggering signal). We can adjust the delay between that signal and the following steps by using three delay-pulse generators (Stanford Research Systems, DG535). About 1 ms before the YAG laser the second pulsed valve opens letting the cold helium enter the cavity. Then the YAG laser pulses and ablates the target rod. Clusters are formed and they exit the cavity. The beam starts traveling the 2.51 m towards the detector, passing

through the collimators and in between the electric deflection plates. The same blade of the chopper crosses now the path of the beam, chopping it if the timing is right. At about 10 ms later the beam gets to the mass spectrometer. The excimer laser (Lambda Physik, Optex) pulses for about 8 ns ionizing the clusters. 10 μ s after the excimer laser the voltage switch closes creating an electric field that accelerates the ions. At the same point the TOF analyzer starts timing the flight and will record the arrival of the signal from this instant.

Once we observe the depletion of the beam it will mean that the blade of the chopper is cutting the beam. We know the delay between that blade and the YAG. We also know the time between the YAG and the excimer laser because it is a fixed time (the same used in the normal experiment). All we need to know is the time between two blades to know how long it takes for the beam to get from the chopper to the mass spectrometer.

Notice that the TOF analyzer starts at the same time as the closing of the high voltage switch. If the switch closed before the excimer laser or at the same time there would be an uncertainty of 8 ns in the starting of the flight which would spoil the resolution, that is why there is a delay between these two events. Also, we should mention that the time between the excimer and the YAG laser is chosen to get maximum intensity of the beam and it depends on the temperature.

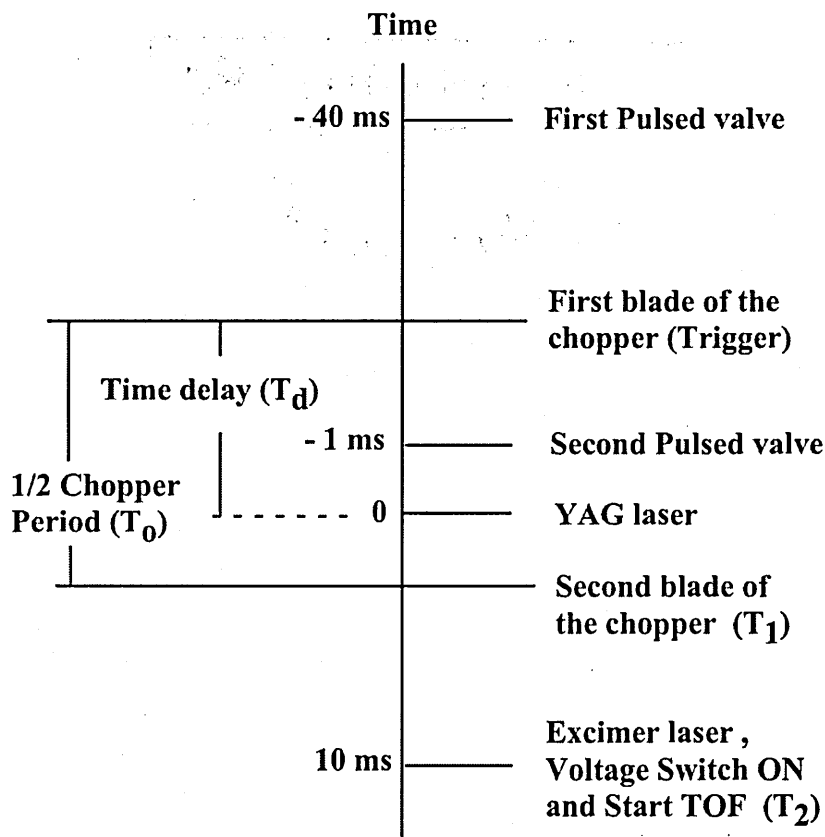


Figure 12: Timing sequence for the experiment. The time axis is not at scale. The sequence starts with the first pulsed valve (Parker) that fills the reservoir with helium at room temperature. Later, one of the blades of the chopper crosses the path of the cluster beam triggering the rest of the time sequence. The gas, already cold, is injected when the second valve opens. Then the YAG laser pulses (Continuum, Surelite I-20) evaporating some atoms from the surface of the sample. With the cold gas, clusters are produced which start going towards the mass spectrometer. If timing is right the second blade of the chopper chops the beam and that is observed as a depletion of signal at the detector.

In order to measure the speed of the beam we need to know the period of the chopper. To do this we treat the signal from the chopper to produce a single square wave that has a width equal to the time between two blades. Then, this signal is timed.

When the chopper is running the motor turns at 6000 RPM (100 Hz). The blades interrupt the beam (and the light in the sensor) twice per revolution, these events are synchronized so when the light is obscured the other blade is in the way of the beam. This produces the signal shown in figure 13a at the sensor output. The signal is inverted in a TTL chip as shown in figure 13b and sent to a one-shot circuit. This produces a single square wave of 1.1 ms duration and period equal to the time between two blades of the chopper as shown in figure 13c. Then the signal is sent to a counter in a PC card (National Instruments, PCI-1200) which is programmed to divide the signal by two. The output of the counter is a single square wave with a width equal to the time between the two blades of the chopper (figure 13d). Finally this square wave is sent to the gate of another counter (which has an internal clock running at 2Mhz, figure 13e) and is programmed to start at 50000 and count down when the gate is high. The final value is read and subtracted from 50000 which gives us the time between the blades in halves of microseconds (figure 13f). One other timer in the PCI-1200 card is used to divide the signal of the chopper by ten and trigger the experiment.

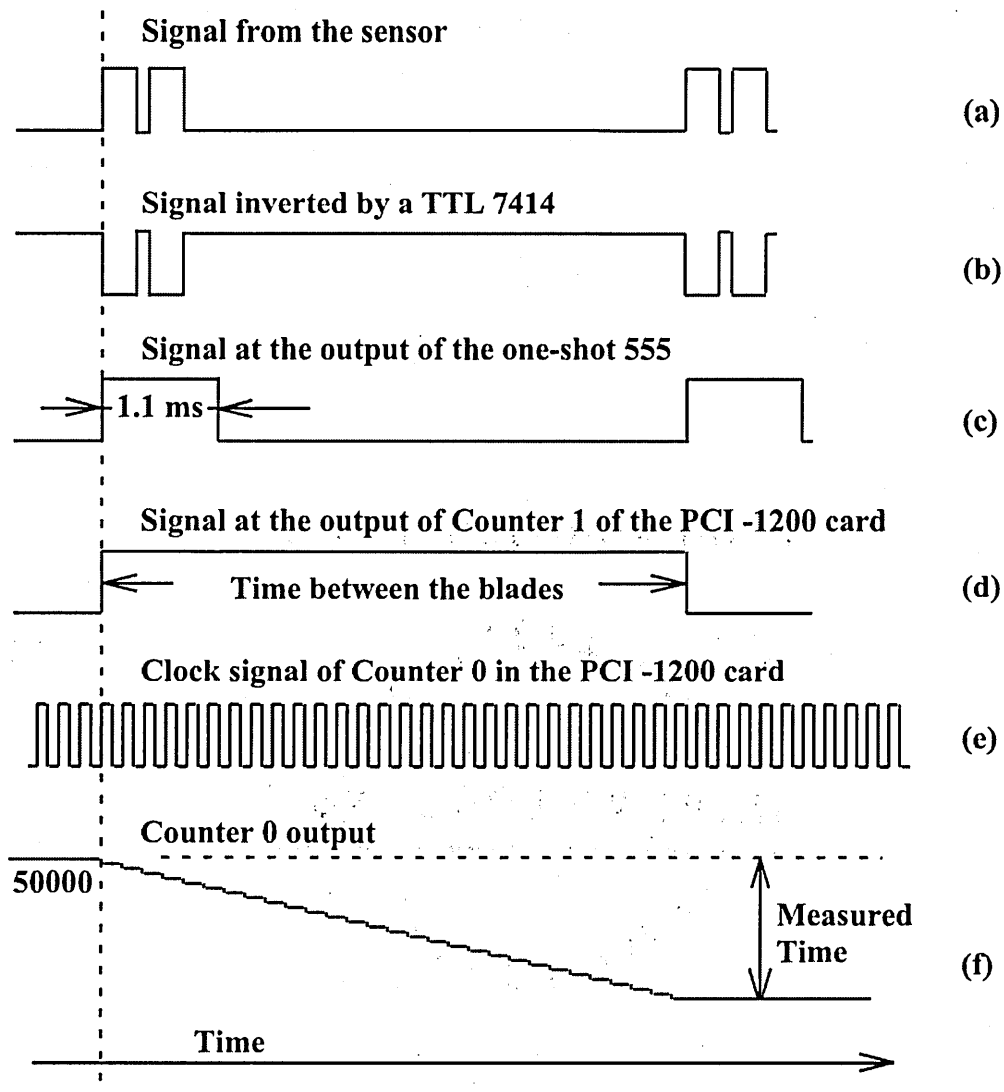


Figure 13: Timing sequence diagram. The chopper signal is treated to measure the time between the first and second blades. (a) TTL signal from light sensor. There are two notched pulses per revolution. (b) Inverted signal from the sensor. (c) Output of a one-shot circuit that gives a 1.1 ms long square wave. (d) The signal is divided by two in counter 1 of a data acquisition card (National Instruments, PCI-1200) and gives a square wave whose length is half the period of the chopper. (e) Clock signal of Counter 0, which is fixed at 2MHz. (f) Counter 0 starts at 50 000 and counts down while signal (d) is high, this way the difference between 50 000 and the final value is the time between the blades of the chopper in halves of microseconds.

2.5 Time of Flight Mass Spectrometer

The neutral clusters are ionized in the last chamber of the machine. Typically we use an ArF excimer laser (Lambda Physik, Optex) as shown in figure 14. The energy per photon is 6.4 eV which is enough to ionize all the niobium clusters except the monomer [M.B. Knickelbein, 1990]. After the clusters are ionized a high voltage switch (Behlke, HTS31) is closed applying 1200 volts to a plate and generating an electric field perpendicular to the beam velocity, which accelerates the ions. They pass through a metallic grid into a region of zero field and after passing a second grid they are further accelerated towards a third grid, which is at -7.71 kV, into a flight tube. The time of flight is proportional to the square root of the mass.

To detect the arrival of the ions a microchannel plate (MCP, Galileo) is placed at the end of the flight chamber. When a MCP is correctly polarized it generates an avalanche of electrons when it is hit by an ion. These electrons leaving the plate are at -5.5 kV and are accelerated towards a grounded grid. Beyond the grid an anode plate collects the electrons and generates a current pulse, which is amplified (Amplifier Ortec, 9327), discriminated and sent to a multi channel analyzer (Fast Comtec, 7886) where it is recorded. This analyzer also records the closing of the voltage switch and so measures the time of flight. It works at 2 GHz, so the bins where the pulses are counted are 0.5 ns in width, which defines the ultimate time resolution of the TOF.

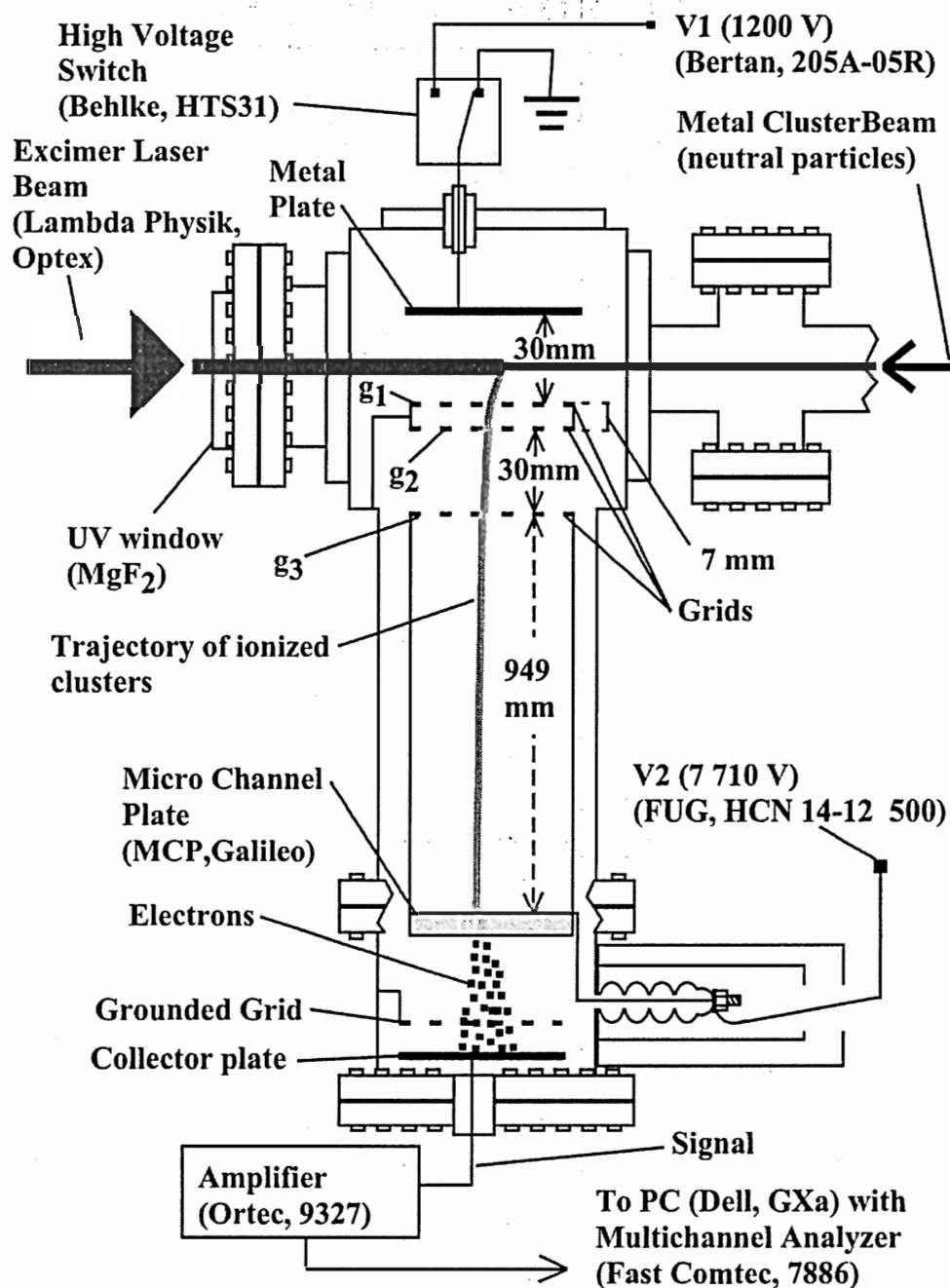


Figure 14: Schematic of the time of flight mass spectrometer. Clusters are ionized by the excimer laser (Lambda Physik, Optex, 193nm, 6.4 eV) and accelerated by an electric field towards a pair of grounded grids. Later, they are further accelerated towards a third grid and a micro channel plate (MCP, Galileo). The impact of the charged cluster on the MCP creates an avalanche of electrons that are collected in a plate. The signal is amplified (Ortec, 9327) and sent to a multichannel analyzer (Fast Comtec, 7886) where it is recorded.

There are two voltages to control in the mass spectrometer. We can set those voltages in such a way that the time-of-flight is almost independent of the initial position. This mode yields very high mass-resolution as shown in figure 15. In this mode, a typical mass resolution is 5000, which means that we can distinguish a single proton in a fifty-atom niobium cluster or an oxygen atom in an 800-atom cluster.

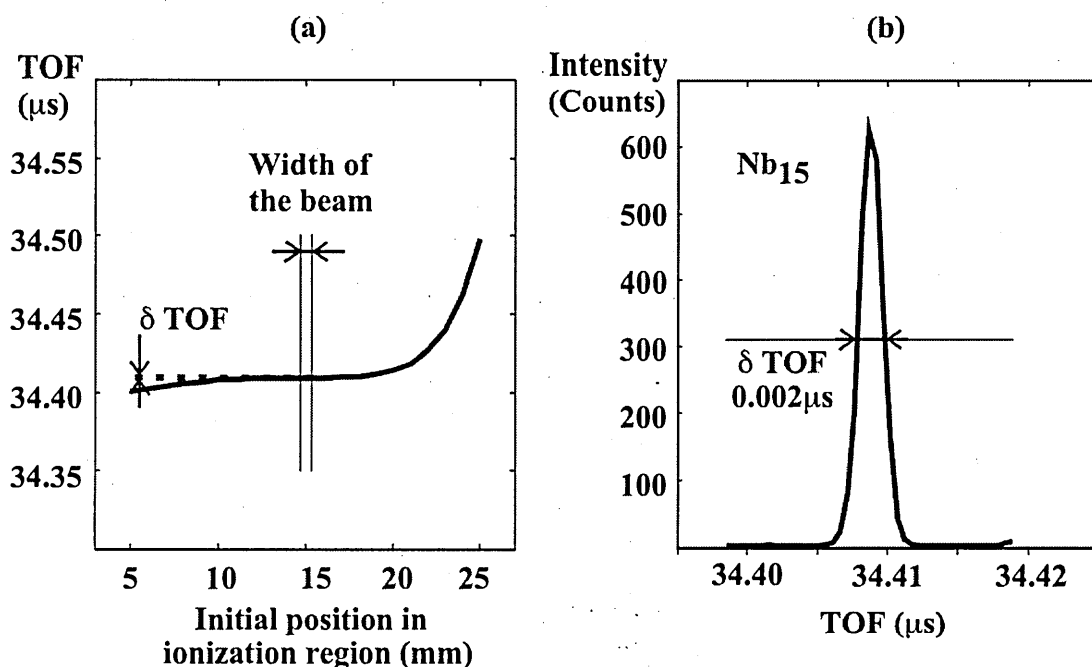


Figure 15: High-resolution mode of the mass spectrometer. (a) Time of flight (TOF) in microseconds for a Nb₁₅ cluster as a function of the initial position in the ionization region. (b) Peak profile of Nb₁₅ as a function of time of flight. The time resolution of this peak ($\text{TOF}/\delta\text{TOF}$) is greater than 17 000, which corresponds to a mass resolution ($\text{Mass}/\delta\text{Mass}$) of 8500.

In normal operation we use the position-sensitive mode. In this case one of the acceleration voltages is changed so the TOF is a function of the initial position as shown

in figure 16. The mass resolution is reduced, but it is still in the order on 1000. Enough to distinguish an oxygen atom in a 160-atom cluster. One advantage of this kind of mass spectrometer is the high volume (several cm^3) that it can handle. It is also an advantage that there is only one voltage to be tuned to get high resolution or position sensitivity. All clusters (typically 100 sizes) are recorded at the same time so experiments are time-efficient.

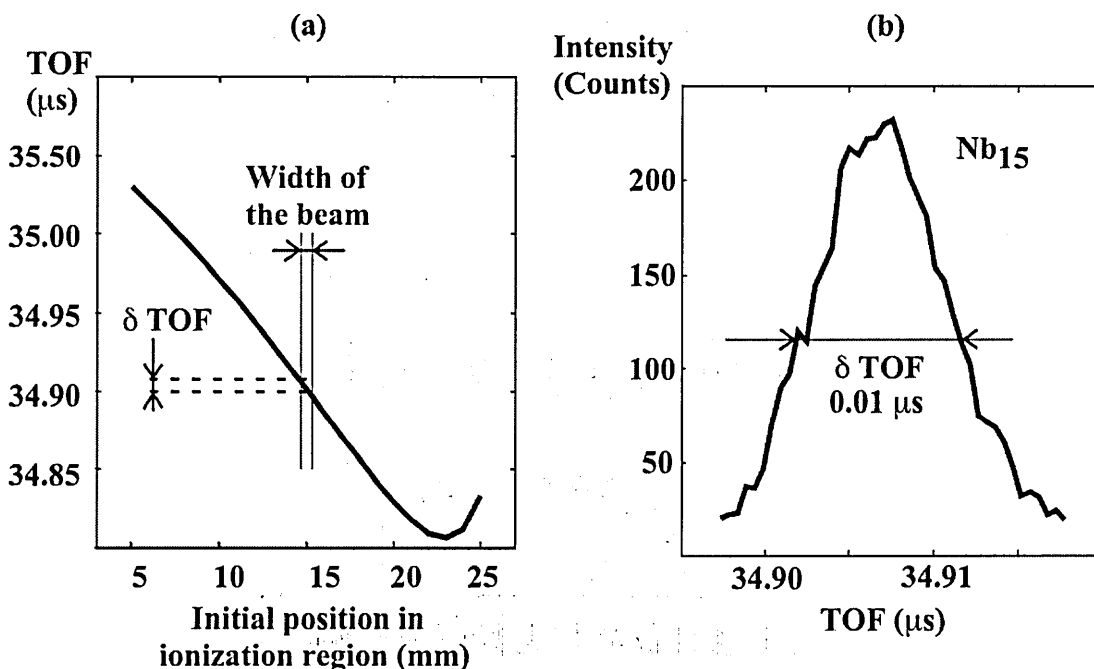


Figure 16: Position sensitive mode of the mass spectrometer. (a) Time of flight (TOF) in microseconds for a Nb₁₅ cluster as a function of the initial position in the ionization region. (b) Peak profile of Nb₁₅ as a function of time of flight. The time resolution of this peak is 3500, and mass resolution 1750.

Better mass resolution means better spatial resolution when working in the position-sensitive mode, which means less counts to get meaningful statistics in experiments. So it

is important to have as high resolution as possible. Among the factors that limit the resolution are:

- The bin-width of the multi-channel analyzer. In our case it is 0.5 ns and that would be the ultimate limit in time resolution.
- Variations in the acceleration voltages. The first voltage is switched on and off and it is typically 1200 volt. An oscillation of 1 volt would mean an error of 5×10^{-5} in time of flight (TOF). The second voltage is constant throughout the experiment (it is not switched) and typically 7.71 kV, which means an error of 3×10^{-5} in the TOF for a change of 1 volt.
- The fact that the grids are made of wires makes the electric field distorted close to the boundaries between one acceleration region and the next [T. Bergman, 1989]. This can account for an error of the order of 1×10^{-5} for a 10 000 amu-cluster in the third grid where the worst distortion happens. This error is mass dependent, the larger the mass the larger the error.
- When the machine works in the high-resolution mode the TOF is almost independent of the initial position, however after considering second order effects this can account for an error of 3×10^{-5} if the beam is 1 cm wide. This error will decrease if a narrower beam is used.

- The timing and shape of the V_1 pulse are important. A change of 2 ns in the leading edge of the voltage will reduce the resolution by adding an error of 3×10^{-5} in the TOF for a cluster of 100 amu. In this case, the larger the cluster the less affected the TOF.
- Precise alignment of the plates and grids is also important. They have to be parallel if we want to avoid distortions in the TOF. A misalignment of 1×10^{-3} radians would reduce the resolution by adding an error of 1×10^{-6} in the TOF for a 1000 amu cluster.

These sources of error are minimized to get the maximum resolution possible. Furthermore, voltage sources are chosen so they do not drift. We wait for the electronics to warm up before starting the experiments. The grids are electroformed and carefully aligned before installing and the electric switch for the first voltage (Behlke, HTS31) was chosen to have sharp transitions. Figure 17 shows an example of a high-resolution spectrum of niobium. Notice the clear separation of different species.

2.6 Calibration

To calibrate the machine we measure the polarizability of the aluminum atom, whose value is well known [P.Milani, 1990]. Given this value and the geometry of the electric deflection plates we can find the product of the electric field and its gradient. For calculations of polarizabilities that is all that is required and for dipole moments we can also find the electric field gradient alone.

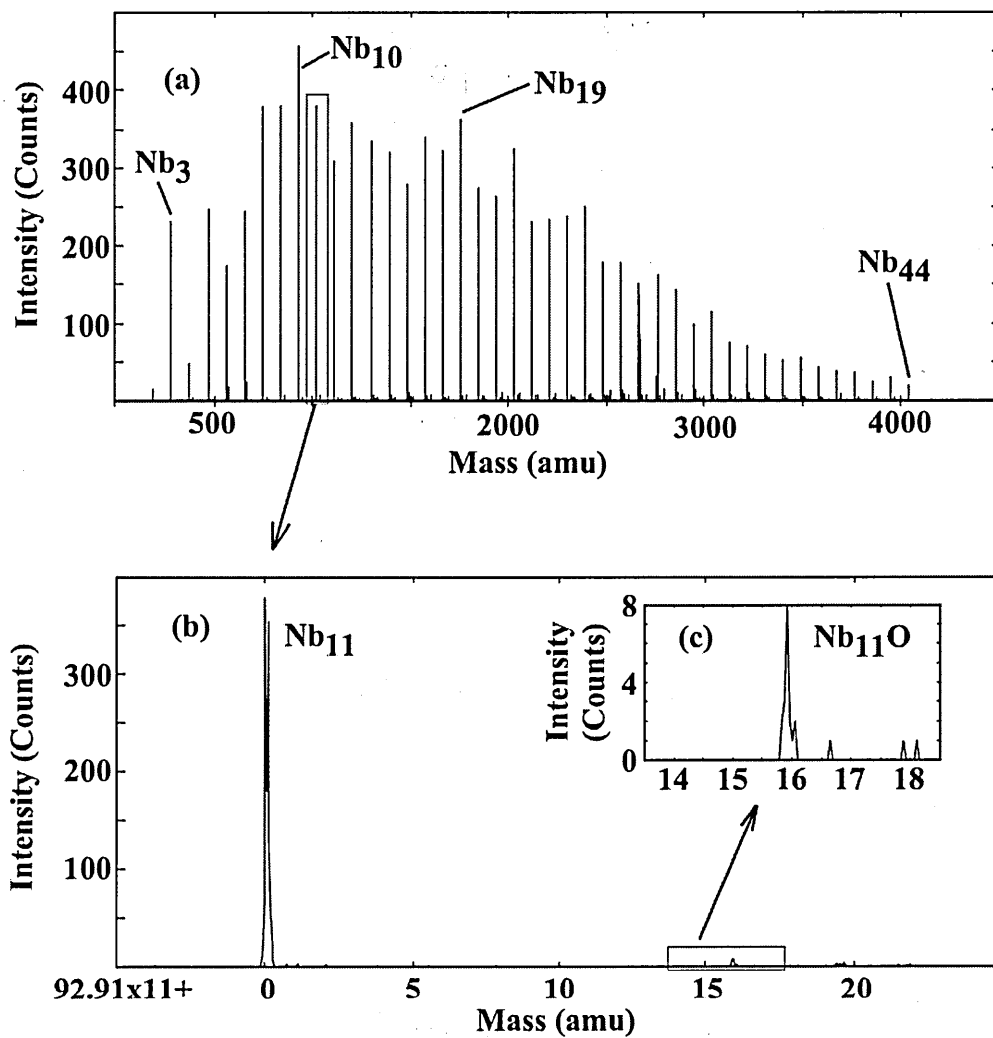


Figure 17: (a) High-resolution spectrum of niobium clusters. (b) Expanded region around Nb₁₁. The mass scale is with respect to 1022.01 atomic mass units (c) Expanded region around Nb₁₁O.

2.7 Data Analysis Methods

The time of flight data is collected in a PC-card (Fast Comtec, 7886). This card has memory bins where the counts are stored. Each shot of the experiment is added to the previous spectrum. Every minute the acquisition is stopped and the data saved in the hard disk of the PC (Dell, GXa) while at the same time changing the conditions of the experiment (changing the magnetic field, for example) and then the acquisition resumes. A program written in LabView (National Instruments, V5.0) controls these events. At the end of the experiment there are two data files, one taken with the field applied and the other without the field for comparison. These files are transferred to another computer (Apple, G4) where they are analyzed using programs written in Matlab (The Math Works, V5.2.0).

The analysis of the data starts with the identification of the peaks. The time-of-flight is used to calculate the mass and with the atomic weight we can determine the size of the clusters. Other peaks are also identified, like oxides or clusters with impurities. Then, the acceleration voltages used in the mass spectrometer determine a scale between time of flight and initial position. For example, if $V_1=1700$ V and $V_2=12000$ V (Refer to figure 14) for a Nb_{10} cluster, 1mm is equivalent to 9.3 ns. This way, deflections measured in time of flight are translated to distance.

A typical peak in a mass spectrum has a full width at half the maximum of 0.5 mm and the shape of the peak can be approximated by a gaussian. So to get an error of less than 5 microns in the position we need about 3000 counts in the peak. This normally takes a few hours to obtain.

In measurements of the zero-moment of the peaks (i.e. the total intensity as defined in equation 17, where $I(x)$ is the intensity as a function of position) counting statistical errors give an uncertainty of \sqrt{N} , where N is the number of counts. In experiments where we measure ratios, the errors of both peaks are compounded to estimate the uncertainties.

$$I_0 = \int I(x) dx \quad (17)$$

The usual way to measure deflections by calculating the first-moment of the distribution (as defined in equation 18) is susceptible of errors due to noise. That is because counts which are far from the peak (and are certainly due to noise) receive the same weight as counts that are truly due to clusters. To avoid this problem there are two approaches that we use, one is to estimate the noise level and subtract the background, or fit the data with a gaussian function. The background subtraction works well when the noise is uniform, but the gaussian fitting is the most robust method in all cases. Of course, the ideal is to have low noise levels and then all the methods converge.

$$I_1 = \frac{\int xI(x)dx}{I_0} \quad (18)$$

CHAPTER III

EXPERIMENTAL RESULTS WITH NIOBIUM CLUSTERS

3.1 Deflections at 300 Kelvin. Normal Polarizabilities

Niobium clusters at 300 K behave like normal metal clusters [R. Moro, 2003]. Deflections are proportional to the field intensity squared and the polarizability values are larger than the bulk limit as expected and seen in simple metal clusters [W.D. Knight, 1985]. Figure 18 shows a typical peak deflected by the electric field. Notice that the deflection is only of the order of 40 microns.

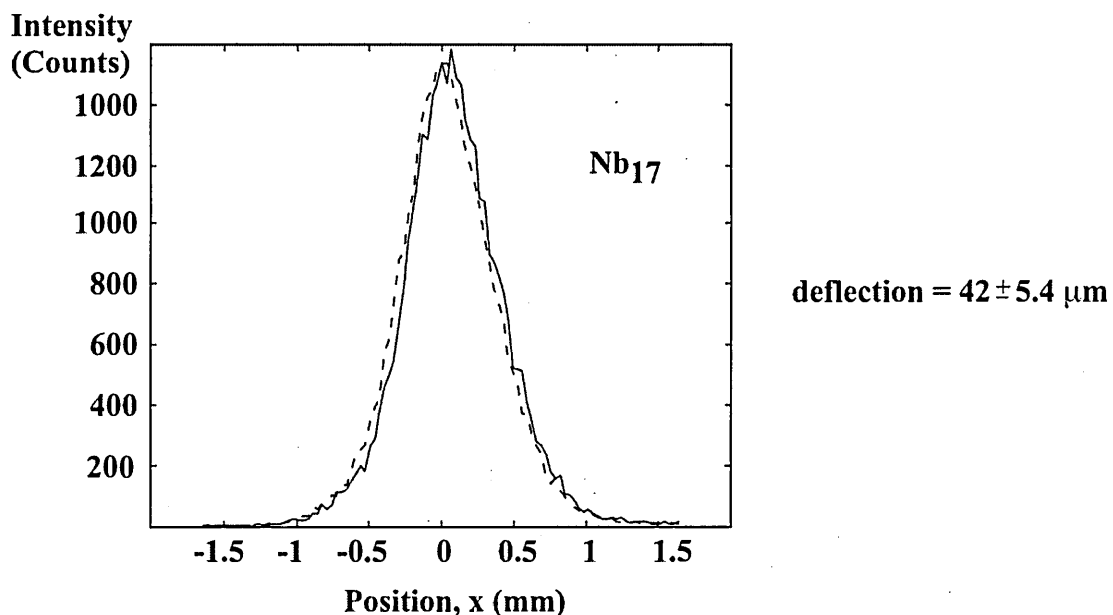


Figure 18: Position-Sensitive mass spectrum with and without electric field for Nb_{17} at 300 K. Dashed line is with field off. Continuous line is with $E = 80 \text{ kV/cm}$.

Deflections such as the one shown in figure 18 are small, but measurable and the polarizabilities calculated from these results for the range between Nb₃ and Nb₇₈ are presented in figure 19. The relatively large uncertainties are primarily caused by the very small deflections due to high speeds at 300 K. This improves as the velocity is reduced.

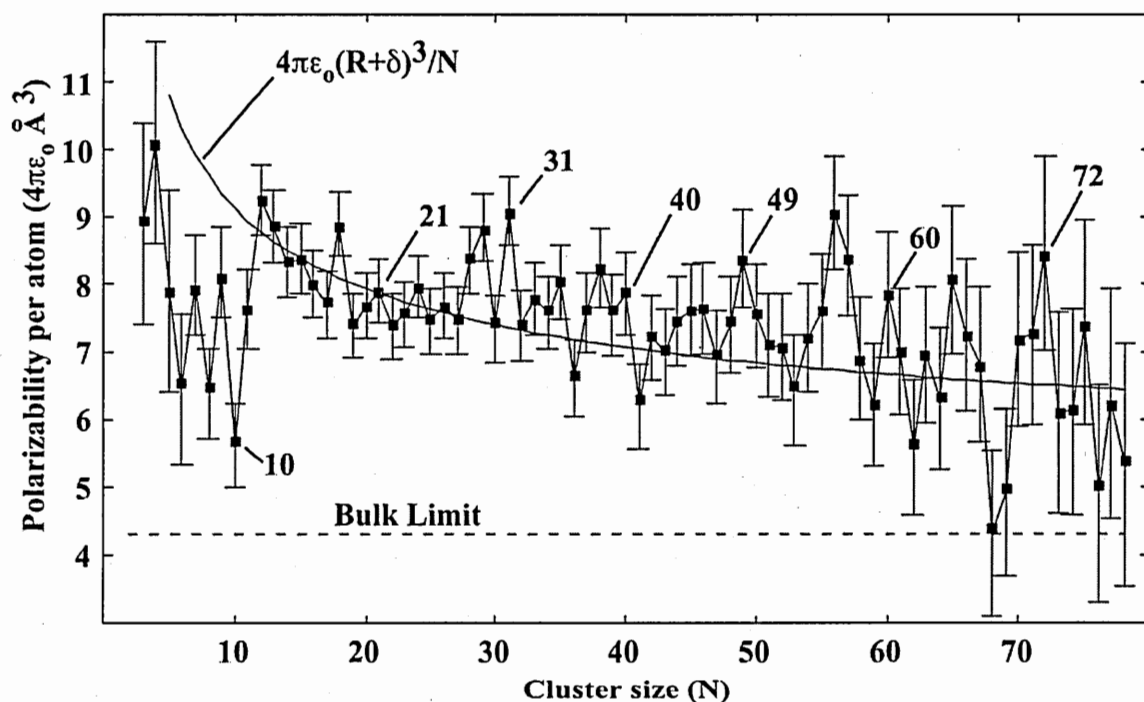


Figure 19: Polarizability per atom of niobium clusters at 300 K. Dashed line is the bulk limit and also shown is the value calculated using equation 6 for the spill-out model with $\delta = 0.1\text{nm}$.

The fact that these deflections are proportional to the electric field squared is demonstrated in figure 20 where the results of three experiments with Nb₁₅ are compared with a quadratic approximation and it fits the data closely.

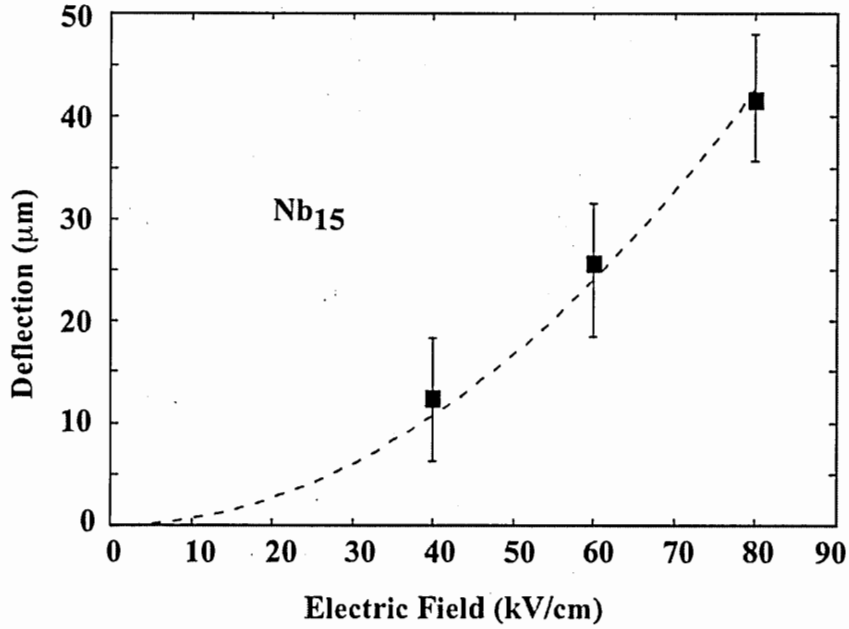


Figure 20: Deflections as a function of electric field for Nb₁₅. These experiments at 300 K demonstrate that the deflections are quadratic with applied field. Dashed line is a quadratic fit to the data.

3.2 Low Temperature Results

The qualitative behavior changes at low temperatures. Figure 21 shows the deflection profiles of some selected clusters at T=300K, 50K and 20 K.

At 50 K, besides the normal deflected component, the clusters also exhibit extended tails. The clusters in these tails are deflected several millimeters as opposed to a few hundred microns for the normal polarizable component of the beam (which correspond to the less deflected peak). Notice that the scale is logarithmic, so the amount of material in the tails

is only a small fraction of the total. A significant fraction of the clusters are deflected beyond the detector limits (i.e. more than 4.5 mm).

At 20 K an even larger fraction of the clusters is deflected beyond the spatial range of the detector. We can identify the fraction of the clusters in the normal component of the beam (for example by fitting the peak with a gaussian function) and by subtraction find the fraction that is anomalous. This fraction is shown in figure 21 as parameter "R". The fraction R hence measures the part of the clusters that deflect anomalously (exhibit a permanent dipole).

Another thing that should be noticed is that the tails are single-sided. Although there is some material deflected towards lower fields (for Nb₁₁ for example) most of the material in the tails is deflected towards higher fields (which is the right side in these figures).

Experiments at 50 K show that the extension of the tails increases with electric field. An example of this is shown in figure 22 for Nb₁₄. The data has been slightly smoothed for clarity in this figure and it includes four field intensities and also zero field for comparison.

An important feature observed is that the extension of the tails is not proportional to the electric field squared. As shown in figure 23 in the case of Nb₁₄. The linear, rather than quadratic response indicates a permanent dipole moment, so the clusters are ferroelectric.

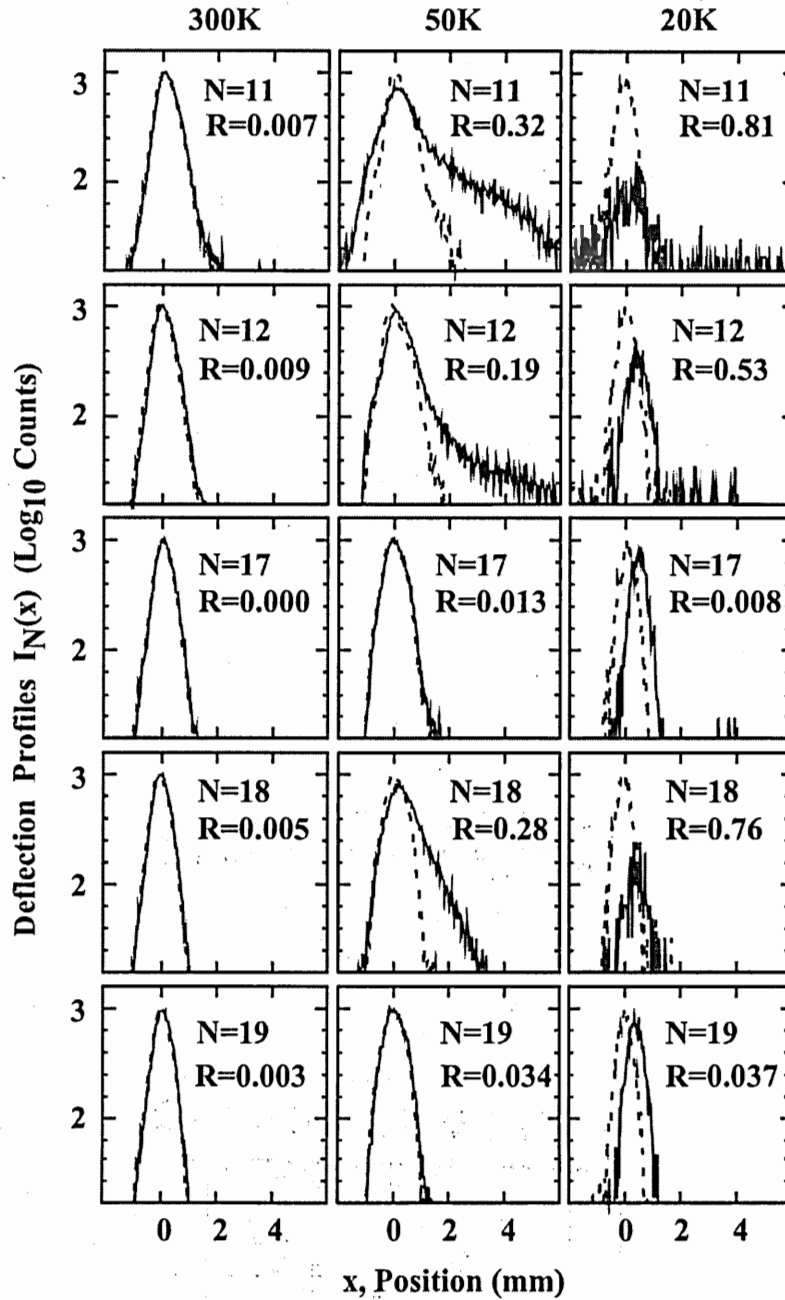


Figure 21: Representative deflection profiles of some niobium clusters at three temperatures. Dashed lines at zero field, continuous lines at 80 kV/cm. At 300 K deflections are small and consistent with normal metal clusters. At 50 K some clusters develop tails that extend several millimeters. At 20 K some clusters are deflected beyond the detector limits yielding loss of detected intensity. The fraction R of the clusters that show anomalous deflections, either detected in the tail or deflected beyond the detection limits is a function of the temperature and electric field intensity.

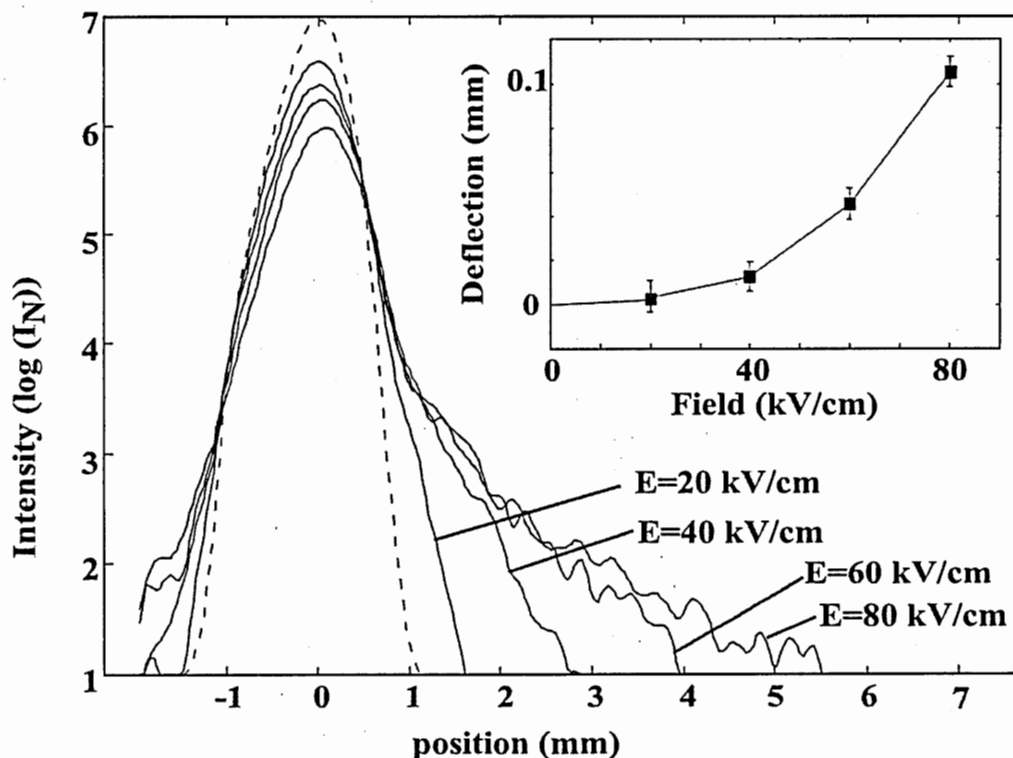


Figure 22: Deflection profiles of Nb₁₄ at 50 K and several electric fields. The dashed line is at zero field intensity. For every profile we can distinguish a main peak and a tail. The main peaks are deflected tens of micrometers. The tails instead are deflected several millimeters. Inset: Deflections of the main peaks as a function of the electric field applied, which demonstrate they are quadratic with the field.

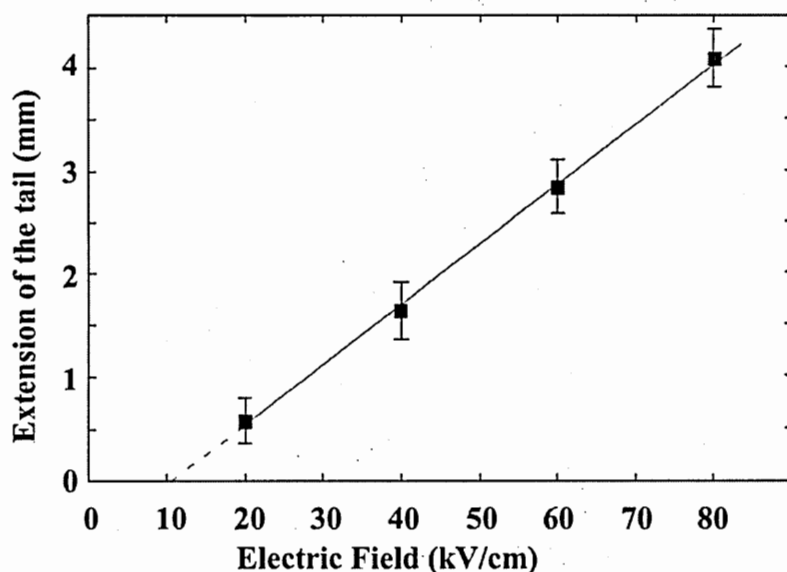


Figure 23: Extension of the observed tail for Nb_{14} as a function of electric field at 50 K. The straight line is a linear fit to the data which extrapolates to give an intercept of 11 kV/cm, which is interpreted as the electric field needed to uncouple the dipole moment.

We calculated the dipole moment associated with the visible extension of the tails. Figure 24 shows these values for clusters in the range Nb_5 to Nb_{32} at $T = 50$ K.

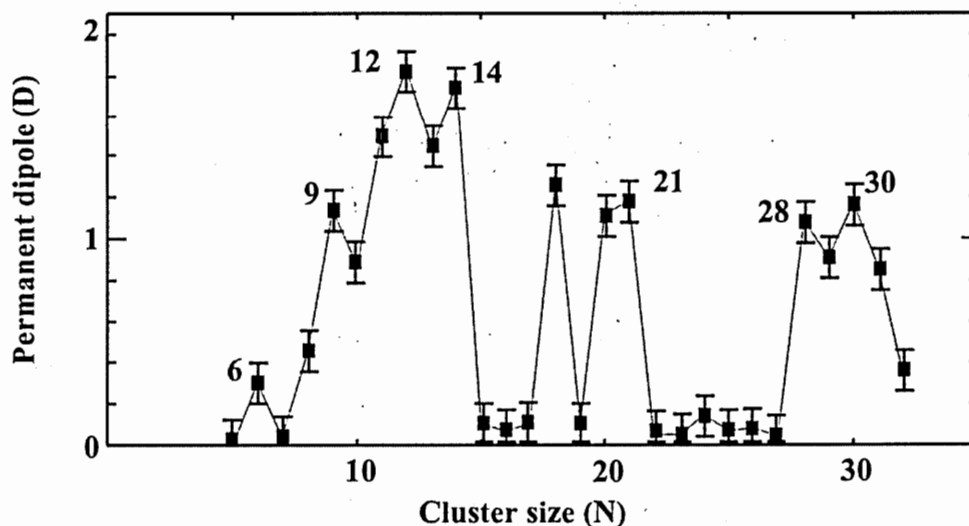


Figure 24: Permanent dipole moments calculated from the extension of the visible tails in niobium clusters at 50 K and 80 kV/cm.

R measures the fraction of the clusters in the tails (either visible or not), which we call the “ferroelectric fraction”. This parameter increases as the temperature is reduced. It also increases when field is increased, but it saturates. When the field is 80 kV/cm most of the losses are saturated (for example when going from 60 kV/cm to 80 kV/cm little material is lost). So at 80 kV/cm the clusters left are basically the ones that behave normally.

We measured deflections of the normally deflected clusters at $T=20$ K and calculated their polarizabilities. This calculation was done by measuring the average deflection of the clusters that were left and applying equation 16 to get the induced dipole and the definition of polarizability (equation 1). The results are shown in figure 25 where the $T=300$ K data is also shown for comparison. A reduction in the polarizability is found, consistent with the prediction for sodium clusters [S.A. Blundell, 2000]. The cases of Nb_9 , Nb_{11} and Nb_{14} are special. In those cases there is some material left that is deflected towards lower fields (and which is not swept by the high electric field), so the average deflection is low or negative for those clusters.

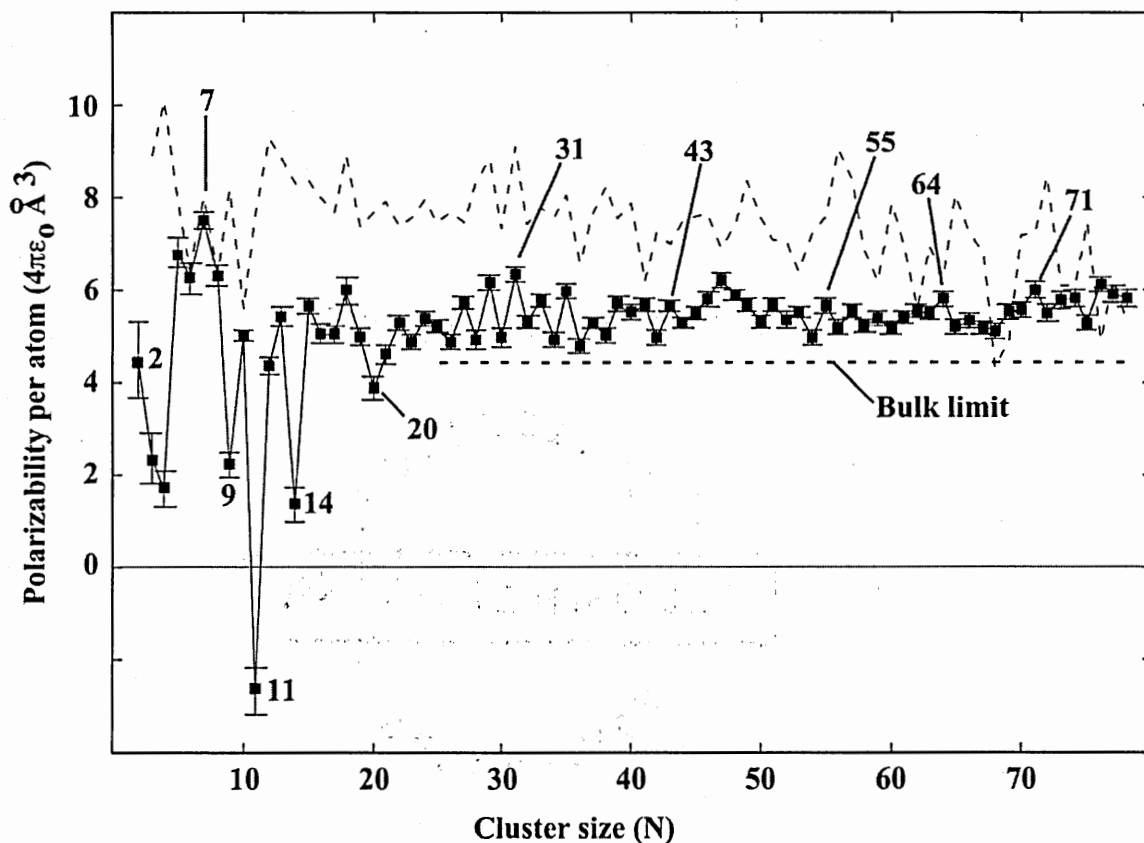


Figure 25: Filled squares are experimentally measured polarizabilities per atom of niobium clusters at 20 K. These values were calculated from the average deflections of clusters that are left after applying an electric field of 80 kV/cm (which deflects most of the anomalous fraction beyond the detector limits). In the case of Nb_9 , Nb_{11} and Nb_{14} there is a certain fraction of the clusters that are deflected negatively (towards weaker fields) and these clusters are not swept away, that is why their polarizabilities are anomalously low. The thin dashed line is the polarizability at 300 K that is reproduced here for comparison. Notice that the values at 20 K are systematically lower than the room temperature data. It is also remarkable the odd-even alternation in the region Nb_{25} - Nb_{45} with higher polarizabilities for odd clusters. The thick dashed line indicates the bulk limit.

The material in the tails (Parameter R) has been measured for several cluster sizes and conditions of electric field and temperature. An example is shown in figure 26 that presents results from two experiments done with niobium at different temperatures but the same electric field.

It can be observed that the ferroelectric fraction is a function of size. There are strong variations for small clusters. For instance Nb_{15} behaves like a normally polarizable cluster even at 20 K, while Nb_{14} has a large ferroelectric fraction. But beyond Nb_{28} all clusters show some ferroelectric fraction. It is also remarkable that beyond Nb_{38} there is a pronounced odd-even alternation, i.e. clusters with even number of electrons have a larger ferroelectric fraction than odd clusters.

To check that the losses were really due to large deflections some control experiments were done. One possibility was ionization of the clusters in the electric field. To rule out this, we used flat deflection plates (which produce a uniform field) that yielded no losses. This experiment also ruled out the possibility of depletion caused by field induced evaporation of helium atoms attached to the clusters.

An experiment covering a larger range of sizes was done and the results are shown in figure 27. The odd even alternations are visible up to 130 atoms. Also it is important to notice that the decay with size is very slow which is an indication that this property is not due to surface effects which would yield a faster decay.

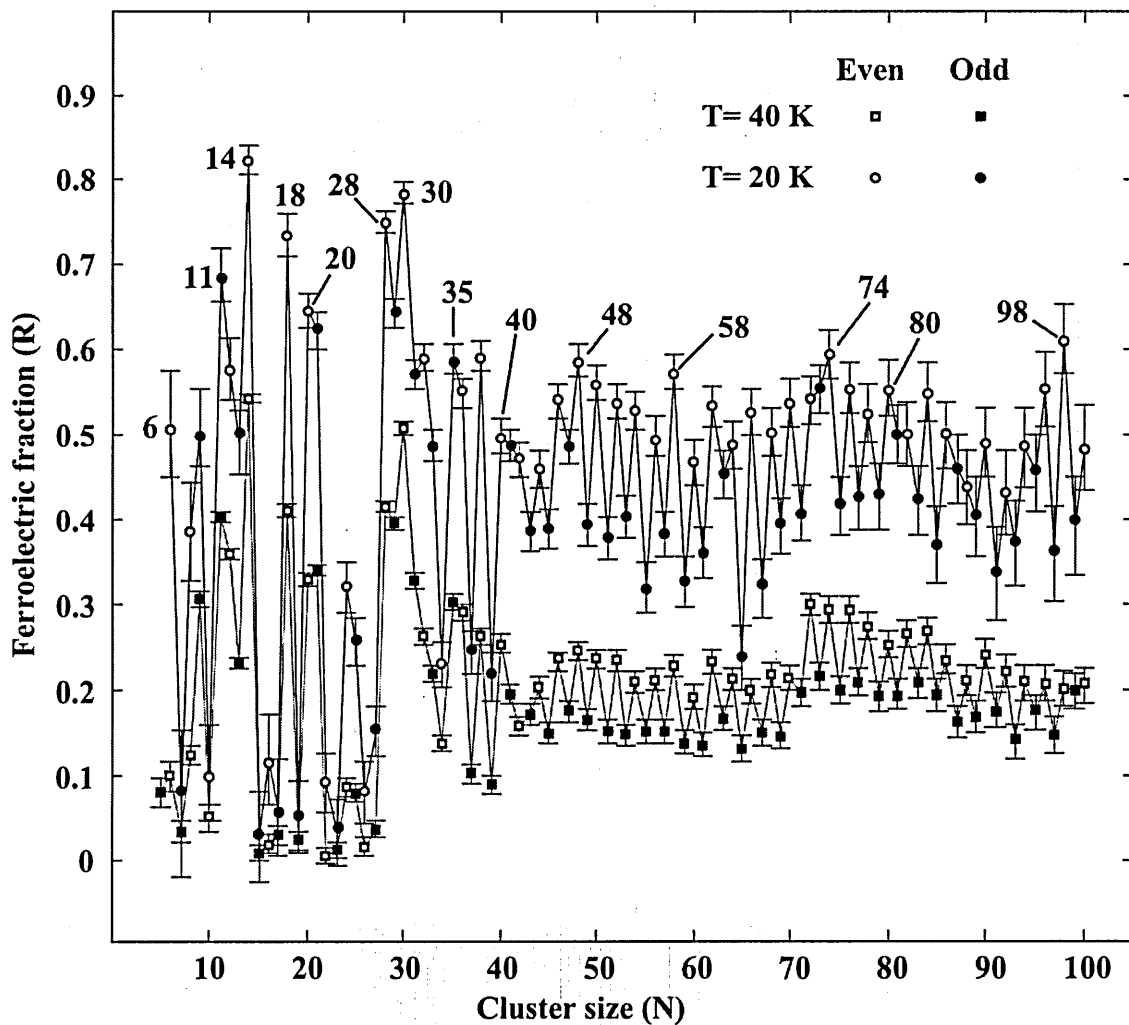


Figure 26: Ferroelectric fraction of niobium clusters at 20 K and 40 K defined as the fraction of the clusters in the tails, either visible or not. Experiments with an electric field of 40 kV/cm.

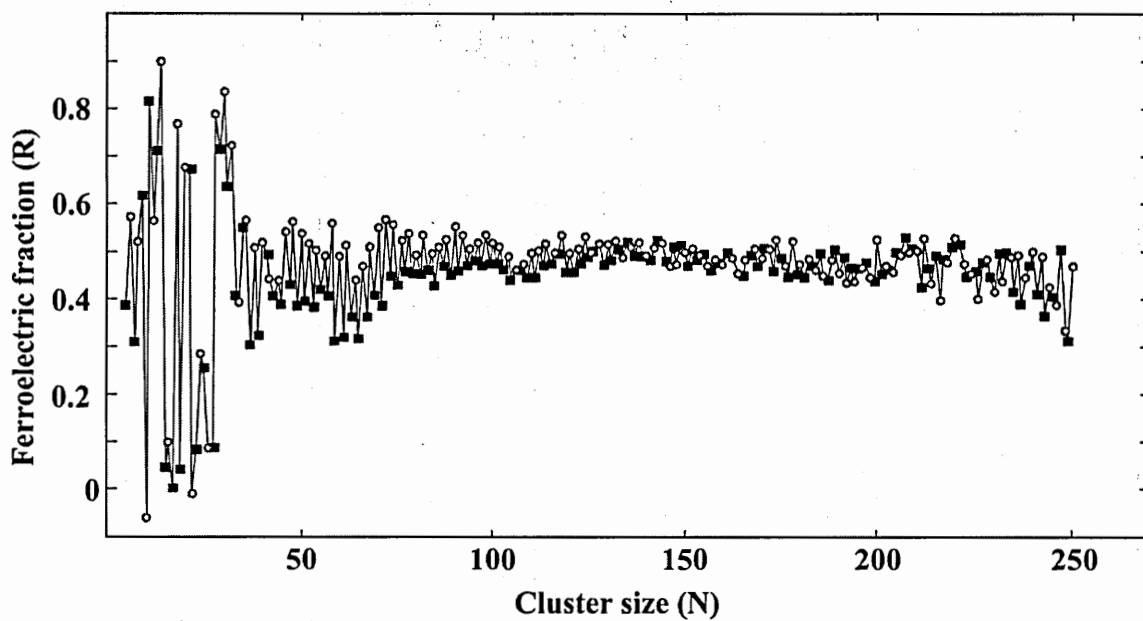


Figure 27: Ferroelectric fraction of niobium clusters measured at 16 K and 72 kV/cm. Filled squares are odd clusters, open circles are even clusters. The accuracy from counting statistics is 5.3% or better.

3.3 Simple Model to explain Field and Temperature Dependence

A permanent dipole moment causes deflections according to equation 16, but P_x (the projection of P on the field axis) will depend of how it interacts with the field and the cluster. A model has to be used to calculate the dipole from the deflected peaks. A very successful model developed by Philippe Dugourd and collaborators [P. Dugourd, 2001] applies to a variety of cases. As shown in figure 28 this model correctly describes the response of a molecule with a permanent dipole moment.

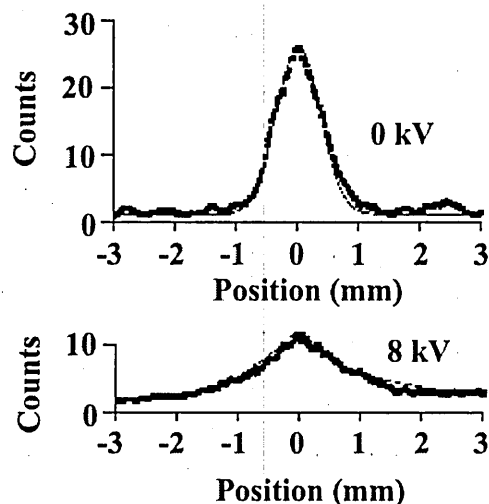


Figure 28: The model by P. Dugourd [P. Dugourd, 2001] correctly predicts the shape of the deflected peak of a molecule of Ti C_{60} with a dipole of 8.1 D. Filled squares are experimental values, thin dashed line their model prediction. The experiment at 8 kV is done with an electric field of 48.3 kV/cm.

However, we cannot use this model to describe our observations. Niobium peaks are deflected asymmetrically and the change in behavior is sudden from deflections of a few hundred microns to several millimeters. Dugourd's model assumes that the dipole is fixed on the cluster axis. Instead, in our model we relax this condition and take into account the tendency of energy levels to avoid crossings.

Our motivation to try this different approach came from [W.A. de Heer, 1991b] where the magnetic deflection of the sodium trimer was explained with the help of a Zeeman diagram. In that case the deflection profile showed two peaks corresponding to the two possible projections of the spin plus an additional peak centered at zero. The reason for that undeflected peak is that the energy levels of different rotational states avoid crossings

so they bend and yield a region of very small average slope (the magnetic dipole moment is given by the slope of the energy level).

Similarly in the case of electric dipoles we can construct a Stark diagram [C.W. Townes, 1975] and study the effect of avoided crossings. This is a diagram that presents the energy levels as a function of electric field. Note that the dipole moment is equal to the slope of the energy level (equation 19).

$$P = \frac{\partial W}{\partial E} \quad (19)$$

Notice that the quantum number M_J (projection of J on the electric field axis) is conserved, because the electric field only produces torque perpendicular to itself. Given a certain value of M_J the cluster can be in any state with J more than or equal to M_J and quantum number K (projection of J on the cluster axis). In average these states will be separated by B (the rotational constant). Now, if the dipole moment (P_0) is either aligned or anti-aligned with J the levels will change with electric field according to:

$$W = W_0(J,K) \pm E \frac{P_0 M_J}{\sqrt{J(J+1)}} \quad (20)$$

Where the sign will depend on the orientation of the dipole with respect to J . W is the energy and $W_0(J,K)$ is its value at zero field. As the field is increased, these levels will approach and avoid crossing, as shown in figure 29. That will produce two regions. One with very dense anticrossing levels (and zero average slope) and one with downwardly going levels (and large slope). This explains why the change from apparently normal

behavior to large dipole moment is so sudden when we increase the electric field. It also explains the single sided deflections observed.

The temperature and field dependence can be calculated by considering the population of rotational energy levels and finding the fraction of the clusters that are beyond the threshold of avoided crossings. Numerically it was found that the fraction could be approximated by the following equation:

$$R = 1 - e^{-\frac{P_0 E}{k_B T}} \quad (21)$$

The temperature dependence observed experimentally is stronger however. Besides it was found that R seems to saturate at a given temperature. This indicates that the population that has a dipole moment depends on temperature. The simplest model to fit the observations is to assume that a ground state exists that has a dipole moment and excited states that are normal. If we further assume that the states are equally separated by a constant energy gap the ferroelectric fraction will be given by.

$$R = \left[1 - e^{-\frac{P_0 E}{k_B T}} \right] \left[1 - e^{-\frac{T_G}{T}} \right] \quad (22)$$

Where $k_B T_G$ is the energy gap that separates the states.

This model has only two parameters. An example of fitting to experimental data is shown in figure 30 for Nb_{30} that includes results from 14 experiments.

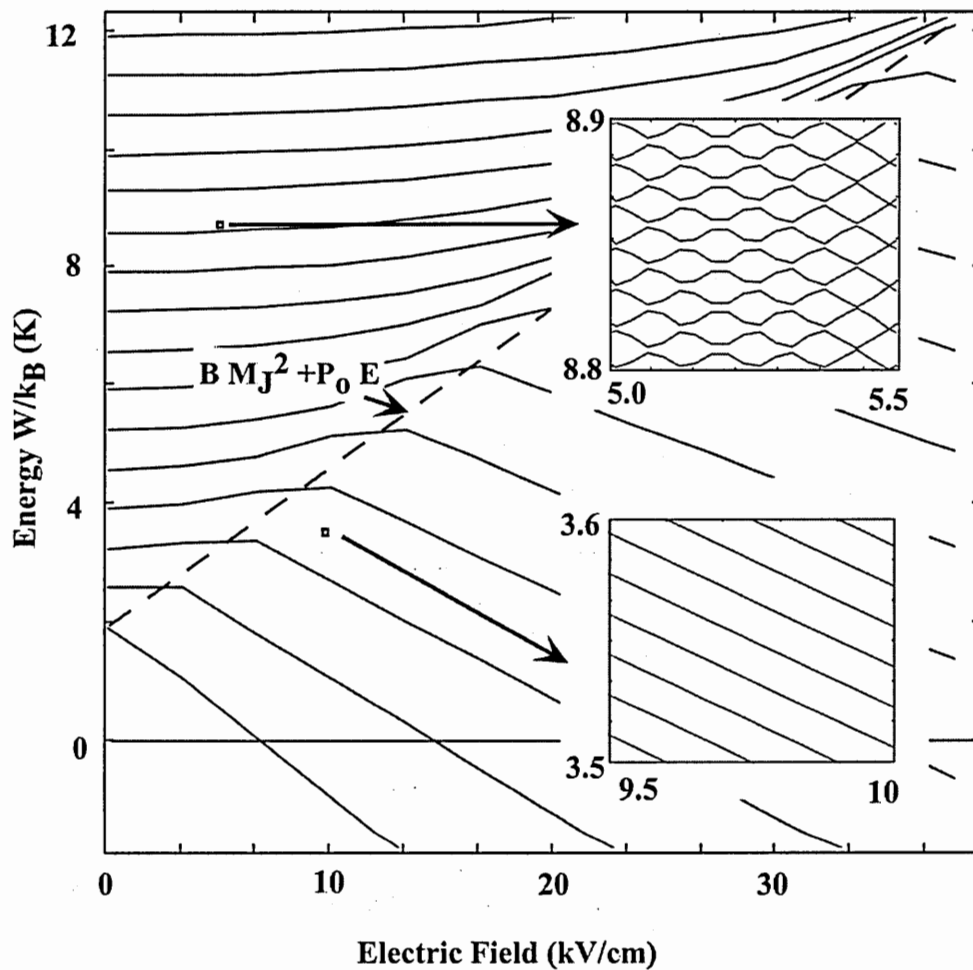


Figure 29: A Stark diagram for Nb_{12} where $M_J=10$ and $P_0=20$ D. Two regions are visible, one of dense avoided crossings that yield an almost zero slope and a region of downwardly going levels. Only every hundredth energy level is shown in the main figure. Insets show every level in the expanded region.

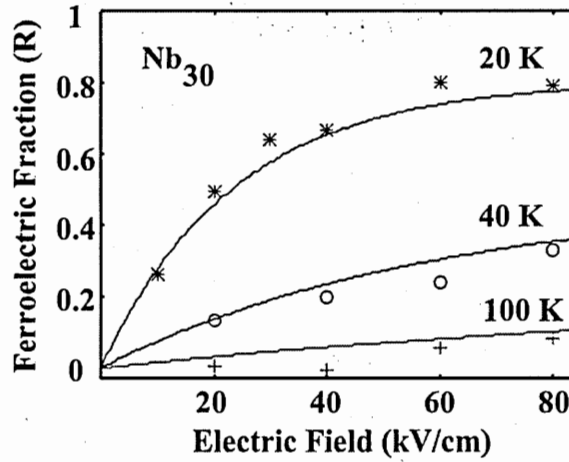


Figure 30: Ferroelectric fraction (R) experimentally measured at 3 temperatures and several electric field intensities for Nb₃₀. The continuous lines are the fitting functions calculated in the proposed model.

3.4 Transition Temperatures and Dipole Moments Calculated in the Model

Based on the model proposed we fit the experimental results and get the dipole moment P_0 and the transition temperature T_G . Figure 31 shows the dipole moment per atom of niobium clusters. The values are in the order of 1 Debye per atom in the range studied, which are comparable to the best ferroelectrics known [B. Matthias, 1976].

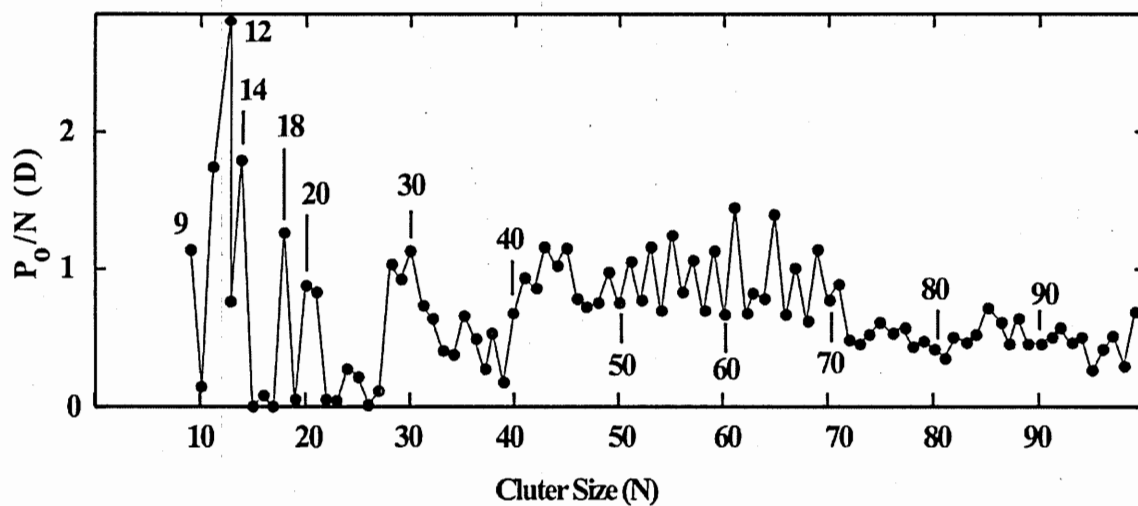


Figure 31: Permanent dipole moment per atom for niobium clusters calculated in the proposed model.

The transition temperatures calculated in the model are presented in figure 32. The maximum is found for Nb_{11} at more than 100 K and it drops and seems to approach a constant value of 10 K for large clusters.

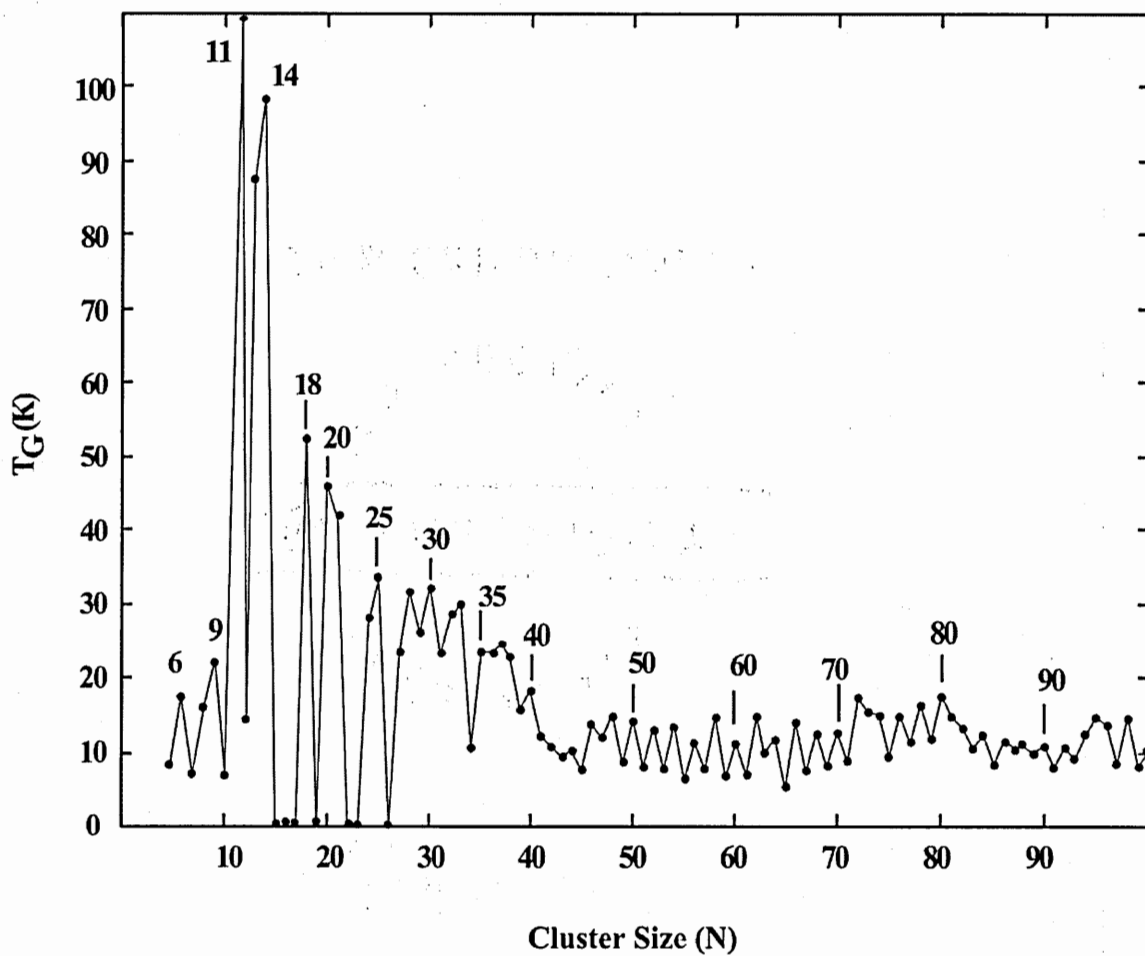


Figure 32: Ferroelectric transition temperatures of niobium clusters calculated in the proposed model.

3.5 Stern-Gerlach Experiments with Niobium clusters.

We also did magnetic deflection experiments with niobium clusters [W.A. de Heer, 2003a]. The experimental set-up is similar to the one used in polarizability experiments, only that instead of an inhomogeneous electric field a magnetic field is applied. Deflection profiles in the range Nb_2 to Nb_{13} are shown in figure 33 and figure 34.

Contrary to what has been observed in ferromagnetic clusters [W.A. De Heer, 1990], in this case responses show both, deflections towards high field and towards lower field. Notice that the dimer does respond to the magnetic field, but all other clusters with even number of electrons do not, as predicted from *ab initio* calculations [V. Kumar, 2002]. Clusters with odd number of atoms have one unpaired electron, so they all respond to the magnetic field. Notice that the shapes of the peaks are different from cluster to cluster. In particular, Nb_9 has a stronger response than Nb_7 for example.

As an additional example figure 35 shows the deflection profile for Nb_{22} where the x-axis scale has been converted to magnetic moment. The response of this cluster is almost zero. All even clusters (except for Nb_2) have similar behavior in the range studied (up to about 100 atoms). An example of an odd cluster is shown in figure 36 for Nb_{23} . Many odd clusters show this kind of behavior where a fraction of the clusters seem to be almost not affected by the field while another fraction is strongly deflected.

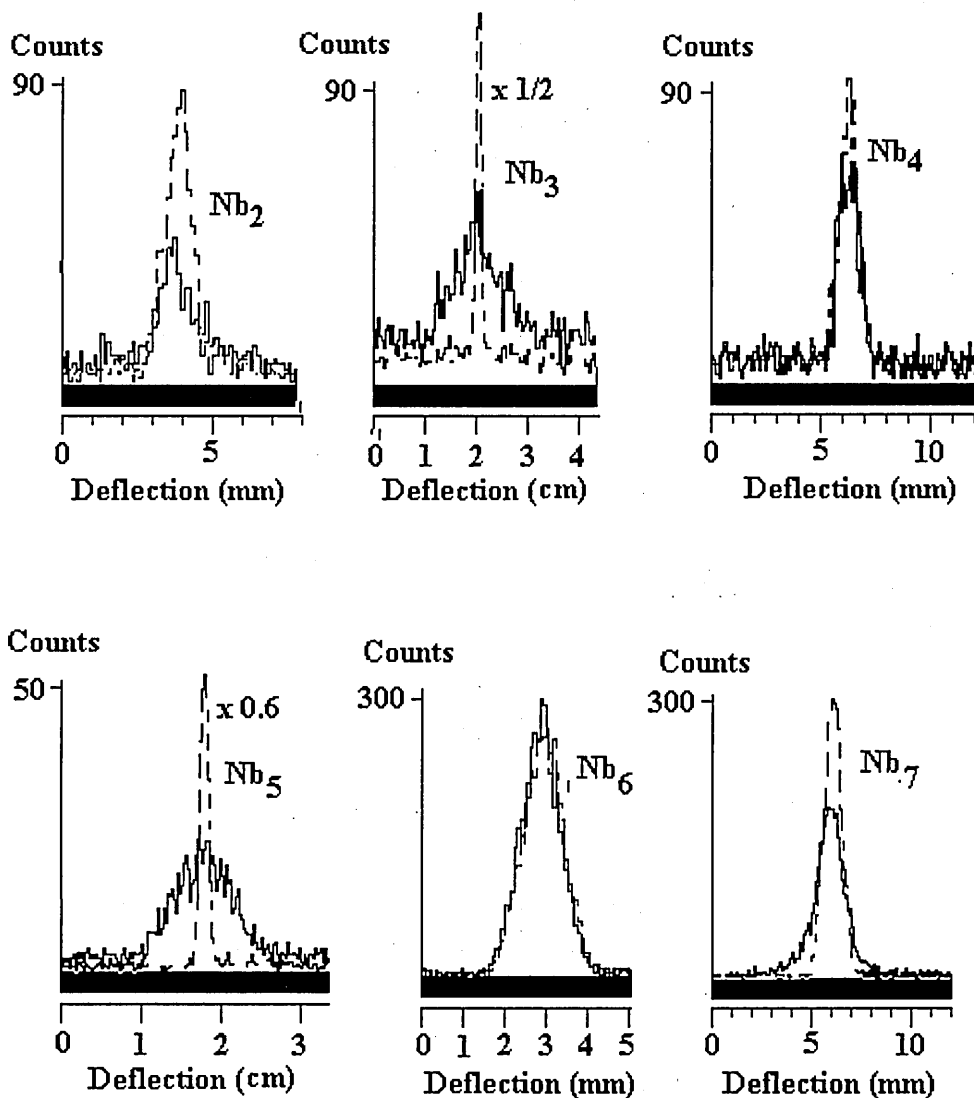


Figure 33: Niobium clusters in the range Nb_2 to Nb_7 deflected by an inhomogeneous magnetic field. The dashed line is the profile without magnetic field and the solid line is after applying 0.9 T. The experiment was done at 20 K. The niobium dimer does respond to the magnetic field as expected [A.M. James, 1993].

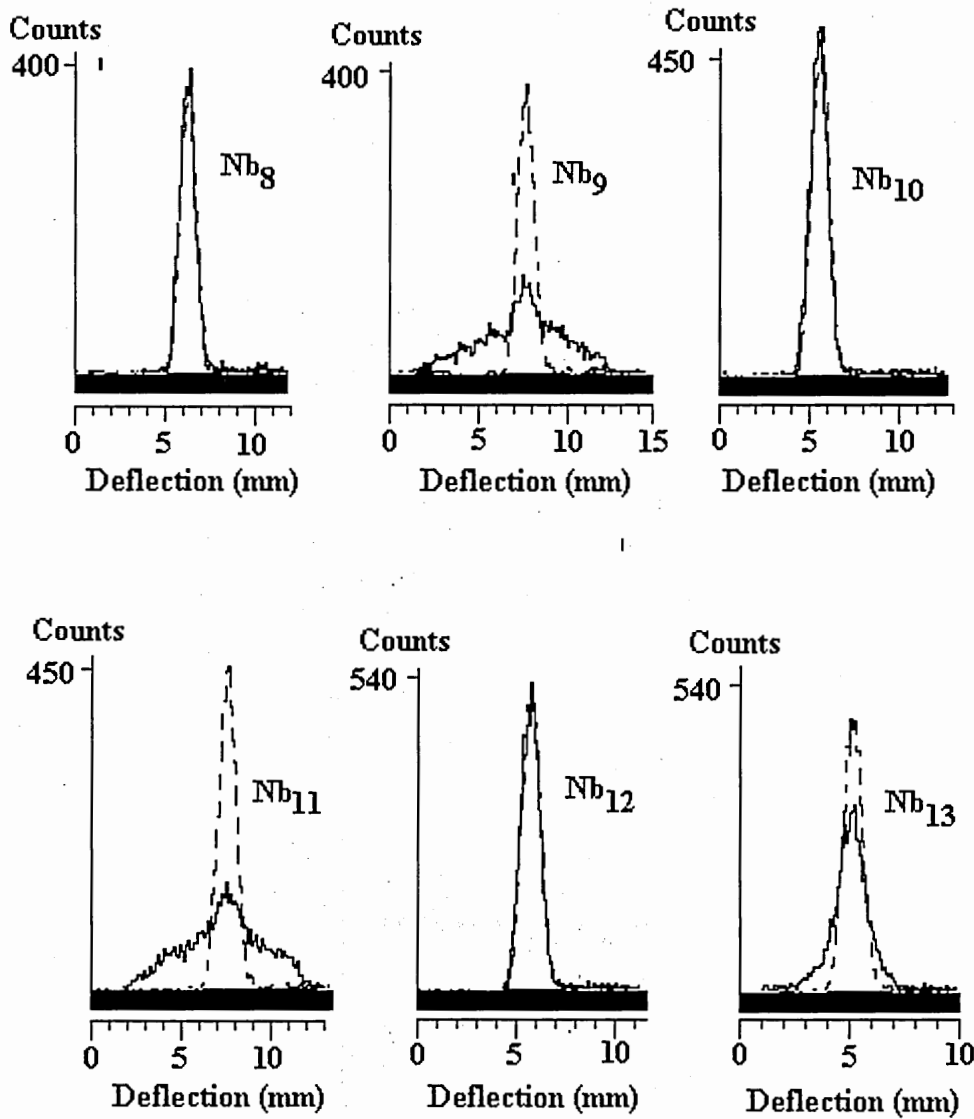


Figure 34: Niobium clusters in the range Nb₈ to Nb₁₃ deflected by an inhomogeneous magnetic field. The dashed line is the profile without magnetic field and the solid line is after applying 0.9 T. This experiment was done at 20 K. The response of Nb₉ is stronger than Nb₇ (shown in the previous figure).

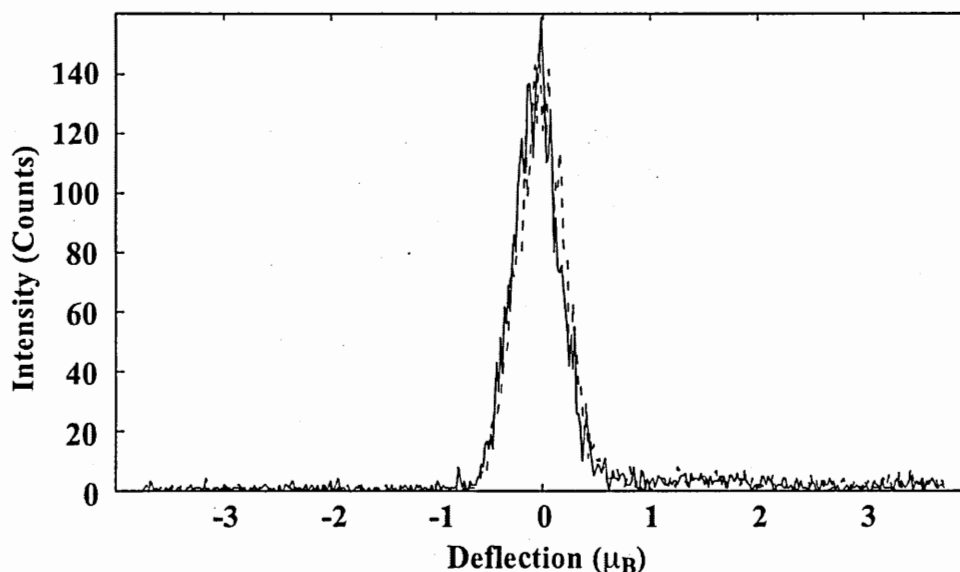


Figure 35: The Stern-Gerlach experiment of Nb_{22} . The dashed line is the peak with zero field and the solid line is after applying 0.9 T. The x-axis scale has been converted to magnetic moment in Bohr magnetons. Almost no visible response to the magnetic field. This is also the case for all even-clusters studied, with the only exception of the dimer.

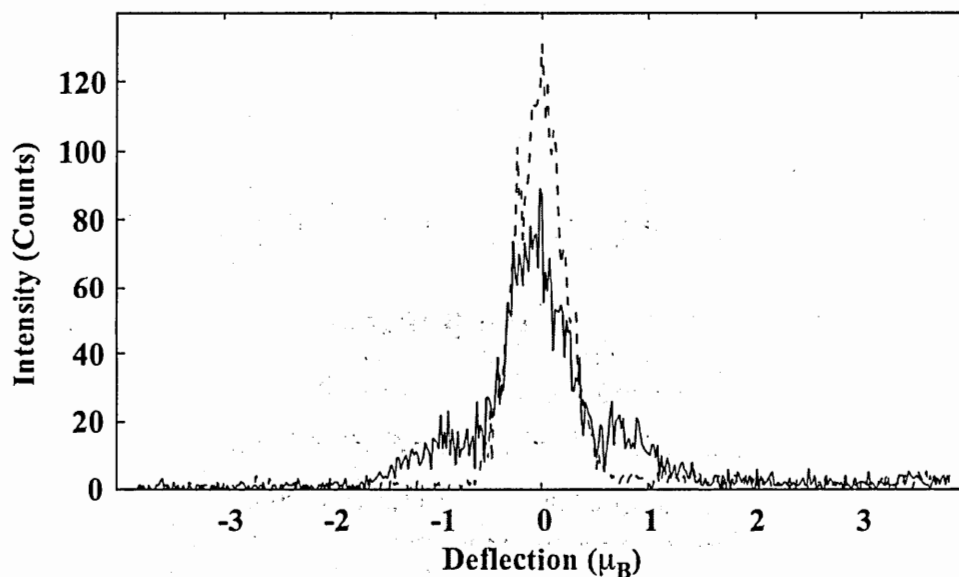


Figure 36: The Stern-Gerlach experiment of Nb_{23} . The dashed line is the peak with zero field and the solid line is after applying 0.9 T. The x-axis scale has been converted to magnetic moment in Bohr magnetons. Contrary to ferromagnetic clusters [W.A. de Heer, 1990], the response is towards higher as well as lower magnetic field in this case.

The shapes of these deflected peaks reflect the fact that we measure the average projection of the magnetic moment on the axis of the field. In the case of the Stern-Gerlach experiment done with atoms we only observe two projections of the spin, but in the case of a cluster the spin is usually coupled to the cluster axis or the rotational angular momentum which give different projections.

Regardless of the kind of coupling the extension of the wings in these peaks is a good measure of the magnitude of the magnetic moment. To measure the extension of the wings we looked for the threshold when the intensity starts to increase. This problem is similar to finding the threshold in the measurement of ionization potential from the ionization efficiency [K.E. Schriver, 1990]. Similarly, we find the intersection between the baseline and the last descent in the signal and compare it to the undeflected peak. The results are shown in figure 37 for clusters in the range Nb_3 to Nb_{52} . The values oscillate about $1 \mu_B$ for odd clusters and zero for even clusters, which means a g-factor of 2 for odd clusters.

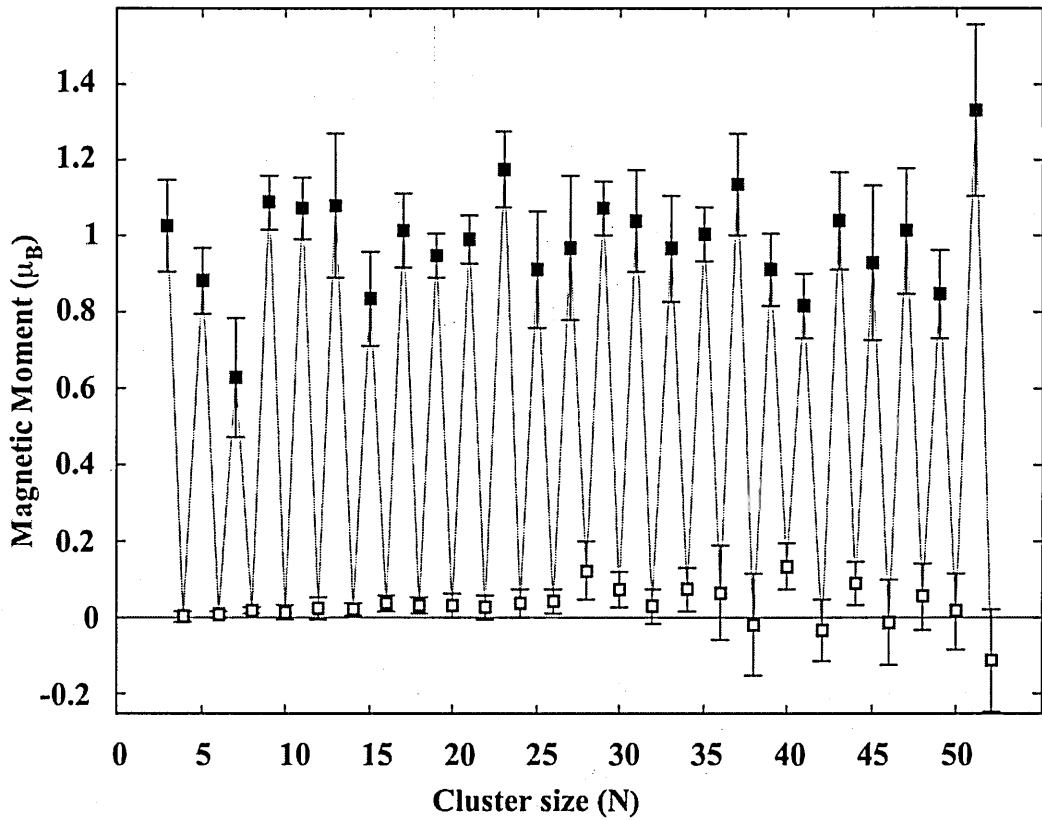


Figure 37: Magnetic moment of niobium clusters measured from the extension of magnetic deflections in Stern-Gerlach experiments. Filled squares are odd clusters, open squares are even clusters.

The projection of the spin on the field axis depends on the coupling of the spin with the cluster axis and the rotational angular momentum. If the spin is strongly coupled to the rotational angular momentum the spin projection follows equation 23.

$$S_z = \frac{1}{2} \frac{M_J}{\sqrt{J(J+1)}} \quad (23)$$

Where S_z is the projection of spin on the magnetic field axis, J is the total angular momentum and M_J is the projection of J on the magnetic field axis. This case would yield a deflection profile that would look like a pedestal as shown in figure 38(a). The distribution of magnetic moments would go from minimum to maximum with equal

probability. The actual deflection profile would be broader due to the physical width of the undeflected peak.

Another case would be when the spin is coupled to the cluster axis. Then the projection of the magnetic moment would be given by equation 24.

$$S_z = \frac{1}{2} \frac{M_J K}{J(J+1)} \quad (24)$$

Where S_z is the projection of spin on the field axis, J is the total angular momentum, M_J is the projection of J on the field axis and K is projection of J on the cluster axis. In this case the distribution of angular momentum would be logarithmic (equation 25) and would produce the deflection profile shown in figure 38(b).

$$P(x) \propto \log \left(\frac{M_o}{|x|} \right) \quad (25)$$

Where $P(x)$ is the probability of having the magnetic moment projection x and M_o is the total magnetic moment.

Other possibility is the case where the coupling of the spin is so weak that it can be considered free. This would yield a deflection profile with two narrow projections as shown in figure 38(c). Yet another possibility would be if the spin were in contact with a thermal bath, then the projection would be extremely narrow with only a slight thermal average deflection towards higher field. As shown in figure 38(d).

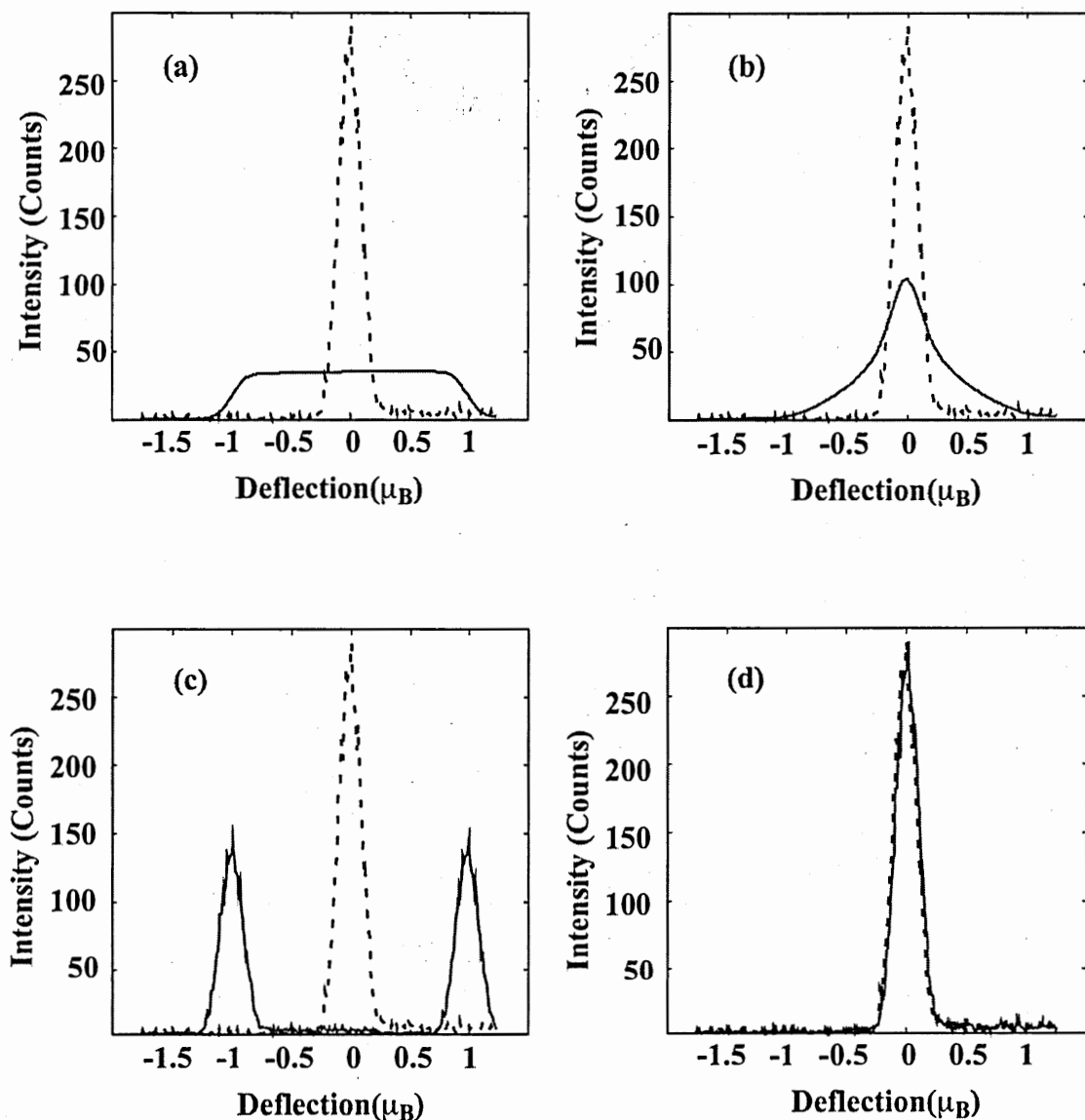


Figure 38: Hypothetical deflection profiles for different coupling cases. (a) Spin strongly coupled to the total angular momentum of the cluster produces a pedestal-like distribution of magnetic moments. (b) Spin strongly coupled to the cluster axis produces a logarithmic distribution of magnetic moments. (c) Spin uncoupled produces two projections. (d) Spin in contact with a thermal bath produces a small thermally averaged deflection. The dashed lines are the profiles with zero field and the continuous lines are with a magnetic field applied. The magnetic moment distributions have been convoluted with the undeflected peaks to get the simulated profile.

These four cases could be used to try to fit the observed deflections, but the shapes of the deflected peaks are not clearly one case or another, besides there could be intermediate coupling regimes in which the shapes were different. Instead of using a fitting routine we notice that the second moment of the distribution of magnetic moments is a good indicator of the kind of coupling. The second moment is defined by the following equation:

$$I_2 = \frac{\int_{-M_0}^{M_0} (x - \langle x \rangle)^2 I(x) dx}{I_0} \quad (26)$$

Where $I(x)$ is the intensity as a function of magnetic moment and I_0 is the total intensity as defined in equation 17. It goes from almost zero for the thermally averaged case to $1 \mu_B^2$ for the free spin case. Table 1 summarizes this observation.

Table 1: Value of the second moment of the distribution of magnetic moments for several coupling cases.

Coupling case	Shape of the distribution	Second Moment (μ_B^2)
Coupled to a thermal bath	Narrow	0
Coupled to the cluster axis	Logarithmic	1/9
Coupled to the total angular momentum	Pedestal	1/3
Uncoupled	Two projections	1

The effect of avoided crossings has been ignored in these approximations. They would tend to reduce the magnitude of the second moment, but it is not as severe as in the case of electric dipoles. The energy of a magnetic moment of $1 \mu_B$ in a field of 1 T is about 50

times lower than an electric dipole of 20 D in a field of 80 kV/cm, so the density of crossings is less than for the Stark diagram.

As presented in table 1, when the spin is more uncoupled the second moment of the distribution of magnetic moment increases. We can measure this second moment from the experimentally obtained peaks by subtracting the off-peak second moment from on-peak in quadrature. This will give us an indicator of how free the spin is. The results for niobium clusters in the range Nb_3 to Nb_{70} are shown in figure 39. As expected the second moment for the even clusters is zero and the calculated values shown give us an idea of the sensitivity of the measurement. Odd clusters show values as large as $0.24 \mu_B^2$ and as low as $0.04 \mu_B^2$ with size dependent variations. These experiments were done at $T=20$ K for clusters in the range Nb_{6-70} and at $T=33$ K for Nb_{3-5} .

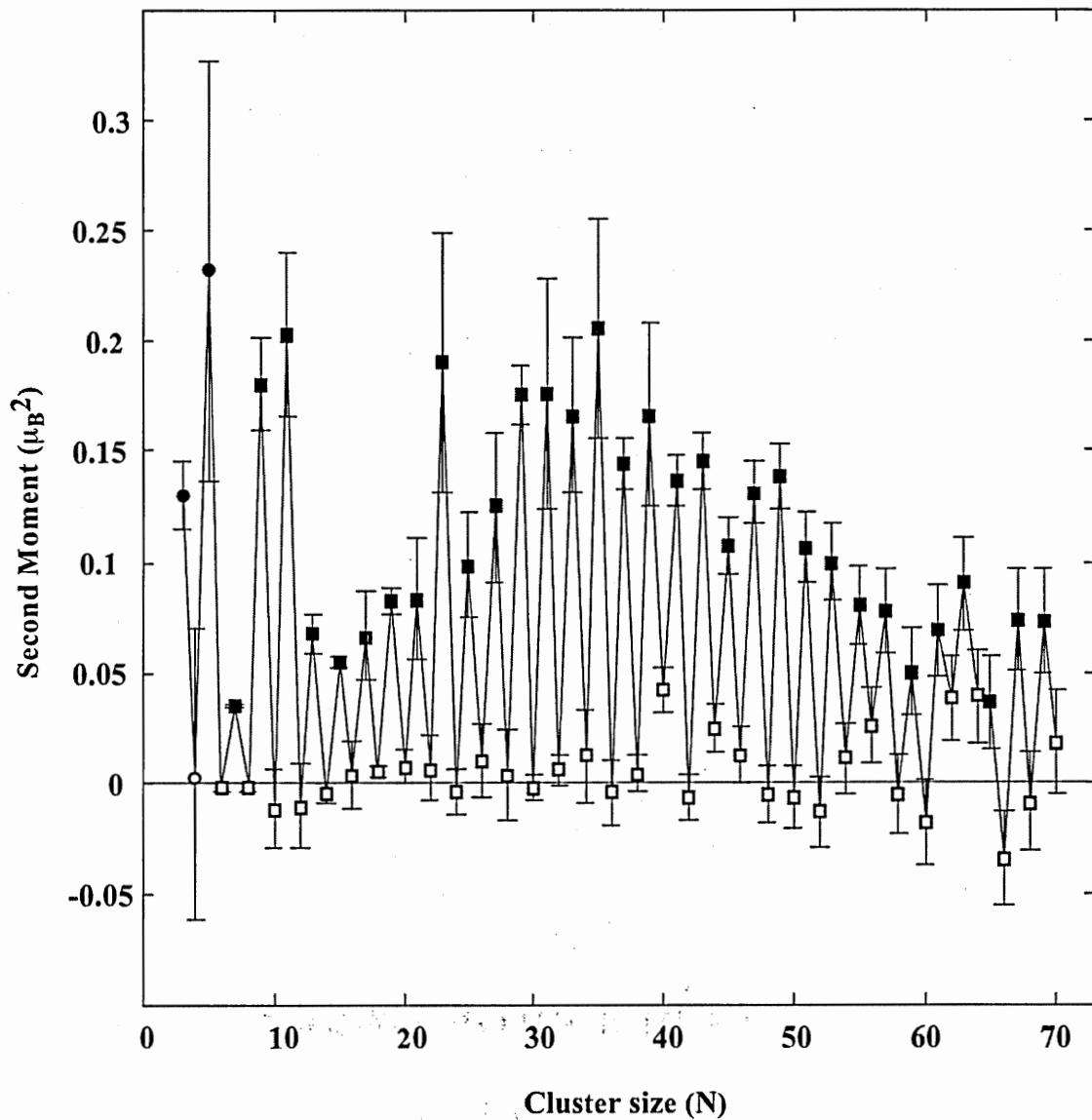


Figure 39: Second moment of the distribution of magnetic moments of niobium clusters. Experiments done at T=20 K for the range Nb₆₋₇₀ (squares) and at T=33 K for Nb₃₋₅ (circles). Filled symbols are odd clusters, open symbols are even clusters.

3.6 Correlation between Magnetic and Electric Deflection Experiments.

For clusters with odd number of electrons it is possible to compare the second moment of the distribution of magnetic moments with the ferroelectric fraction. The width of the distribution (square root of the second moment) is presented in figure 40 together with the ferroelectric fraction. The correlation coefficient of these two values is 0.41, which is considered moderate. This suggests that the ferroelectric property is related to the uncoupling of the spin.

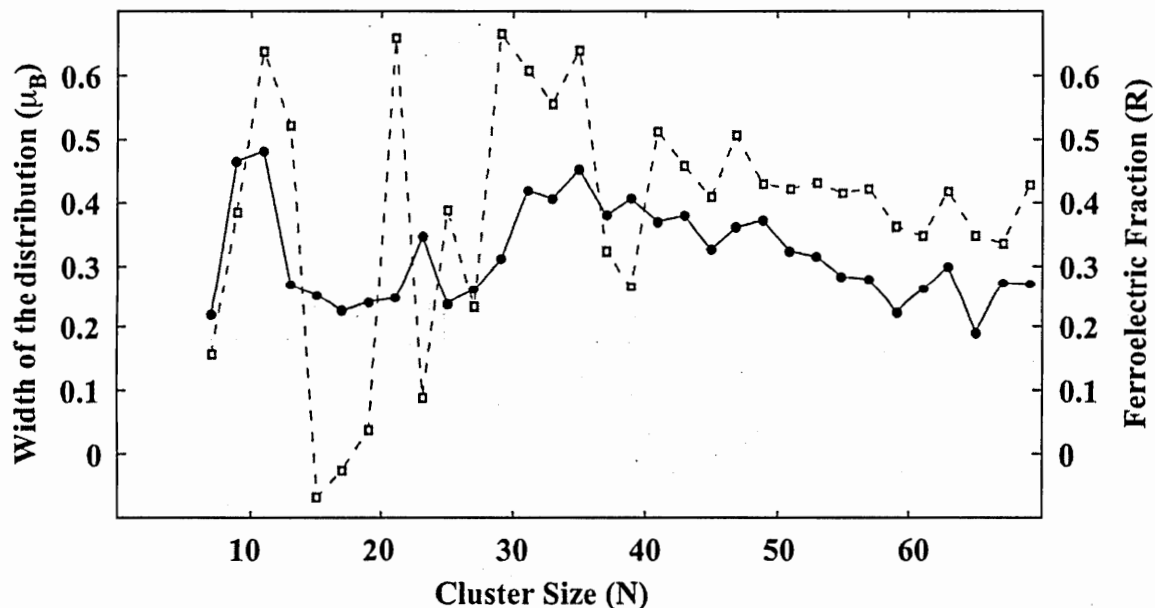


Figure 40: Width of the distribution of magnetic moments in niobium clusters with odd number of electrons measured at 20 K and 0.9 T (solid line) compared to the ferroelectric fraction measured at 20 K and 60 kV/cm (dashed line).

CHAPTER IV

EXPERIMENTS WITH VANADIUM, TANTALUM AND Nb_NAl_M

In the present chapter we extend our study to tantalum, vanadium [W.A. de Heer, 2003b] and the binary alloy Nb_NAl_M .

4.1 Electrical Polarizabilities of Vanadium and Tantalum Clusters.

At room temperature, the deflections of vanadium and tantalum clusters follow a quadratic dependence on the field, so they are polarizable particles. Results are shown in figure 41 for vanadium and figure 42 for tantalum. In both cases the polarizabilities are higher than the bulk value. Using equation 6 to fit the data we get 0.18 nm for δ in vanadium and 0.19 nm in tantalum. These values are so large that some clusters have polarizabilities of 4 times the bulk value. In the case of niobium (figure 19) δ is 0.1 nm, which accounts for polarizabilities of 2.5 times the bulk value. When cooled down vanadium and tantalum clusters develop permanent dipole moments as seen in niobium, however it happens at lower temperatures as will be shown below.

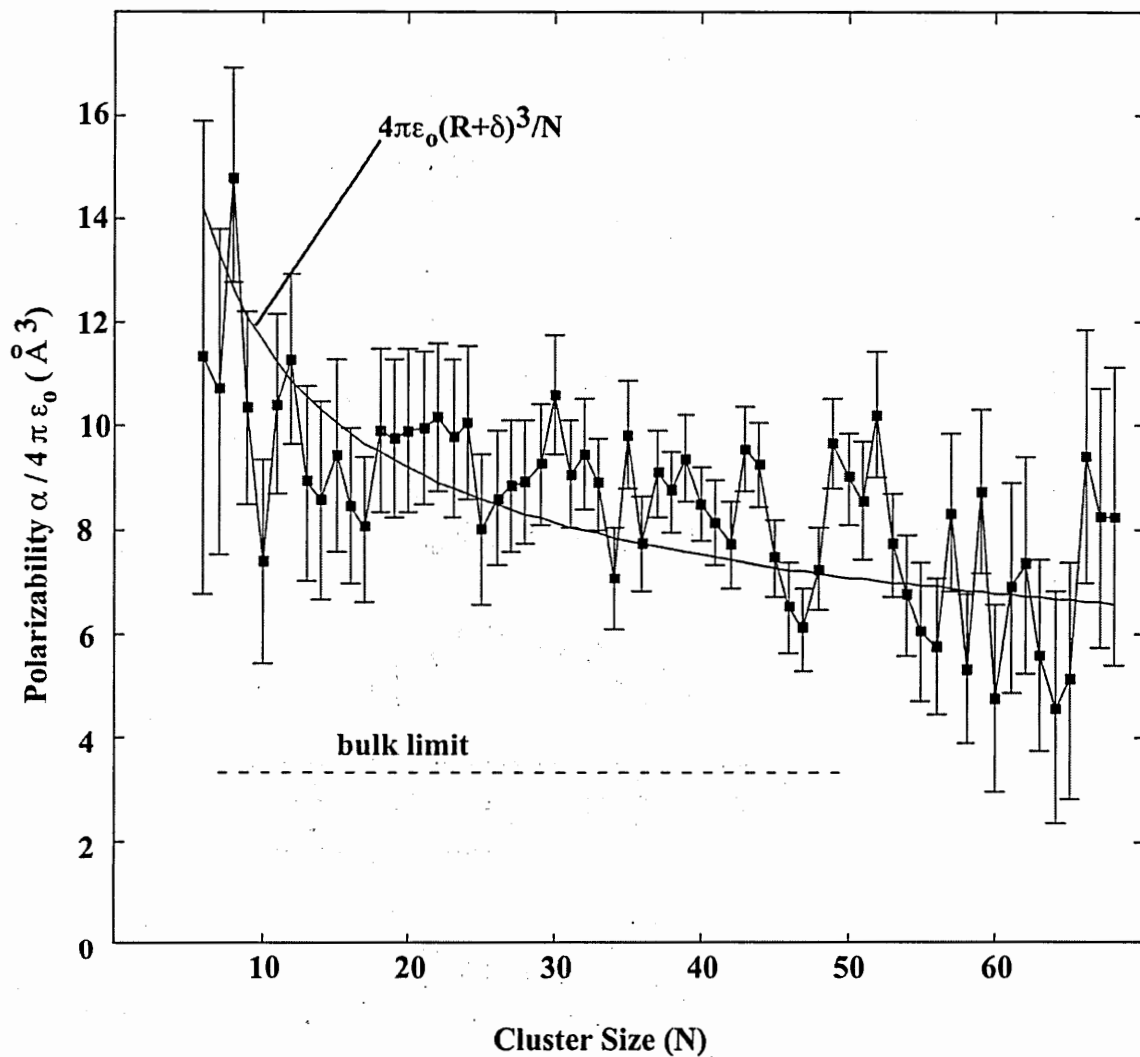


Figure 41: Polarizability per atom of vanadium clusters measured at 300 K and 72 kV/cm. The dashed line is the bulk limit and also shown is the polarizability calculated with the spill-out approximation (equation 6) for $\delta=0.18$ nm.

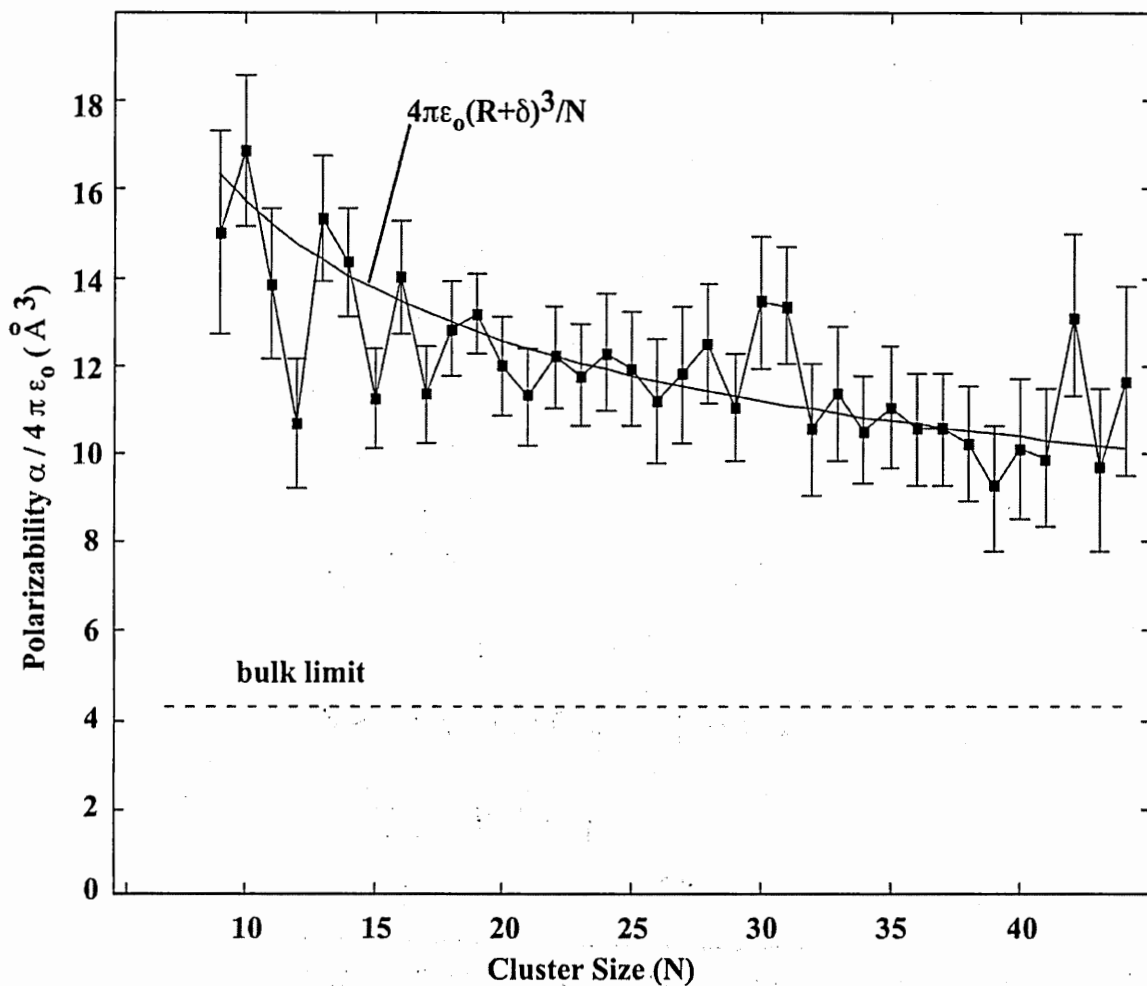


Figure 42: Polarizability per atom of tantalum clusters measured at 300 K and 72 kV/cm. The dashed line is the bulk limit and also shown is a fitting with the spill-out approximation (equation 6) with $\delta = 0.19$ nm.

4.2 Low Temperature Results with Vanadium and Tantalum Clusters

Vanadium and tantalum clusters develop tails at low temperatures, similarly to what we observed in niobium, and a good fraction of the clusters are deflected beyond the detector limits. Figure 43 shows the ferroelectric fraction measured at 18 K in vanadium clusters and figure 44 is the result of an experiment at 21 K with tantalum. Notice that clusters with even number of electrons in general show larger values of R .

If we apply the model proposed for niobium we could use these results to estimate the transition temperature. Assuming that the values of R are already saturated at 80 kV/cm we can use equation 19 to get T_G . Figures 45 and 46 show the calculated values for vanadium and tantalum respectively. It can be seen that in both metals T_G s are lower than in the case of niobium. Several features are similar between these metals, for example V_{13} and Ta_{13} are normal (They have no permanent dipole moment, hence $R=0$) but V_{14} and Ta_{14} have a T_G of 14 K, which is the maximum in both cases. Notice also that a common feature of the three metals is that there is a sharp transition at 28 atoms.

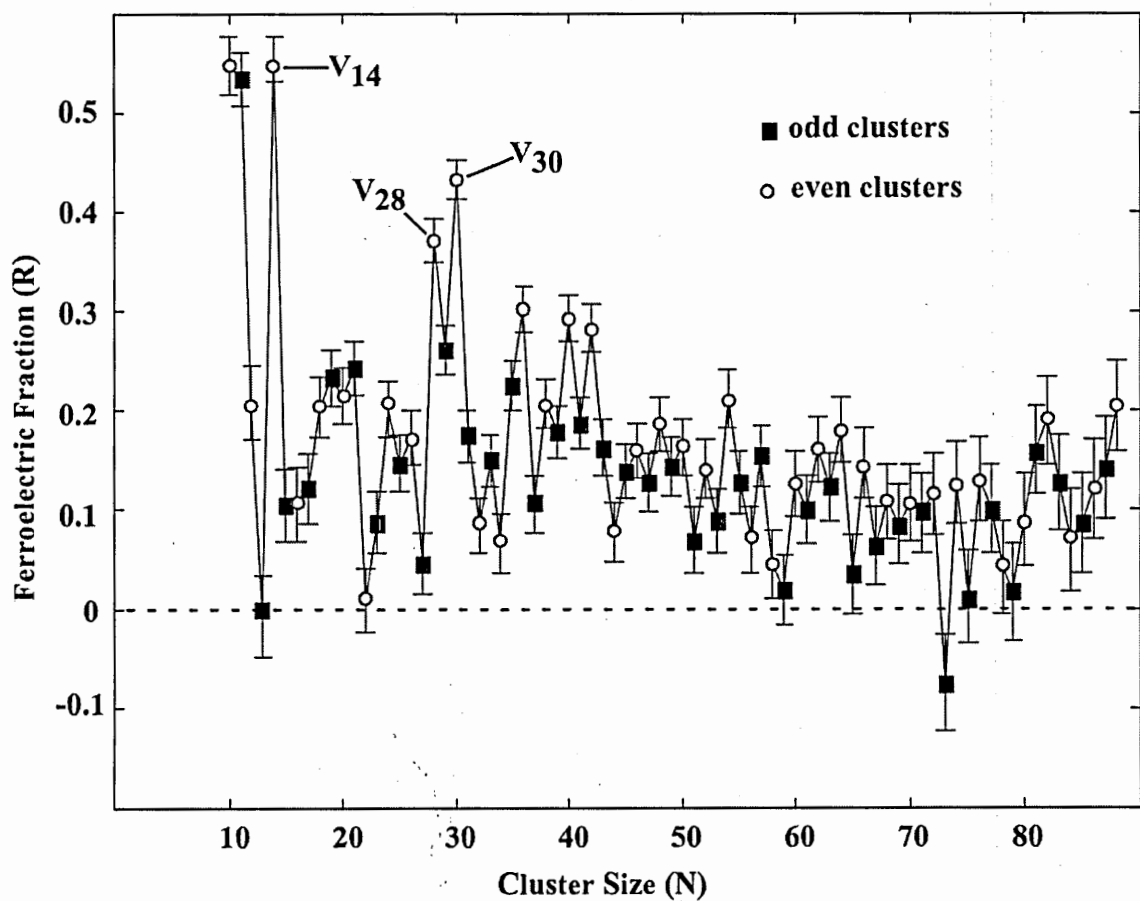


Figure 43: Ferroelectric fraction of vanadium clusters in the range V_{10} to V_{88} . Experiment done at 18 K and 80 kV/cm. Errors shown are from counting statistics.

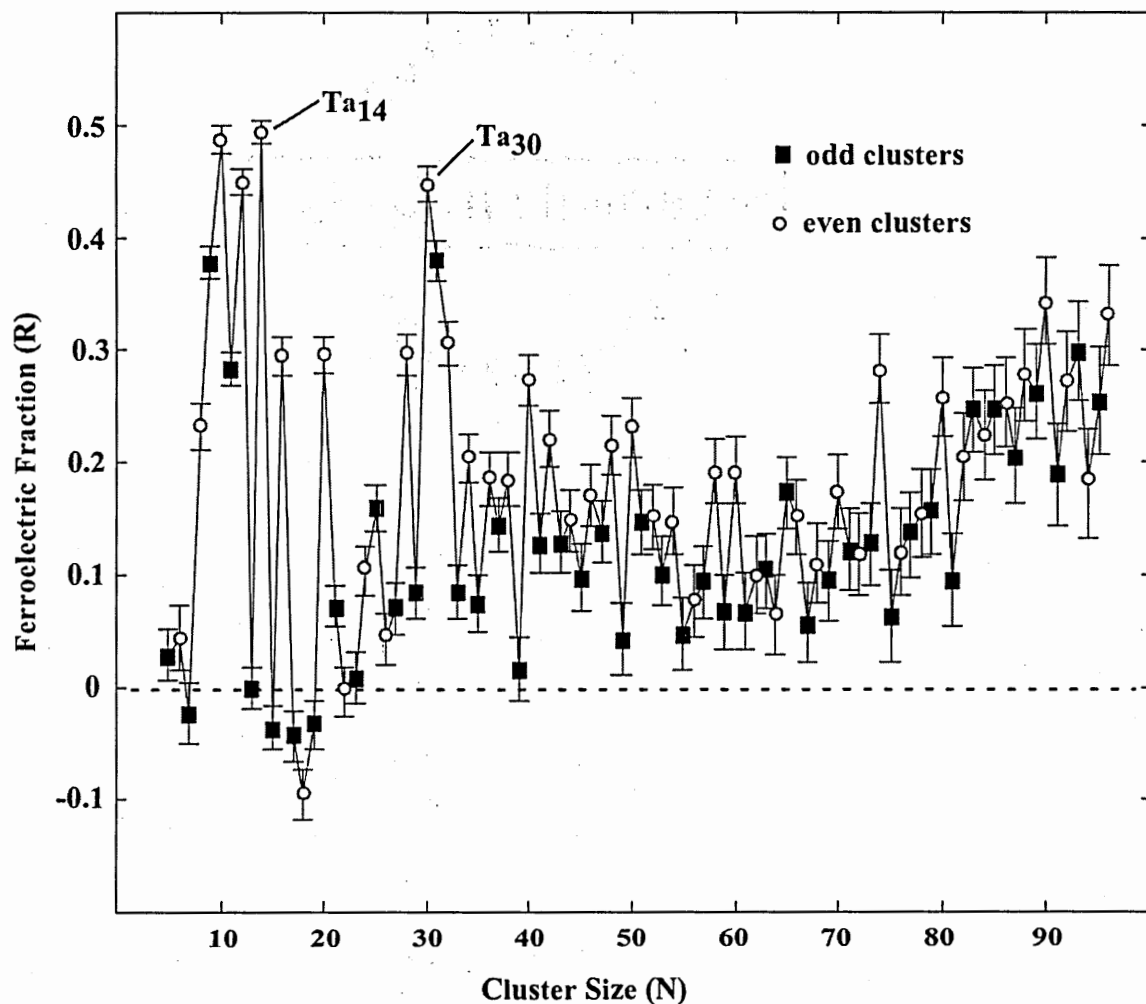


Figure 44 Ferroelectric fraction of tantalum clusters in the range Ta₅ to Ta₉₆. Experiment done at 21 K and 80 kV/cm. Errors are from counting statistics.

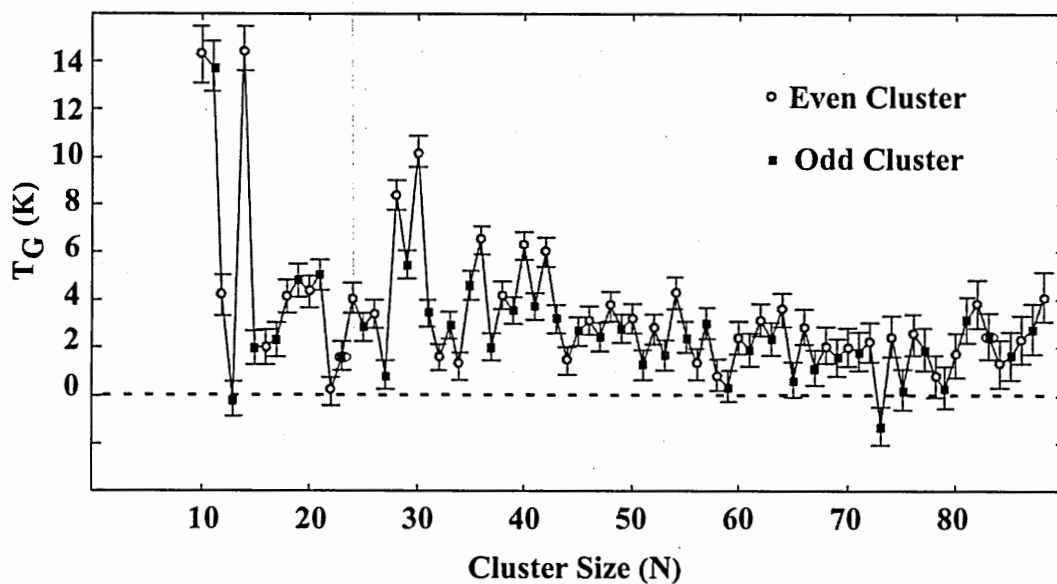


Figure 45: Transition temperature T_G calculated in the model for vanadium clusters.

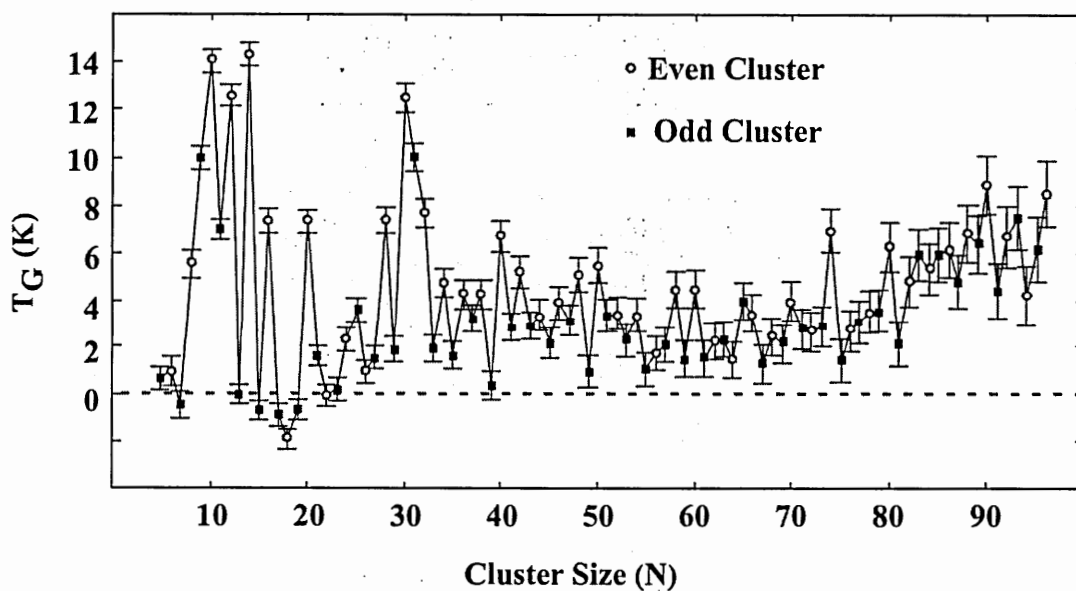


Figure 46: Transition temperature T_G calculated in the model for tantalum clusters.

4.3 Results with Nb_NAl_M

We run an experiment using a sample made of the alloy $\text{Nb}_{0.7}\text{Al}_{0.3}$ and it made binary clusters with several compositions. Because Nb_3Al is a superconductor at 17.5 K [Kittel, 1996] we wanted to see the effect of adding aluminum atoms to a niobium cluster. Figure 47 shows our results for $\text{Nb}_{15}\text{Al}_M$. Other clusters were affected in less degree, but the general trend was that adding aluminum enhanced the ferroelectric effect.

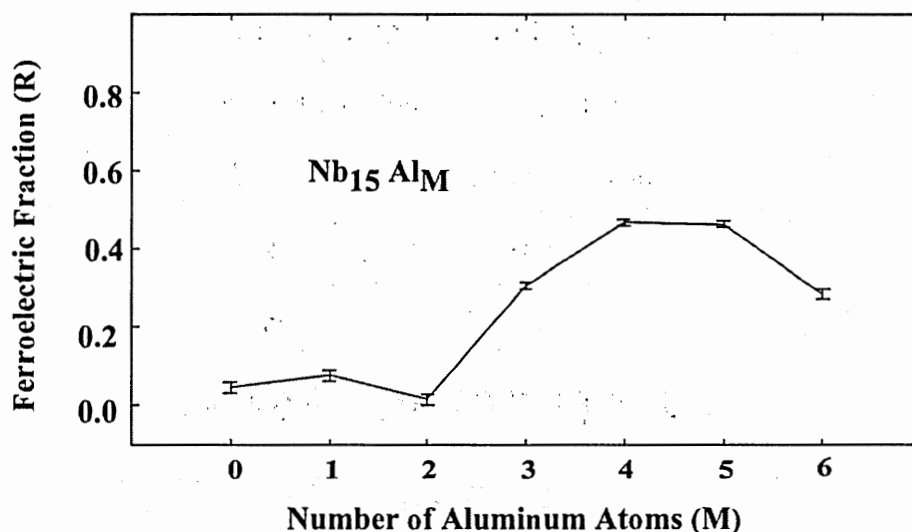


Figure 47: Ferroelectric fraction in a cluster of 15 niobium atoms doped with aluminum. Error bars show the uncertainty in counting statistics. Experiment done at 34 K and 60 kV/cm.

CHAPTER V

DISCUSSION AND CONCLUSION

Niobium clusters have been studied before, although not at the low temperatures of this work. Mass abundance spectra [V. Kumar, 2001] show magic numbers that are different from the icosahedral growth, suggesting that the electronic structure is the one that determines its growth behavior. Photoionization threshold measurements with Nb_{4-29} [R.L. Whetten, 1986] show high values for $N=8, 10$ and 16 , that correlates with reactivity toward D_2 [M.E. Geusic, 1985]. In our polarizability experiments at low temperatures, Nb_N clusters that behave normally include $N=8, 10, 15, 16, 17, 19$ and 22 , so those clusters that have higher ionization potentials are among the ones that behave normally, however there is not a one to one correspondence.

5.1 Possible connection with superconductivity

Experience has shown that properties of the bulk are already visible in clusters, hence we expect to see some signature of superconductivity [M. Tinkham, 1996] in clusters of niobium. Superconductivity has a coherence length associated that for niobium is 38 nm [C. Kittel, 1996]. This is much larger than the typical diameter of the particles studied in this thesis (less than 3 nm). The Anderson limit [P.W. Anderson, 1959], that is when the superconducting gap is equal to the energy level spacing, happens for 7000 atoms in niobium which is also beyond the size range in these experiments. However, the observed

ferroelectric behavior could be a precursor to superconductivity and it is supported by the following observations:

- The transition temperatures of ferroelectricity (T_{GS}) in niobium clusters tend to 10 K, which is close to the 9.5 K of its superconducting transition. Vanadium and tantalum clusters have lower T_{GS} as are their superconducting transition temperatures.
- Our experiments with clusters of manganese, bismuth and cobalt at low temperature show normal metallic polarizabilities and they are not superconductors in the bulk.
- The odd-even effect observed in the three metals favors clusters with even number of electrons. This suggests that pairing is important to the formation of the dipoles. It has been proposed [J. von Delft, 2001], that the presence of an unpaired electron blocks an energy level for pair scattering, reducing the superconducting correlation in small grains.
- Nb_3Al is an alloy that superconducts at 17.5 K and in experiments with binary clusters we found that ferroelectricity in niobium was enhanced with the addition of aluminum atoms.
- The correlation found between the second moment of the distribution of magnetic moments and the ferroelectric fraction suggests that the spin of the last electron uncouple in the ferroelectric state. And conduction electron spin resonance

experiments [D.C. Vier, 1983] have shown that the spin relaxation rate is slower in the superconducting state than in the normal state, implying a weaker spin coupling.

Our experiments with lead clusters at low temperatures show that they are normal polarizable particles, so it could be that this property only applies to some superconductors, but the facts just mentioned suggest a connection between these two properties.

This ferroelectric state is a property of the electrons acting collectively because if there were a normal (free) fraction of them they would move to screen any electric field. Based on the theory of hole superconductivity [F. Marsiglio, 1990], it has been proposed [J.E. Hirsch, 2003] that the charge distribution in superconductors is inhomogeneous and it would produce quadrupole moments in clusters with non-spherical shapes. The existence of electric fields inside a superconductor is consistent with this theory as well as the possibility of electric dipole moments, since the ground state wave function would be rigid.

Alternatively, it has been suggested that the anomalous ferroelectricity in niobium could be explained in the electronic ferroelectricity model [C.D. Batista, 2002] [C.D. Batista, 2003] where a system with two dispersive bands with opposite parity plus an inter-band local Coulomb interaction gives rise to an electronic ferroelectric state. Ab initio calculations [G.B. Grad, 2000] show that the valence electron in Nb has the same amount

of s and p character, making it a strong candidate for this model. The transition from this state to superconductivity as the particle grows is still an open question.

5.2 Conclusion

A state of the art molecular beam machine was developed that can make cold clusters beams. Temperature can be controlled from 10 K to 300 K. The mass spectrometer in the position-sensitive mode allows the measurement of deflections of the order of 5 microns. This tool allowed us to study electrical polarizability in an uncharted region.

Polarizabilities of small niobium, vanadium and tantalum clusters at room temperature are all higher than the bulk value. They can be approximated by taking into account the spill-out of the electronic cloud. At low temperatures most of these clusters (with some exceptions like Nb_{17} , V_{13} and Ta_{13}) develop dipole moments that are more than an order of magnitude larger than the normal induced ones in fields of the order of 80 kV/cm. These dipoles are comparable to the ones found in the best ferroelectric materials known.

The structure of the cluster is especially important in the small size range where large variations are found, but for larger clusters (beyond Nb_{28} for example) there are less variations and only an odd-even alternation dominates the size dependence. Beyond Nb_{130} this odd-even alternation is not visible in our experiments.

Magnetic deflection measurements show that clusters with even number of electrons have spin zero (except for the dimer) and clusters with odd number of electrons have spin 1/2 with magnetic moments close to $1 \mu_B$. For niobium clusters with odd number of electrons a positive correlation was found between the ferroelectric fraction and the second moment of their magnetic moment distribution which is a measure of how the spin is coupled to the cluster. This suggests that when a cluster develops an electric dipole moment the spin of the last unpaired electron becomes uncoupled.

The fact that the ferroelectric fraction (and the transition temperature T_G) does not decay for large niobium clusters and the very slow decay in the dipole moment per atom suggest that it is not a surface property. The transition to normal behavior does not happen to at least 300 atoms in niobium. A surface effect that has been predicted for sodium [I.A. Solov'yov, 2002] would yield extremely small dipoles as compared with the ones observed in this work, ruling out that possibility.

The crossover from the ferroelectric to the superconducting state is still to be explored as well as the effect of a magnetic field on the ferroelectric state. Future work in this direction would involve experiments with clusters in the thousand-atom range and simultaneous application of electric and magnetic fields.

REFERENCES

- Alameddine, G., Hunter, J., Cameron, D., and Kappes, M.M., 1992
Electronic and geometric structure in silver clusters
Chem. Phys. Lett. **192**, 122-128
- Anderson, P.W., 1959
Theory of dirty superconductors
J. Phys. Chem. Solids **11**, 26
- Bachels, T., Güntherodt, H.J., Schäfer R., 2000
Melting of Isolated Tin Nanoparticles
Phys. Rev. Lett. **85**, 1250-1253
- Batista, C.D., 2002
Electronic Ferroelectricity in the Falicov-Kimball Model
Phys. Rev. Lett. **89**, 166403-1
- Batista, C.D., Gubernatis, J.E., Bonca, J., and Lin, H.Q., 2003
Intermediate Coupling Theory of Electronic Ferroelectricity
cond-mat / 0308329
- Bergmann T., Martin, T.P., and Schaber, H., 1989
High-Resolution time-of-flight mass spectrometers: Part I. Effects of field distortions in the vicinity of wire meshes
Rev. Sci. Instrum. **60** (3), 347-349
- Billas, I. M. L., Chatelain, A., and de Heer, W.A., 1994
Magnetism From the Atom to the Bulk in Nickel, Cobalt and Iron Clusters
Science **265**, 1682
- Black, C.T., Ralph, D.C., and Tinkham, M., 1996
Spectroscopy of the Superconducting Gap in Individual Nanometer-Scale Aluminum Particles
Phys. Rev. Lett. **76**, 688-691
- Blundell, S.A., Guet, C., Zope, R.R., 2000
Temperature Dependence of the Polarizability of Sodium Clusters
Phys. Rev. Letters **84**, 4826-4829
- Bucher, J.P., Douglass, D.C., and Bloomfield, L.A., 1991
Magnetic Properties of Free Cobalt Clusters
Phys. Rev. Lett. **66**, 3052

Cox, A.J., Louderback, J.G., and Bloomfield, L.A., 1993
Experimental observation of magnetism in rhodium clusters
Phys. Rev. Lett. **71**, 923

CRC Handbook of Chemistry and Physics, 1980
Robert C. West, PhD Editor
60th Edition

de Heer, W. A., Knight, W. D., Chou, M. Y. and Cohen, M. L., 1987
Solid State Physics
edited by H. Ehrenreich and D. Turnbull (Academic, New York), Vol. 40, p. 93.

de Heer, W.A., Milani, P., and Chatelain, A., 1989
Nonjellium-to-jellium transition in aluminum cluster polarizabilities
Phys. Rev. Lett. **63**, 2834–2836

de Heer, W.A., Milani, P., and Chatelain, A., 1990
Spin Relaxation in Small Free Iron Clusters
Phys. Rev. Letters **65**, 488-491

de Heer, W.A., Milani, P., 1991a
Large ion volume time-of-flight mass spectrometer with position- and velocity-
sensitive detection capabilities for cluster beams
Rev. Sci. Instrum. **62** (3), 670-676

de Heer, W.A., Milani, P., and Chatelain, A., 1991b
Magnetic Properties of free alkali and transition metal clusters
Z. Phys. D – Atoms, Molecules and Clusters **19**, 241-245

de Heer, W.A., 1993
The physics of simple metal clusters: experimental aspects and simple models
Rev. Mod. Phys. **65**, 611-676

de Heer, W.A., et al. 2003a
Magnetic deflections in niobium clusters
In preparation

de Heer W.A. et al 2003b
Ferroelectricity in Vanadium, Niobium and Tantalum Clusters
To be published

Dugourd, P., Compagnon, I., Lepine, F., Antoine, R., Rayane, D., and Broyer, M., 2001
Beam deviation of large polar molecules in static electric fields: theory and experiment
Chemical Physics Letters **336**, 511-517

- Eckardt, W., 1984
Dynamical Polarizability of Small Metal Particles: Self-Consistent Spherical Jellium Background Model
Phys. Rev. Lett. **52**, 1925-1928
- Gerion, D., Hirt, A., Billas, I.M.L., Chatelain, A., and de Heer, W.A., 2000
Experimental specific heat of iron, cobalt, and nickel clusters studied in a molecular beam
Phs. Rev. B. **62**, 7491-7501
- Gerion, D., 1999
Thermal properties of ferromagnetic clusters studied in a molecular beam
Thesis No 1963 (1999) Ecole Polytechnique Federale de Lausanne
- Geusic, M.E., Morse, M.D., and Smalley, R.E., 1985
Hydrogen chemisorption on transition metal clusters
J. Chem. Phys. **82**, 590
- Grad, G. B., Blaha, P., Luitz, J., Schwarz, K., Fernández Guillermet, A., and Sferco, S.F., 2000
Electronic structure and chemical bonding effects upon the bcc to phase transition: Ab initio study of Y, Zr, Nb, and Mo
Phys. Rev. B. **62**(19), 12743-12753
- Hahn, M.Y., and Whetten, R.L., 1988
Rigid-Fluid transition in Specific-Size Argon Clusters
Phys. Rev. Lett. **61**, 1190-1193
- Hirsch, J.E., 2003
Charge expulsion and electric field in superconductors
cond-mat/0308604v2
- James, A.M., Kowalczyk, P., Fournier, R., and Simard, B., 1993
Electronic spectroscopy of the niobium dimer molecule: Experimental and theoretical results
J. Chem. Phys., **99** (11), 8504-8518
- Jarrold, M.F., Constant, V.A., 1991
Silicon cluster ions: Evidence for a structural transition
Phys. Rev. Lett. **67**, 2994-2997
- Katakuse, I. and Ichihara, T., 1985
Mass distributions of copper, silver and gold clusters and electronic shell structure
International Journal of Mass Spectrometry and Ion Processes. **67**, 229-236

- Khana, S.N., Linderoth, S., 1991
Magnetic behavior of clusters of ferromagnetic transition metals
Phys. Rev. Lett. **67**, 742-745
- Kittel, C., 1996
Introduction to Solid State Physics
John Wiley & Sons, 7th edition, Chapter 12: Superconductivity
- Knickelbein, M.B., and Yang, S., 1990
Photoionization studies of niobium clusters: Ionization Potentials for Nb₂-Nb₇₆
J. Chem. Phys. **93** (8), 5760-5767
- Knickelbein, M.B., 2001a
Electric dipole polarizabilities of Ni₁₂₋₅₈
J. Chem. Phys. **115** (13), 5957
- Knickelbein, M.B., 2001b
Experimental Observation of Superparamagnetism in Manganese Clusters
Phys. Rev. Lett. **86**, 5255-5257
- Knight, W.D., Clemenger, K., de Heer, W.A., Saunders, W., Chou, M.Y. and Cohen, M.L., 1984
Electronic Shell Structure and Abundances of Sodium Clusters
Phys. Rev. Lett. **52**, 2141
- Knight, W.D., de Heer, W.A., Clemenger, K., Saunders, W., 1985a
Electronic shell structure in potassium clusters
Solid State Communications. **53**, 445
- Knight, W.D., Clemenger, K., de Heer, W.A., Saunders, W., 1985b
Polarizability of Alkali Clusters
Phys. Rev. B **31**, 2539-2540
- Kresin, V.V., Bonin, K.D., 1997
Electric-dipole polarizabilities of atoms, molecules and clusters
World Scientific, Singapore, River Edge, N.J.
- Kumar, V., Esfarjani, K., and Kawazoe, Y., 2001
Clusters and Nanomaterials
Springer Series in Cluster Physics (Springer Verlag, Heidelberg), p. 9.
- Kumar, V., and Kawazoe, Y., 2002
Atomic and electronic structures of niobium clusters
Physical Review B **65**, 125403

- Lang, N. D., and Kohn, W., 1970
Theory of Metal Surfaces: Charge Density and Surface Energy
Phys. Rev. B. **1**, 4555-4568
- Marsiglio, F., Hirsch, J.E., 1990
Hole superconductivity and the high- T_c oxides
Phys. Rev. B. **41**, 6435-6456
- Matthias, B., Weller, Ed., 1976
Ferroelectricity
Elsevier Pub.Co.
- Milani, P., Moullet, I, and de Heer, W.A., 1990
Experimental and theoretical electric dipole polarizabilities of Al and Al₂
Physical Review A **42** (9), 5150-5154
- Moro, R., Xu, X., Yin, S., de Heer, W.A., 2003
Ferroelectricity in Free Niobium Clusters
Science, **300**, 1265-1269
- Moullet, I., 1990
Static electric polarizabilities of sodium clusters
Phys. Rev. B **42**, 11598-11609
- Nomura, K., Kobayashi, S., and Sasaki, W., 1980
J. Phys. Soc. Japan, **48**, 37
- Pokrant, S., 2000
Evidence for adiabatic magnetization of cold Dy_N Clusters
Phys. Rev. A., **62**, 051201
- Reich, S., Leitus, G., Popovitz-Biro, R., and Schechter, M., 2003
Magnetization of Small Lead Particles
Phys. Rev. Lett. **91**, 147001
- Schäfer, R., Schlecht, S., Woenckhaus, J., Becker, J.A., 1996
Polarizabilities of Isolated Semiconductor Clusters
Phys. Rev. Lett. **76**, 471
- Schmidt, M., Kusche, R., Kronmüller, W., von Issendorff, B., and Haberland, H., 1997
Experimental Determination of the Melting Point and Heat Capacity for a Free Cluster of
139 Sodium Atoms
Phys. Rev. Lett. **79**, 99-102

Schriver, K.E., 1990
Photoionization and Optical Spectroscopy of Atomic Clusters Generated via Laser Ablation
PhD Thesis University of California, Los Angeles

Scoles, G., 1988
Atomic and Molecular Beam Methods
Oxford University Press, New York, Oxford

Shimizu, K., Ishikawa, H., Takao, D., Yági, T., Amaya, K., 2002
Superconductivity in compressed lithium at 20 K
Nature, **419** (6907) 569, 571-2

Shoenberg, D., 1962
Superconductivity
Cambridge University Press. Second edition with additional appendix, reprinted.

Smalley, R.E., 1983
Laser Studies of Metal Cluster Beams
International Conference on Photochemistry and Photobiology, **2**, 167-184

Solov'yov, I.A., Solov'yov, A.V., and Greiner, W., 2002
Structure and properties of small sodium clusters
Phys. Rev. A **65**, 053203

Tikhonov, G., Kasperovich, V., Wong, K., and Kresin, V.V., 2001
A measurement of the polarizability of sodium clusters
Physical Review A, **64**, 063202

Tinkham, M., 1996
Introduction to Superconductivity, Second Edition
Publisher: McGraw Hill

Townes, C.W., Shawlow, A.L., 1975
Microwave Spectroscopy
Dover, New York

Vier, D.C., and Schultz, S., 1983
Observation of conduction electron spin resonance in both the normal and superconducting state of niobium
Physics Letters A, **98**, 283-286

von Delft, J., 2001
Superconductivity in ultrasmall metallic grains
Ann. Phys. (Leipzig) **10** (2001) 3, 1-60

Whetten, R. L., Zakin, M. R., Cox, D. M., Trevor, D. J., and Kaldor, A., 1986
Electron binding and chemical inertness of specific Nb_x clusters
The Journal of Chemical Physics, **85**(3), 1697-1698

Wrigge, G., Hoffmann, M.A., and Issendorff, B.
Photoelectron spectroscopy of sodium clusters: Direct observation of the electronic shell structure
Phys. Rev. A. **65**, 063201

VITA

Ramiro Alfredo Moro was born on March 17th, 1968 in Lima, Peru. He received a Bachelor of Science degree in Electrical Engineering from the National University of Engineering (Lima, Peru) in 1991. For seven years he worked in industry, mainly involved in automation, control and protection projects for mining companies. In 1993 he spent a semester teaching the introductory electric circuits course at the Catholic University in Lima, Peru. He started his studies of Physics at Georgia Tech in the fall of 1998. In 1999 he joined the Small Systems group of Walter de Heer's, where he has been working in the cluster beam experiments for his Ph.D. thesis.